

Colloids in non-equilibrium: From one-dimensional transport to pattern formation at surfaces

vorgelegt von

Diplom-Physiker

Ken Lichtner

aus Bremen

Von der Fakultät II - Mathematik und Naturwissenschaften
der Technischen Universität Berlin
zur Erlangung des akademischen Grades
Doktor der Naturwissenschaften
Dr. rer. nat.

genehmigte Dissertation

Promotionsausschuss:

Vorsitzende:

1. Gutachterin:

2. Gutachter:

Prof. Dr. Janina Maultzsch

Prof. Dr. Sabine H. L. Klapp

Prof. Dr. Joachim Dzubiella

Tag der wissenschaftlichen Aussprache: 18.08.2014

Berlin 2014

D 83

Contents

Contents	i
Figures	v
Abstract	1
Zusammenfassung	3
Publications	5
1. Introduction	7
1.1 Colloidal suspensions: A short overview	7
1.2 From equilibrium phase behavior to pattern formation	8
1.3 Systems driven out of equilibrium	10
1.4 Motivation, goals and structure of this thesis	11
2. Theory	15
2.1 Equilibrium theory of the many-body system	15
2.1.1 Many-body Hamiltonian	15
2.1.2 Grand potential functional	16
2.1.3 Hohenberg-Kohn variational principle for the one-body density	17
2.1.4 Ideal gas limit	19
2.1.5 Excess free energy	21
2.2 Relaxation dynamics of colloids in non-equilibrium	23
2.2.1 Overdamped Langevin equation	23
2.2.2 Dynamics of the probability density function	24
2.2.3 Dynamical density functional theory	24
2.3 Spatiotemporal correlations	27
2.3.1 Pair correlation function of the bulk system	27
2.3.2 Percus' test particle limit	28
2.3.3 The van Hove function	30

2.4	Pyragas control loop	32
3.	The one-dimensional driven system	35
3.1	Model	35
3.2	Delay-induced instability	36
3.2.1	Linear stability analysis	37
3.2.2	Stability thresholds	40
3.2.3	Nonlinear regime: Numerical study of the one-body distribution	42
3.2.4	Cycle time for the oscillating density state	45
3.2.5	Microchannel geometry	46
3.3	Influence of repulsive particle interactions	51
3.4	Summary	60
4.	The phase-separating magnetic mixture	63
4.1	Model	64
4.2	Equilibrium theory of the demixing transition	65
4.2.1	The density functional for the mixture	65
4.2.2	Phase behavior	68
4.2.3	Linear stability of the demixing transition	72
4.2.4	Interfacial structure	77
4.3	Demixing dynamics	81
4.3.1	Spinodal demixing	84
4.3.2	Dynamical test particle theory	84
4.4	Spinodal decomposition kinetics	87
4.4.1	Correlation functions	89
4.4.2	Domain size	91
4.5	Nucleation	95
4.5.1	Classical nucleation theory	96
4.5.2	DFT approach to nucleation	98
4.5.3	DDFT approach to nucleation	100
4.6	Summary	104
5.	Field-controlled pattern formation	107
5.1	Model	107
5.2	Results	108
5.3	Summary	114
6.	Concluding remarks	117
6.1	Summary of this thesis	117
6.2	Outlook and experimental realizations	119

Appendix	123
I Gibbs-Bogoliubov relation	123
II Inhomogeneous profiles of the interface	124
Bibliography	127
Acknowledgements	143

Figures

1	Optical manipulation of colloids	10
2	Microscope image of confined colloids	11
3	Magnetic assembly of beads inside a ferrofluid	12
4	Feedback control block diagram	33
5	Stability thresholds for different parameters	39
6	Three-dimensional stability threshold	40
7	Controlled system in the periodic regime	41
8	Stationary solution of the controlled system	43
9	Bifurcation diagram for the periodic system	44
10	Cycle time for the periodic system	46
11	Time-periodic solution for the microchannel	47
12	Cycle time for the microchannel	49
13	Bifurcation diagram for the microchannel	50
14	Density profiles for different tilting strengths	51
15	Transport properties of the tilted system	53
16	Van Hove function at constant driving strength	54
17	First moment for various control amplitudes	55
18	Various snapshots for the balanced case	56
19	Long-time velocities	57
20	First moment for a local control scheme	58
21	Typical density profiles for a local control scheme	59
22	First moment for the interacting system	60
23	Phase diagram for the binary system	69
24	Linear stability analysis for spinodal decomposition	76
25	Interfacial structure of the demixed system	77
26	Grand potential density	79
27	Interfacial line tension	80
28	Snapshots for the demixing process	82
29	Time series for partial van Hove functions	88
30	Partial correlation functions in two dimensions	90

31	Dynamic structure factor for the isotropic species	91
32	Average size for non-magnetic domains	92
33	Average size for magnetic domains	93
34	Domain size from a Vineyard type approximation	94
35	Nucleation barrier from classical nucleation theory	95
36	Grand potential of the nucleus	99
37	DFT results for the nucleation barrier	101
38	DDFT free energy pathway	102
39	Nucleation snapshots	103
40	Stripe formation phase diagram	109
41	Typical snapshots for different surface field ratios	110
42	Averaged net particle current for a constant ratchet amplitude	112
43	Instantaneous current at the onset of the instability	113

Abstract

In this thesis, we investigate the collective behavior of colloidal suspensions at the mesoscale level in equilibrium as well as in non-equilibrium. Related to recent experiments, we focus in the first part of the thesis on the transport behavior of suspensions of purely repulsive "soft" particles in narrow, spatially modulated channels. Based on the modern dynamical density functional theory (DDFT) we investigate for the first time the impact of external control loops with time delay on colloidal dynamics in non-equilibrium. For different control targets which are also accessible in experiments we demonstrate that the manipulation of the global particle behavior is possible, including the reversal of the particle current and the stabilization of spatiotemporal oscillations. By adding magnetic particles with classical spins of Heisenberg type in the second part of the thesis, we find spontaneous pattern formation with magnetic and non-magnetic domains. Depending on the particle density and concentration we find a first-order demixing transition and a second-order phase transition for the magnetization at fixed magnetic coupling. Based on classical and dynamical density functional approaches we calculate the fluid-fluid interface in equilibrium as well as the domain growth in non-equilibrium. We find two distinct demixing regions for the equilibrium phase diagram, namely spinodal decomposition and nucleation where the latter is an activated growth process. Based on DDFT we show that the domain growth within spinodal decomposition grows systematically with a power law exponent that corresponds to predictions from classical theories. For the nucleation process in non-equilibrium we show new results for the physical pathway towards equilibrium where we choose the energy barrier and particle excess number as coordinates. In the last part of the thesis we demonstrate that the pattern formation in non-equilibrium can be altered in a controlled way by using time-dependent external surface fields. For a novel dynamical instability where stripes against the symmetry of the external potential form, we show that the underlying mechanism is based on an interplay between the intrinsic spinodal decomposition and time-dependent external forces. Moreover, we find that this structural transition is accompanied by directed particle transport which is tuneable by changing external parameters.

Zusammenfassung

In dieser Arbeit wird das kollektive Verhalten kolloidaler Suspensionen auf der mesoskopischen Skala im Gleichgewicht sowie im Nichtgleichgewicht untersucht. In Anlehnung an kürzlich durchgeführte Experimente fokussieren wir uns im ersten Teil der Arbeit auf das Transportverhalten von Suspensionen mit rein repulsiv wechselwirkenden “weichen” Teilchen in engen, räumlich modulierten Kanalstrukturen. Basierend auf der modernen dynamischen Dichtefunktionaltheorie (DDFT) können wir erstmals den Einfluss von externen Kontrollschleifen mit zeitlicher Rückkopplung auf die Kolloid-Dynamik im Nichtgleichgewicht untersuchen. Für verschiedene experimentell zugängliche Kontrolltargets zeigen wir, dass die gezielte Manipulation des globalen Teilchenverhaltens möglich ist, darunter die Umkehr des Teilchenstroms und die Stabilisierung von raumzeitlichen Oszillationen. Im zweiten Teil der Arbeit finden wir durch Beimischung von magnetischen Teilchen mit klassischen Heisenbergspins eine spontane Strukturbildung, wobei magnetische und nichtmagnetische Domänen entstehen. In Abhängigkeit von Teilchendichte und -konzentration ergeben sich ein Entmischungsübergang erster Ordnung und ein Phasenübergang zweiter Ordnung für die Magnetisierung bei bestimmten magnetischen Kopplungskonstanten. Basierend auf klassischer und dynamischer Dichtefunktionaltheorie berechnen wir sowohl die Flüssig-Flüssig-Grenzfläche im Gleichgewicht als auch das Domänenwachstum im Nichtgleichgewicht. Für das Gleichgewichts-Phasendiagramm finden wir zwei verschiedene Phasenseparationsbereiche: die spinodale Entmischung und die Nukleation für energetisch aktivierte Wachstumsprozesse. Basierend auf der DDFT zeigen wir, dass das Wachstum in der spinodalen Entmischung systematisch einem Power-Law-Verhalten folgt mit einem Exponenten, der mit Vorhersagen aus klassischen Überlegungen übereinstimmt. Für die Nukleation im Nichtgleichgewicht präsentieren wir neue Resultate zum physikalischen Pfad ins Gleichgewicht, wobei wir als Koordinaten die Barrierenenergie und die Teilchenexzesszahl wählen. Im letzten Teil der Arbeit demonstrieren wir, dass das Strukturbildungsverhalten im Nichtgleichgewicht gezielt mit zeitabhängigen externen Substratfeldern beeinflusst werden kann. Für eine neuartige dynamische Instabilität, bei der sich Streifen entgegen der Symmetrie des externen Potentials ausbilden, zeigen wir, dass der zugrundeliegende physikalische Mechanismus auf ein Wechselspiel zwischen der spinodalen Entmischung und der gewählten externen Kraft

beruht. Zudem stellt sich heraus, dass der Strukturübergang mit einem gerichteten Teilchentransport verbunden ist, der sich mit äusseren Parametern einstellen lässt.

Publications

Parts of the results presented in this thesis have been published in the following peer-reviewed journals:

Ken Lichtner and Sabine H. L. Klapp

Novel Structure Formation of a Phase Separating Colloidal Fluid in a Ratchet Potential
Europhys. Lett. **106 56004** **June 2014**

Ken Lichtner and Sabine H. L. Klapp

Spinodal Decomposition of a Binary Magnetic Fluid Confined to a Surface
Phys. Rev. E **88 032301** **September 2013**

Ken Lichtner, Andrey Pototsky and Sabine H. L. Klapp

Feedback-induced Oscillations in One-dimensional Colloidal Transport
Phys. Rev. E **86 051405** **November 2012**

Ken Lichtner, Andrew J. Archer, and Sabine H. L. Klapp

Phase Separation Dynamics in a Two-Dimensional Magnetic Mixture
J. Chem. Phys. **136 024502** **January 2012**

Ken Lichtner and Sabine H. L. Klapp

Feedback-Controlled Transport in an interacting Colloidal System
Europhys. Lett. **92 40007** **December 2010**

1. Introduction

This chapter is intended to introduce the reader to the subject of colloidal dispersions. Besides discussing basic concepts and definitions concerning their theoretical description we will address some recent major developments. This thesis focuses mainly on the non-equilibrium behavior of colloids and their manipulation thereof. In particular, we investigate phenomena ranging from transport in narrow channels to pattern formation at surfaces under *time-dependent* fields. Within this context, one traditionally employs so called “open-loop” control schemes, that is, manipulating the system behavior through external parameters (e.g., by tuning external electric or magnetic fields or the temperature). We also make some first steps towards novel “closed-loop” or “feedback” control strategies which depend on the state of the system. In the following, we will discriminate between both approaches.

1.1. Colloidal suspensions: A short overview

In the past few decades, the investigation of colloidal systems received increasing attention from scientists with a variety of backgrounds, including applied mathematicians, chemists, physicists and (bio-)engineers. A colloidal suspension is a system where nano- to micrometre-sized objects of condensed matter (“the colloids”) are dispersed in a continuous liquid phase consisting of (atomic-sized) solvent molecules. It is the interplay between the dimensions (and *not* the shapes) that allows for a fascinating phenomenon: Due to the random collisions with the solvent molecules, the colloids perform irregular shivering movements known under “Brownian motion”. Looking at these movements closely through an optical microscope reveals that the displacements are undirected. Yet, as predicted independently by Einstein in 1905 [1] and Smoluchowski one year later [2], the squared mean displacement grows for $t \gg \tau_B$ systematically with time. The experimental verification of this phenomenon (which indirectly confirms the existence of atoms and molecules) was provided by Perrin a few years later in 1909 [3]. In a theoretical approach, one defines a time scale τ_B corresponding to the time a particle needs to diffuse over its own diameter. This “Brownian time scale” is typically of order $\sim 10^{-9}$ s for colloids. At times larger

than τ_B , the momentum degrees of freedom of the colloids are in equilibrium with the solvent [4]. Thus, on this time scale, one can consider the “overdamped” motion of the colloids neglecting inertial effects as in most theoretical approaches so far. In these models, the solvent molecules are “integrated out” meaning that the solvent appears only in an implicit manner.

Examples for colloidal suspensions appearing in our daily surroundings are manifold, including familiar products such as milk, paint and shampoo. On the other hand, due to the advances in chemical engineering over the last decades, a large variety of synthesized suspensions with tailored physical properties exist. The cores of these mesoscopic particles range from rigid (*hard*) spheres such as silica [5], PMMA [6], or polystyrene [7] to penetrable (*soft*) particles such as star polymers [8] or dendrimers [9]. Examples for aspherical particles, i.e. particles with shape-anisotropy are colloidal rods [10] or dumbbells [11]. Besides designing different shapes, a special emphasis in colloid science is placed on tuning the interactions between particles, e.g., by functionalizing the particles with surface charges. In theoretical approaches, the interactions between such particles are modeled with (effective) pair potentials involving long-ranged, electrostatic interactions such as the Coulomb interaction [12] or dipole-dipole interactions originating from electric or magnetic dipole moments [13]. More recently, a wide class of patchy particles is a topic under focus where the interaction anisotropy is highly tunable (for an overview, see references [14; 15]).

1.2. From equilibrium phase behavior to pattern formation

A very fascinating aspect of colloidal suspensions is that they display a rich phase behavior depending on the details of the system. Even the simplest suspensions of spherical colloidal particles interacting through a steep repulsive repulsion (“hard spheres”) exhibit phase transitions between solid, liquid and glass phases [16; 17]. By supplementing the hard spheres with additional short-range particle attractions (e.g., by functionalizing PMMA particles with polystyrene [18]), the phase behavior is enriched by vapour, gel [19], and higher-order glass phases displaying reentrant phenomena [20].

Correspondingly, more complex behavior is observed for particles with internal degrees of freedom such as magnetic particles [21; 22] and mixtures involving shape-anisotropic particles such as colloidal rods [23]. From the theoretical side, the equilibrium properties of one-component Heisenberg fluids [24; 25; 26; 27; 28], as well as other

spin fluids with two-dimensional [29] (XY) and Ising spins and mixtures thereof have been extensively studied by MC simulations, integral equation methods, and (mean field) density functional theories (see reference 30). These systems display a rich variety of first-order phase transitions between solid, liquid, and vapour as well as second-order transitions between ordered and disordered phases. In fact, even simple mixtures consisting of spherical particles display non-trivial phase behavior including triple points and critical end points not present for one-component systems [31; 32; 33; 34]. In a more general sense, pattern formation may occur in a class of systems with competing interactions [35; 36]; examples include charged colloidal systems [37; 38], colloidal clays [39], or binary complex plasmas [40]. Examples the structure formation is purely imposed through the interaction with a surrounding media include micelles (i.e., colloids with hydrophobic and hydrophilic sides) or the self-assembling colloids deposited on structured surfaces or thin liquid films such as, e.g., in the Langmuir-Blodgett transfer [41] or magnetic garnet films [42; 43; 44].

Particularly interesting are systems where the occurrence of patterns can be manipulated by tuning only external parameters (thus involving “open-loop” schemes). A paradigm example are systems where the structure formation is driven by an underlying phase separation such as, e.g., in colloids with Lennard-Jones type of interaction [45] or binary mixtures [34; 33]. For the latter, it is the temperature or the chemical potential that can be used as control parameters for a quench into the two-phase region. Another interesting example for systems subject of manipulation with “open-loop” schemes are classical spin fluids. Indeed, the impact of static, homogeneous fields on the magnetic phase transition of interacting spin fluids has been investigated, in particular, by Omelyan, Folk and coworkers based on Monte Carlo simulations [46] and (modified) integral equation methods [30; 29]. One inherent systematic feature is that the critical temperature T_c for the continuous para-ferromagnetic transition decreases with turning on and increasing an external field. However, depending on the spin dimensionality f the response of the system to a field of strength H can be more complicated. Indeed, while T_c decreases monotonically with H for $f = 1$ (Ising), a sudden increase of T_c is being observed for the cases $f = 2$ and $f = 3$ (XY and Heisenberg) at very strong fields H [46]. While the impact of static fields on classical spin structures has been intensively studied, the interplay between *time-dependent* fields and magnetic systems undergoing a phase separation, however, is essentially unexplored.

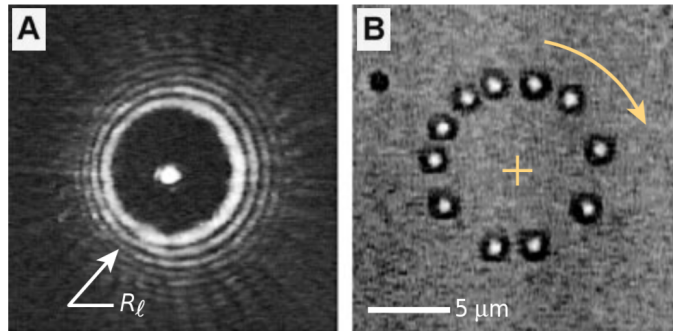


Figure 1.: (a) *Optical vortices created from helical modes of light and (b) a single trapped colloid moving in an optical vortex. Taken from reference [47].*

1.3. Systems driven out of equilibrium

In the context of non-equilibrium phenomena so far, the Brownian transport in complex geometry has been studied intensively with applications in diverse fields such as biology, condensed matter and nanotechnology [48; 49; 50]. A large number of studies has been devoted to the dynamics in structured systems such as colloids or biomolecules in microchannels [51], colloids in optical potentials [52; 53; 54; 55], or cold atoms in optical lattices [56]. Depending on the details of the external potential, a variety of spectacular effects have been observed. Most prominent examples are giant diffusion [57] and dispersionless transport [58] for symmetric systems under constant external bias (“tilted washboards”), or ratchet mechanisms, i.e., fluctuating-induced transport for systems with asymmetric spatial potential [50]. Anomalous, subdiffusive transport may be found, e.g., in crowded biological media [59], dipolar systems with field-aligned particles [60] or amorphous materials near the glass transition [61; 62]. Even paradoxical behavior such as a net motion of particles against the direction of a constant force (“negative mobility effect”) has been reported for charged beads subject to ac-fields [51; 63]. Many of these effects have also been observed experimentally (see, e.g., references [52; 53; 63; 64]), often involving colloidal systems (see figure 1 for an example where colloids are trapped in optical fields).

A related topic is how these non-equilibrium phenomena can be manipulated by control forces [66]. Particularly promising is *feedback control*, i.e. a closed-loop scheme where the control force depends on the state of the system. A special case is the time-delayed feedback control method suggested by Pyragas [67], where the control term involves the difference between an output variable (the control target) at time t

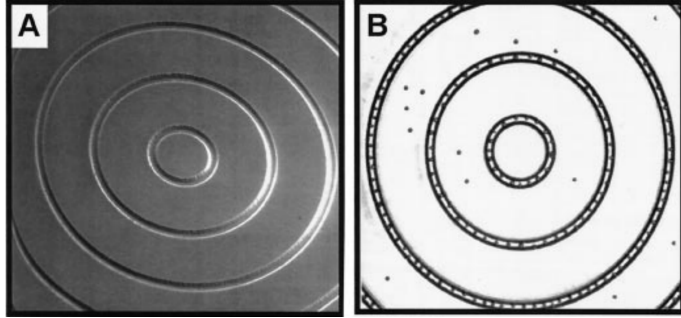


Figure 2.: (a) Scanning electron microscope image of 1d trenches etched by photolithography and (b) video microscope image of colloids confined in circular channels. Taken from reference [65].

and its value at time $t - \tau$, with τ being the delay time. This method is particularly suitable to stabilize certain, otherwise unstable periodic states [68]. Moreover, a time delay naturally occurs in experiments involving feedback control due to the lag between the collection of information and the feedback. Indeed, time-delayed feedback control is nowadays used in a broad variety of non-linear systems such as lasers, neural dynamics, and excitable macroscopic media [68]. In the area of transport, this method has already been applied, on a theoretical level, to Brownian motors (driven by an unbiased, time-periodic force) [69], systems rectified by delayed correlated noise [70], and flashing ratchets involving asymmetric, time-dependent potentials [66; 71]. Very recently, feedback strategies with delay have also been explored, on the basis of Langevin equations [72; 73], as a tool to manipulate the particle current in tilted washboard potentials. However, despite intense research we are still far away from a full understanding of the usefulness of control schemes in transport processes and its potential applications in biology and nanotechnology.

1.4. Motivation, goals and structure of this thesis

The purpose of this thesis is to address the non-equilibrium dynamics of one- and two-component liquid suspensions under time-dependent external fields. We investigate different geometries, including infinite systems representing colloidal particles on a ring (see figure 2 for an experiment), and finite microchannel geometries [74]. We aim at developing novel control schemes (including such of closed-loop type) based on quantities that are directly accessible in experiments. The major control goals

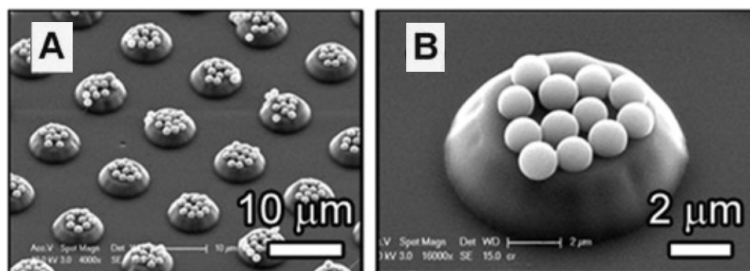


Figure 3.: Scanning electron microscope image showing magnetic assembly of beads after drying. Taken from reference [77].

in this context are the manipulation of the transport behavior and the stabilization of dynamical non-equilibrium states. A second major goal is to analyze and control the dynamic patterns arising from phase separating mixtures confined in liquid thin films or surfaces (2D). To this end, we consider a binary mixture of magnetic and non-magnetic particles. Indeed, pattern selection in the present context is essential for a variety of applications such as, e.g., the fabrication of (colloidal) magnetic storage media [75] or sorting devices based on the controlled transport of magnetic particles [76]. Our investigations are mainly based on static conventional density functional theory (DFT) and its dynamical extension, DDFT.

After introducing the theoretical background in chapter 2, we start our investigations in chapter 3 with the simplest possible non-equilibrium models for colloids, that is, a system of *non-interacting* colloids where the external force is exerted by a static modulated potential. In order to control the transport in this washboard potential, we supplement by a closed-loop feedback control force. Indeed, we find that the particle current in our strongly correlated system can be efficiently controlled via time-delayed feedback schemes focusing either on the average particle position or directly on the density profile. We then go one step further and ask to which extent the time-delayed feedback control can induce dynamic states *not seen* in the uncontrolled system, which involves the purely static washboard potential. Specifically, we search for the existence of spatiotemporal structures characterized by an *oscillatory* distribution of particles. That time-delayed feedback control itself can indeed generate novel dynamics has recently also been seen in other extended systems [78]. Moreover, we show that the existence and stability of the oscillatory distribution density strongly depends on the properties of the periodic energy landscape that describes the interaction between the particle and the channel walls. The energy landscape is, in turn, directly linked to the properties of the individual particles, such as, for instance, the (gyration) radius of the

particles. As a consequence, the proposed time-delayed feedback control can be used as a filter in order to separate particles of different size. The underlying mechanism is somewhat similar to the well-studied symmetry-selected sorting of particles in periodic potential landscapes [79; 80].

In chapter 4, we introduce a second species with the goal of inducing phase separation in the system. Specifically, we consider one of the simplest examples of mixtures with internal degrees of freedom, that is, a binary fluid of spherical particles where one species carries a classical three-dimensional Heisenberg spin. The particles are confined in a thin liquid film (2d). This situation is actually close to many experiments (see, e.g., reference 21 and figure 3) and has the advantage that the calculated structure can be easily visualized. Within the vast parameter space characterizing our model, we focus on a situation where the system demixes into a non-magnetic and a ferromagnetic phase. For this situation, we first use conventional static DFT to calculate a complete phase diagram involving a first-order transition and a tricritical point, as well as the inhomogeneous fluid density and magnetization profiles characterizing the liquid-liquid interface. Based on this information we then consider the phase separation dynamics, focusing on both nucleation phenomena and spinodal decomposition. For the nucleation, we compare the results of three different approaches, namely classical nucleation theory, which is based on macroscopic concepts, an approach based on equilibrium DFT, and finally DDFT. In order to gain more structural information about the underlying phase-separating process, we proceed with the calculation of dynamic correlation functions based on Percus' test particle limit [81], that is, identifying the van Hove dynamic correlation function with one-body density distributions of a mixture [82; 83]. The equivalent function of the dynamic correlation function $G(\mathbf{r}, t)$ in momentum space is the dynamic structure factor $S(\mathbf{k}, t)$ which we utilize to investigate, in particular, the time-dependence of the average domain size. We also compare the DDFT predictions to those from a simpler, mean-field like ("Vineyard") approach.

In chapter 5, we study the impact of a time-dependent magnetic ratchet potential (serving as an open-control scheme) on the collective behavior, specifically the phase separation dynamics, of the mixture. Indeed, recent experimental and theoretical research has shown that magnetic colloidal systems are ideally suited to study transport in such complex geometry. Static, magnetic periodic potentials can be created, e.g., by using ferrite garnet films [42; 43] or by using a periodic arrangement of micromagnets on "lab-on-a-chip" devices [84; 85; 86]. An additional time-dependent (oscillating) field can be introduced by combining the static potential with a rotating magnetic field [84; 43; 42; 85; 87]. The latter yields a periodic increase (decrease) of the size of domains with parallel (antiparallel) magnetization, which eventually enables transport. From an applicational point of view, a particular attractive feature is that

the average velocity of the particles depends on the frequency of the rotating field as well as on the particle geometry [84; 87]. Moreover, contrary to electric fields, the properties of magnetic substrate fields can be changed on the fly (if the frequency is sufficiently small), which is an important prerequisite for transport of sensitive objects such as living cells [88; 84]. So far, most theoretical studies in this area have been undertaken for *single* colloids or systems with negligible interactions. This is in contrast to indications from experiments, which suggest that interaction effects could be important for the transport in magnetic ratchets [87] and the self-assembly of particles into patterns on magnetic lattices [89]. We illuminate this gap by considering also the interacting system with our theoretical approach.

In chapter 6, we close this thesis with concluding remarks and discuss several directions which are interesting for further investigation.

2. Theory

2.1. Equilibrium theory of the many-body system

In this chapter we introduce the Hamiltonian for the interacting many-body system. Starting from this microscopic basis we derive a variational principle for the one-body density distribution which is known as classical density functional theory (DFT). After applying the DFT scheme for a simple case, we show that correlation functions are linked to the functional derivatives of the free energy. DFT is thus an equilibrium theory that mediates between structural changes of a fluid and its thermodynamical quantities.

2.1.1. Many-body Hamiltonian

The microscopic Hamiltonian for a N -body system has three contributions,

$$\mathcal{H}_N(\mathbf{r}^N, \mathbf{p}^N) = T(\mathbf{p}^N) + U(\mathbf{r}^N) + V(\mathbf{r}^N), \quad (1)$$

where $\mathbf{r}^N = \{\mathbf{r}_1, \mathbf{r}_2, \dots, \mathbf{r}_N\}$ and $\mathbf{p}^N = \{\mathbf{p}_1, \mathbf{p}_2, \dots, \mathbf{p}_N\}$ are sets of coordinates and momenta. The first contribution in equation (1), $T(\mathbf{p}^N) = \sum_{i=1}^N \mathbf{p}_i^2 / (2m)$, is the kinetic energy (with m being the mass and \mathbf{p}_i being the momentum of particle i), the second contribution accounts for the potential energy arising from particle interactions, and the third is the external potential contribution stemming from an arbitrary external, locally varying field $\phi^{\text{ext}}(\mathbf{r})$. We assume that the latter is a one-body field, i.e. the total contribution is just the sum over $\phi^{\text{ext}}(\mathbf{r})$ evaluated at the positions, that is,

$$V^{\text{ext}}(\mathbf{r}^N) = \sum_{i=1}^N \phi^{\text{ext}}(\mathbf{r}_i). \quad (2)$$

For fields of this type it is useful to introduce the particle density operator for N identical particles,

$$\hat{\rho}(\mathbf{r}) = \sum_{i=1}^N \delta(\mathbf{r} - \mathbf{r}_i). \quad (3)$$

By employing equation (3), we can convert the sum in equation (2) into an (often) easier to handle integral depiction, that is,

$$V^{\text{ext}}(\mathbf{r}^N) = \sum_{i=1}^N \phi^{\text{ext}}(\mathbf{r}_i) = \sum_{i=1}^N \int d\mathbf{r} \delta(\mathbf{r} - \mathbf{r}_i) \phi^{\text{ext}}(\mathbf{r}) = \int d\mathbf{r} \hat{\rho}(\mathbf{r}) \phi^{\text{ext}}(\mathbf{r}). \quad (4)$$

Examples for the one-body potential $\phi^{\text{ext}}(\mathbf{r})$ in equation (4) include confinement potentials ensuring that the system volume V is finite (e.g., “hard wall” potentials), or a surrounding static field which couples to the (electric or magnetic) moments of the particles.

2.1.2. Grand potential functional

The many-body equilibrium probability distribution for a N -body system at fixed temperature T , volume V , and chemical potential μ is given in the grand canonical ensemble by

$$f_0 = \frac{\exp(-\beta(\mathcal{H}_N - \mu N))}{\Xi_{\text{gc}}}, \quad (5)$$

where \mathcal{H}_N is the microscopic Hamiltonian [see equation (1)], and $\beta = 1/(k_B T)$, with k_B being Boltzmann’s constant. The grand canonical partition sum in equation (5) counts all possible microstates in the phase space corresponding to fixed values of (T, V, μ) weighted by a Boltzmann factor, that is,

$$\Xi_{\text{gc}} = \text{Tr} \exp(-\beta(\mathcal{H}_N - \mu N)). \quad (6)$$

In equation (6) the symbol Tr denotes the classical trace, that is,

$$\text{Tr} = \sum_{N=0}^{\infty} \frac{1}{h^{3N} N!} \int d\Gamma_N, \quad (7)$$

where h is Planck’s constant, and $\Gamma_N = (\mathbf{r}_1, \dots, \mathbf{r}_N, \mathbf{p}_1, \dots, \mathbf{p}_N)$ represents a set consisting of all particle positions and momenta. Evans proposed to rewrite the grand

potential as a functional of the many-body probability distribution, that is, [45]

$$\Omega[f] = \text{Tr} f(\mathcal{H}_N - \mu N + \beta^{-1} \ln f), \quad (8)$$

where f denotes an arbitrary “trial” distribution satisfying the normalization condition $\text{Tr} f=1$. The link to the equilibrium grand potential Ω_0 is established by inserting the equilibrium density distribution into equation (8), that is, [45]

$$\begin{aligned} \Omega[f_0] &= \text{Tr} f_0(\mathcal{H}_N - \mu N + \beta^{-1} \ln f_0) \\ &= \text{Tr} f_0(\mathcal{H}_N - \mu N + \beta^{-1}(-\beta(\mathcal{H}_N - \mu N) - \ln \Xi_{\text{gc}})) \\ &= -\beta^{-1} \ln \Xi_{\text{gc}} \\ &= \Omega_0. \end{aligned} \quad (9)$$

The central property of the functional (8) is that it satisfies a variational principle, i.e.,

$$\Omega[f] > \Omega[f_0], \quad \text{for } f \neq f_0. \quad (10)$$

The inequality (10) can be proven by employing the Gibbs-Bogoliubov relation [see App. I for the proof].

2.1.3. Hohenberg-Kohn variational principle for the one-body density

The functional (8) was originally formulated by Mermin [90] for non-classical electronic systems. For the description of classical fluids we have to reformulate the variational principle in terms of a classical distribution function. We will do so by following the major steps of reference [45].

The equilibrium one-body density $\rho_0(\mathbf{r})$ is defined as the ensemble average of the particle density operator [see equation (3)], that is,

$$\rho_0(\mathbf{r}) = \text{Tr} f_0 \hat{\rho}(\mathbf{r}) = \left\langle \sum_{i=1}^N \delta(\mathbf{r} - \mathbf{r}_i) \right\rangle_{\text{gc}}, \quad (11)$$

where the index “gc” indicates that we take the average in the grand canonical ensemble. Note that the probability distribution f_0 (as introduced in section 2.1.2) is already a functional of the external potential $V^{\text{ext}}(\mathbf{r})$ through the many-body Hamiltonian \mathcal{H}_N . However, we still have to prove that the function $\rho_0(\mathbf{r})$ is uniquely linked to V^{ext} . A

possible way to show this is a proof by contradiction [45]:

We assume that two different external potentials, V^{ext} and \tilde{V}^{ext} , lead to the exact same equilibrium density, $\rho_0(\mathbf{r})$, that is,

$$\begin{aligned}\rho_0(\mathbf{r}) &= \text{Tr} f_0 \hat{\rho}(\mathbf{r}) = \text{Tr} \tilde{f}_0 \hat{\rho}(\mathbf{r}) \\ &= \langle \hat{\rho}(\mathbf{r}) \rangle_{f_0} = \langle \hat{\rho}(\mathbf{r}) \rangle_{\tilde{f}_0}.\end{aligned}\quad (12)$$

The corresponding equilibrium probability distributions f_0 and \tilde{f}_0 enter the grand potential through equation (8),

$$\begin{aligned}\Omega[f_0] &= \text{Tr} f_0 (\mathcal{H}_N - \mu N + \beta^{-1} \ln f_0), \\ \Omega[\tilde{f}_0] &= \text{Tr} \tilde{f}_0 (\tilde{\mathcal{H}}_N - \mu N + \beta^{-1} \ln \tilde{f}_0),\end{aligned}\quad (13)$$

where \mathcal{H}_N and $\tilde{\mathcal{H}}_N$ differ only in the contribution from the external potential, that is,

$$\begin{aligned}\mathcal{H}_N &= T + U + V^{\text{ext}}, \\ \tilde{\mathcal{H}}_N &= T + U + \tilde{V}^{\text{ext}}.\end{aligned}\quad (14)$$

Since \tilde{f}_0 is not the equilibrium distribution corresponding to the Hamiltonian \mathcal{H}_N (neither does f_0 correspond to $\tilde{\mathcal{H}}_N$) it follows from the variational principle (10) that

$$\begin{aligned}\Omega[f_0] &< \text{Tr} \tilde{f}_0 (\mathcal{H}_N - \mu N + \beta^{-1} \ln \tilde{f}_0), \\ \Omega[\tilde{f}_0] &< \text{Tr} f_0 (\tilde{\mathcal{H}}_N - \mu N + \beta^{-1} \ln f_0).\end{aligned}\quad (15)$$

Employing equations (13-14) we may rewrite the right hand sides of (15), that is,

$$\begin{aligned}\text{Tr} \tilde{f}_0 (\mathcal{H}_N - \mu N + \beta^{-1} \ln \tilde{f}_0) &= \Omega[\tilde{f}_0] + \langle V^{\text{ext}} - \tilde{V}^{\text{ext}} \rangle_{\tilde{f}_0}, \\ \text{Tr} f_0 (\tilde{\mathcal{H}}_N - \mu N + \beta^{-1} \ln f_0) &= \Omega[f_0] + \langle \tilde{V}^{\text{ext}} - V^{\text{ext}} \rangle_{f_0},\end{aligned}\quad (16)$$

such that the latter inequalities read

$$\begin{aligned}\Omega[f_0] &< \Omega[\tilde{f}_0] + \langle V^{\text{ext}} - \tilde{V}^{\text{ext}} \rangle_{\tilde{f}_0}, \\ \Omega[\tilde{f}_0] &< \Omega[f_0] + \langle \tilde{V}^{\text{ext}} - V^{\text{ext}} \rangle_{f_0}.\end{aligned}\quad (17)$$

By adding both sides of (17) we obtain the relation

$$\Omega[f_0] + \Omega[\tilde{f}_0] < \Omega[f_0] + \Omega[\tilde{f}_0] + \langle V^{\text{ext}} - \tilde{V}^{\text{ext}} \rangle_{\tilde{f}_0} + \langle \tilde{V}^{\text{ext}} - V^{\text{ext}} \rangle_{f_0}. \quad (18)$$

Relation (18) gives only rise to a true result if the sum over the external potential averages on the right hand side is positive. However, from the assumption (12) it follows for the averaging process that its result does not change if f_0 is being used instead of \tilde{f}_0 , such that

$$\begin{aligned} \langle V^{\text{ext}} - \tilde{V}^{\text{ext}} \rangle_{\tilde{f}_0} + \langle \tilde{V}^{\text{ext}} - V^{\text{ext}} \rangle_{f_0} &= \langle V^{\text{ext}} - \tilde{V}^{\text{ext}} + \tilde{V}^{\text{ext}} - V^{\text{ext}} \rangle_{f_0} \\ &= \langle V^{\text{ext}} - \tilde{V}^{\text{ext}} + \tilde{V}^{\text{ext}} - V^{\text{ext}} \rangle_{\tilde{f}_0} = 0. \end{aligned} \quad (19)$$

Thus, the assumption (12) leads to a contradiction,

$$\Omega[f_0] + \Omega[\tilde{f}_0] < \Omega[f_0] + \Omega[\tilde{f}_0], \quad (20)$$

and must therefore be wrong. From this fact we can draw the opposite conclusion, namely that the probability density f_0 (and through that the function V^{ext}) must be *uniquely* linked to the equilibrium density $\rho_0(\mathbf{r})$. Another consequence is that the functional $\Omega[\rho(\mathbf{r})]$ is also unique with respect to any considered “trial” density $\rho(\mathbf{r})$ [45]. Moreover, from relation (10) follows a variational principle for the quantity $\rho(\mathbf{r})$, that is,

$$\Omega[\rho(\mathbf{r})] > \Omega[\rho_0(\mathbf{r})], \quad \text{for } \rho(\mathbf{r}) \neq \rho_0(\mathbf{r}). \quad (21)$$

From relation (21) it follows that the equilibrium density $\rho_0(\mathbf{r})$ minimizes the grand potential, that is,

$$\left. \frac{\delta \Omega}{\delta \rho(\mathbf{r})} \right|_{\rho_0(\mathbf{r})} = 0, \quad \Omega[\rho_0(\mathbf{r})] = \Omega_0. \quad (22)$$

2.1.4. Ideal gas limit

In this section we exemplarily consider the Hamiltonian for a gas of non-interacting Brownian particles in the canonical ensemble, that is,

$$\mathcal{H}_N = \sum_{i=1}^N \mathbf{p}_i^2 / 2m, \quad (23)$$

where \mathbf{p}_i is the momentum of the i -th particle with mass m . At first, we neglect the impact from external fields of any kind (e.g., gravitational fields). In this case, the Helmholtz free energy for the ideal gas can be calculated analytically through the

canonical partition sum, that is,

$$\mathcal{F}^{\text{id}} = -\beta^{-1} \ln \Xi_c^{\text{id}} = -\beta^{-1} \ln \frac{1}{h^{3N} N!} \int d\mathbf{r}^N \int d\mathbf{p}^N \exp \left(-\beta \sum_{i=1}^N \mathbf{p}_i^2 / 2m \right). \quad (24)$$

The integration over the positions can be carried out explicitly, $\int d\mathbf{r}^N = V^N$ (where V is the volume of the system), and the integration over the momenta yields

$$\mathcal{F}^{\text{id}} = -\beta^{-1} \ln \frac{V^N}{h^{3N} N!} \int d\mathbf{p}^N \exp \left(-\beta \sum_{i=1}^N \mathbf{p}_i^2 / 2m \right) = -\beta^{-1} \ln \frac{V^N}{\lambda^{3N} N!}, \quad (25)$$

where $\lambda = h/\sqrt{2\pi m k_B T}$ is the thermal de Broglie wavelength. For large particle numbers N , we can apply Stirling's approximation to the right hand side of equation (25), $\ln N! \simeq N \ln N - N$, that is,

$$\mathcal{F}^{\text{id}} = N\beta^{-1}(\ln(\lambda^3 N/V) - 1) = N\beta^{-1}(\ln(\lambda^3 \rho_0) - 1), \quad (26)$$

where $\rho_0 = N/V$ is the equilibrium density of the ideal gas. Note that we omitted in equation (26) a symbol which signifies that both sides are only *approximately* equal. The reason relies on the fact that Stirling's approximation is very accurate even for small particle numbers, e.g., the relative error is less than one percent for $N = 100$ (note that N is typically much larger for colloidal suspensions, e.g., the study [91] employs magnetic particles where $N = 6 - 7 \times 10^8$ per ml solution).

In presence of a locally varying external field, the equilibrium density becomes inhomogeneous. One then heuristically replaces the particle number in equation (26) by an integral over the density, i.e. $N = \int d\mathbf{r} \rho(\mathbf{r})$ [45]. The external field contribution to the free energy is obtained by taking the ensemble average of equation (4). The ideal gas free energy then reads

$$\begin{aligned} \mathcal{F}[\rho(\mathbf{r})] &= \mathcal{F}^{\text{id}}[\rho(\mathbf{r})] + \mathcal{F}^{\text{ext}}[\rho(\mathbf{r})] \\ &= \beta^{-1} \int d\mathbf{r} \rho(\mathbf{r}) (\ln(\lambda^3 \rho(\mathbf{r})) - 1) + \int d\mathbf{r} \rho(\mathbf{r}) \phi^{\text{ext}}(\mathbf{r}). \end{aligned} \quad (27)$$

The grand potential is obtained by performing a Legendre transform with respect to the particle number N , that is,

$$\Omega[\rho(\mathbf{r})] = \mathcal{F}[\rho(\mathbf{r})] - \mu \int d\mathbf{r} \rho(\mathbf{r}), \quad (28)$$

where μ is the chemical potential. Performing the functional minimization (22) yields the Euler-Lagrange equations for μ ,

$$\mu = \mu^{\text{id}}[\rho_0(\mathbf{r})] + \phi^{\text{ext}}(\mathbf{r}), \quad (29)$$

where $\mu^{\text{id}} = \delta\mathcal{F}^{\text{id}}/\delta\rho(\mathbf{r}) = \beta^{-1} \ln(\lambda^3\rho(\mathbf{r}))$ is the exact ideal gas contribution. Solving equation (29) for $\rho_0(\mathbf{r})$ leads to the expression

$$\rho_0(\mathbf{r}) = \lambda^{-3} \exp(\beta\mu) \exp(-\beta\phi^{\text{ext}}(\mathbf{r})). \quad (30)$$

Equation (30) is the exact equilibrium solution for the non-interacting gas. Since we have shown in section 2.1.3 that ρ_0 is uniquely linked to ϕ^{ext} , we can consider the solution together with an arbitrary one-body field ϕ^{ext} . For example, in the case of earth's gravitational field, we obtain from equation (30) the barometric formula¹ by inserting $\phi^{\text{ext}} = mgh$. It is a central advantage of DFT that this ‘‘Hohenberg-Kohn property’’ also holds for the interacting case.

2.1.5. Excess free energy

In the case of an interacting system, we have to extend the free energy with a term corresponding to the interaction potential $U(\mathbf{r}^N)$. To this end, one defines an excess (over ideal gas) part \mathcal{F}^{ex} which contributes to the free energy functional (27), that is, [45]

$$\mathcal{F}[\rho(\mathbf{r})] = \mathcal{F}^{\text{id}}[\rho(\mathbf{r})] + \mathcal{F}^{\text{ext}}[\rho(\mathbf{r})] + \mathcal{F}^{\text{ex}}[\rho(\mathbf{r})]. \quad (31)$$

For the construction of $\mathcal{F}^{\text{ex}}[\rho(\mathbf{r})]$ it is useful to introduce an effective one-body potential $c^{(1)}$ (also named the ‘‘direct correlation function’’ [92]) that is linked to the excess chemical potential through the relation,

$$c^{(1)}[\rho(\mathbf{r})] \equiv \beta\mu^{\text{ex}}[\rho(\mathbf{r})] = \beta \frac{\delta\mathcal{F}^{\text{ex}}[\rho(\mathbf{r})]}{\delta\rho(\mathbf{r})}. \quad (32)$$

In the case of pairwise interacting particles, the pair potential can be expressed as the sum of a reference part and a perturbation part, that is, [92; 45]

$$v_2(\mathbf{r}, \mathbf{r}', \lambda) = v_{\text{ref}}(\mathbf{r}, \mathbf{r}') + \lambda v_{\text{pert}}(\mathbf{r}, \mathbf{r}'), \quad (33)$$

¹where $\rho_0 \equiv \lambda^{-3} \exp(\beta\mu)$ is the density at the surface

where $0 \leq \lambda \leq 1$ is a perturbation parameter that gradually “charges” between a reference system ($\lambda = 0$) and a fully perturbed system ($\lambda = 1$). For example, for a system of interacting particles of Lennard-Jones type, the reference part $v_{\text{pert}}(\mathbf{r}, \mathbf{r}')$ represents the repulsive core-core forces (e.g., described by an effective soft or hard core potential) while the attractive part of the effective potential can be treated successfully as a perturbation $v_{\text{pert}}(\mathbf{r}, \mathbf{r}')$ (e.g., see reference [92]). Integrating then equation (32) yields

$$\begin{aligned} \mathcal{F}^{\text{ex}}[\rho(\mathbf{r})] &= \mathcal{F}_0^{\text{ex}}[\rho(\mathbf{r})] + \frac{1}{2} \int_0^1 d\lambda \int d\mathbf{r} \int d\mathbf{r}' \rho^{(2)}(\mathbf{r}, \mathbf{r}', \lambda) v_{\text{pert}}(\mathbf{r}, \mathbf{r}') \\ &= \mathcal{F}_0^{\text{ex}}[\rho(\mathbf{r})] + \frac{1}{2} \int_0^1 d\lambda \int d\mathbf{r} \int d\mathbf{r}' \rho(\mathbf{r}) \rho(\mathbf{r}') g(\mathbf{r}, \mathbf{r}', \lambda) v_{\text{pert}}(\mathbf{r}, \mathbf{r}'). \end{aligned} \quad (34)$$

In equation (34) $\rho^{(2)}(\mathbf{r}, \mathbf{r}', \lambda)$ [$g(\mathbf{r}, \mathbf{r}', \lambda)$] is the two-body density [pair distribution function] for the system interacting through the pair potential $v_2(\mathbf{r}, \mathbf{r}', \lambda)$. In order to quantify the spatial correlation between pairs of particles located at positions \mathbf{r} and \mathbf{r}' , one introduces the pair correlation function, that is, [92]

$$h(\mathbf{r}, \mathbf{r}', \lambda) = g(\mathbf{r}, \mathbf{r}', \lambda) - 1. \quad (35)$$

Note that $h(\mathbf{r}, \mathbf{r}', \lambda)$ vanishes for all pair potentials in the limit $|\mathbf{r} - \mathbf{r}'| \rightarrow \infty$ (also known as the ideal gas limit). Applying equation (35) to equation (34) leads to a division of the excess free energy into three parts, that is,

$$\begin{aligned} \mathcal{F}^{\text{ex}}[\rho(\mathbf{r})] &= \mathcal{F}_0^{\text{ex}}[\rho(\mathbf{r})] + \mathcal{F}^{\text{corr}}[\rho(\mathbf{r})] + \mathcal{F}^{\text{uncorr}}[\rho(\mathbf{r})] \\ &= \mathcal{F}_0^{\text{ex}}[\rho(\mathbf{r})] + \frac{1}{2} \int_0^1 d\lambda \int d\mathbf{r} \int d\mathbf{r}' \rho(\mathbf{r}) \rho(\mathbf{r}') h(\mathbf{r}, \mathbf{r}', \lambda) v_{\text{pert}}(\mathbf{r}, \mathbf{r}') \\ &\quad + \frac{1}{2} \int d\mathbf{r} \int d\mathbf{r}' \rho(\mathbf{r}) \rho(\mathbf{r}') v_{\text{pert}}(\mathbf{r}, \mathbf{r}'). \end{aligned} \quad (36)$$

In equation (36) the term $\mathcal{F}^{\text{uncorr}}$ accounts for the excess contribution stemming from uncorrelated pairs of particles (where $g(\mathbf{r}, \mathbf{r}', \lambda) \equiv 1$). We note that for weakly correlated suspensions such as soft sphere fluids at high densities the function $g(\mathbf{r}, \mathbf{r}', \lambda)$ decays to unity within interparticle distances $|\mathbf{r} - \mathbf{r}'|$ that correspond to a few particle diameters (e.g., see figure 2 in [93]). Moreover, in this case it follows from equation (36) that $\mathcal{F}^{\text{uncorr}} \gg \mathcal{F}^{\text{corr}}$, i.e. we can set $\mathcal{F}^{\text{corr}}[\rho(\mathbf{r})] \approx 0$. Approximations of the latter

type are called mean-field approximations which we will apply later within our DFT (and DDFT) approaches.

2.2. Relaxation dynamics of colloids in non-equilibrium

In this section we derive the dynamical density functional theory (DDFT) which will be used as a main tool in the following chapters. In the DDFT the microscopic interactions which determine the underlying system of discrete Brownian particles enter via a free energy functional. Therefore, DDFT has a bridging position between microscopic Langevin-equation based models and mesoscopic models for transport of continuous phases as will be shown below.

2.2.1. Overdamped Langevin equation

The overdamped dynamics of colloidal suspensions can be described on a microscopic level by a stochastic Langevin equation, that is,

$$\gamma \mathbf{v}_j(\mathbf{r}^N, t) = \mathbf{F}_j(\mathbf{r}^N, t) + \boldsymbol{\chi}_j(t), \quad (37)$$

where the friction constant is related to the diffusion constant through Einstein's relation $\gamma = k_B T / D_0$ [4]. Equation (37) expresses the balancing of viscous forces $\gamma \mathbf{v}_j$ with forces \mathbf{F}_j arising from interparticle interactions, external fields, and stochastic random forces $\boldsymbol{\chi}_j$. The latter are characterized by a zero mean and a short correlation time, that is,

$$\langle \boldsymbol{\chi}_j(t) \rangle = \mathbf{0}, \quad (38)$$

$$\langle \boldsymbol{\chi}_i(t) \boldsymbol{\chi}_j(t') \rangle = \mathbf{0} \quad \text{for } |t - t'| > \tau_c. \quad (39)$$

We can rewrite (39) by assuming that the correlation time τ_c is infinitesimally small (this approximation seems to be justified since τ_c is typically much smaller than the relaxation time of the velocities [94]), that is,

$$\langle \boldsymbol{\chi}_i(t) \boldsymbol{\chi}_j(t') \rangle = 2k_B T \gamma \delta_{ij} \delta(t - t') \mathbf{1}. \quad (40)$$

For the latter equation we have used the fact that the power spectrum of equation (39) is a constant which can be related to the friction constant through the fluctuation-dissipation theorem [92].

2.2.2. Dynamics of the probability density function

In this section we present an alternative description for the dynamics of interacting colloids provided by the probability density function $P(\mathbf{r}^N, t)$ which is the probability of finding N particles at a specific coordinate set \mathbf{r}^N at time t . The time evolution of $P(\mathbf{r}^N, t)$ is given by the Smoluchowski equation, that is, [4]

$$\frac{\partial P(\mathbf{r}^N, t)}{\partial t} = - \sum_{i=1}^N \nabla_i \cdot [\mathbf{v}_i P(\mathbf{r}^N, t)] \quad (41)$$

Equation (41) is a continuity equation for the interacting N -particle system with particle current

$$\mathbf{J}_i(\mathbf{r}^N, t) = \mathbf{v}_i(\mathbf{r}^N, t) P(\mathbf{r}^N, t), \quad (42)$$

where \mathbf{v}_i is the velocity of particle i . The velocity can be rewritten as a function of the interaction potential $U(\mathbf{r}^N, t)$ [see equation (1)], that is,

$$\mathbf{v}_i(\mathbf{r}^N, t) = \gamma^{-1} [-\nabla_j U(\mathbf{r}^N, t) - k_B T \nabla_i \ln P(\mathbf{r}^N, t)], \quad (43)$$

where the second term accounts for the (stochastic) thermal force. In the absence of interparticle interactions and external fields [i.e., setting the total interaction potential $U(\mathbf{r}^N, t) \equiv 0$ for all times t], equation (41) reduces to the diffusion equation for a system of N Brownian particles, that is,

$$\frac{\partial P(\mathbf{r}^N, t)}{\partial t} = k_B T \gamma^{-1} \sum_{i=1}^N \nabla_i^2 P(\mathbf{r}^N, t), \quad (44)$$

We note that the Smoluchowski depiction for Brownian motion is equivalent to the Langevin approach presented in section 2.2.1. In fact, this can be shown by averaging equation (41) with respect to the noise which yields a Fokker-Planck equation for the probability density function with the same particle current as in equations (42)-(43) (e.g., see reference [94]).

2.2.3. Dynamical density functional theory

Starting from the Smoluchowski equation, we proceed by deriving a Fokker-Planck equation for the one-body density $\rho(\mathbf{r}, t)$ by following reference [95], that is, integrating out the many-body Smoluchowski equation (41) together with the particle current

given by equations (42-43).

The microscopic definition of the time-dependent one-body density profile $\rho(\mathbf{r}, t)$ is given by the configurational average over the time-dependent N -particle density operator [see equation (3) for the static counterpart], $\hat{\rho}(\mathbf{r}, t) = \sum_{i=1}^N \delta(\mathbf{r} - \mathbf{r}_i(t))$, that is,

$$\rho(\mathbf{r}, t) = \left\langle \sum_{i=1}^N \delta(\mathbf{r} - \mathbf{r}_i(t)) \right\rangle. \quad (45)$$

We can relate this distribution to the probability density function by arbitrarily tagging one particle in the system and integrating out the remaining $(N - 1)$ particle positions, that is,

$$\rho(\mathbf{r}, t) = N \int d\mathbf{r}_2 \dots \int d\mathbf{r}_N P(\mathbf{r}^N, t). \quad (46)$$

The combinatorial prefactor N in equation (46) takes into account that all particles are indistinguishable. Similarly, the two-body density profile can be defined based on the microscopic density operator, that is,

$$\rho^{(2)}(\mathbf{r}, \mathbf{r}', t) = \left\langle \sum_{i=1}^N \sum_{j=1}^N \delta(\mathbf{r} - \mathbf{r}_i(t)) \delta(\mathbf{r}' - \mathbf{r}_j(t)) \right\rangle. \quad (47)$$

In analogy to equation (46), one obtains the same quantity by integrating the probability density function over $(N - 2)$ particle positions, that is,

$$\rho^{(2)}(\mathbf{r}, \mathbf{r}', t) = N(N - 1) \int d\mathbf{r}_3 \dots \int d\mathbf{r}_N P(\mathbf{r}^N, t). \quad (48)$$

Following this route, the n -particle density can be written as

$$\rho^{(n)}(\mathbf{r}^n, t) = \frac{N!}{(N - n)!} \int d\mathbf{r}_{n+1} \dots \int d\mathbf{r}_N P(\mathbf{r}^N, t). \quad (49)$$

Thus, a hierarchy of Fokker-Planck equations for $\rho^{(n)}(\mathbf{r}^n, t)$ can be generated by “integrating out” the Smoluchowski equation (41). We only show this here for the first member of the hierarchy², namely $\rho(\mathbf{r}, t) \equiv \rho^{(1)}(\mathbf{r}, t)$. Inserting the particle

²For a detailed discussion of the dynamics of the two-body density $\rho^{(2)}$ see reference [96]

current (42-43) into the Smoluchowski equation (41) and integrating over $(N - 1)$ particles yields

$$N \int d\mathbf{r}_2 \dots \int d\mathbf{r}_N \frac{\partial P(\mathbf{r}^N, t)}{\partial t} = \gamma^{-1} N \int d\mathbf{r}_2 \dots \int d\mathbf{r}_N \sum_{i=1}^N \nabla_i \cdot [k_B T \nabla_i + \nabla_i U(\mathbf{r}^N, t)] P(\mathbf{r}^N, t). \quad (50)$$

Assuming that the derivatives of $P(\mathbf{r}^N, t)$ exist and are continuous, we can exchange the order of integration and differentiation, which leads to the Fokker-Planck equation for $\rho(\mathbf{r}, t)$, that is,

$$\frac{\partial \rho(\mathbf{r}, t)}{\partial t} = \gamma^{-1} \sum_{i=1}^N \nabla_i \cdot [k_B T \nabla_i + \nabla_i U(\mathbf{r}^N, t)] \rho(\mathbf{r}, t). \quad (51)$$

In the limit $U(\mathbf{r}^N, t) \equiv 0$ equation (51) reduces to the diffusion equation which can be solved analytically. In the presence of interactions, on the other hand, no general analytical solution exists. This fact becomes more visible by rewriting the total interaction potential $U(\mathbf{r}^N, t)$ into a series of n -body potentials (where $n = 2, 3, \dots$) plus the external potential, that is,

$$U(\mathbf{r}^N, t) = \sum_{i=1}^N V_{\text{ext}}(\mathbf{r}_i, t) + \frac{1}{2} \sum_{\substack{i=1 \\ j \neq i}}^N v_2(\mathbf{r}_i, \mathbf{r}_j) + \frac{1}{6} \sum_{\substack{i=1 \\ j \neq i \\ k \neq j \neq i}}^N v_3(\mathbf{r}_i, \mathbf{r}_j, \mathbf{r}_k) + \text{higher terms}. \quad (52)$$

Inserting equation (52) into equation (50) yields

$$\begin{aligned} \gamma \frac{\partial \rho(\mathbf{r}_1, t)}{\partial t} = & k_B T \nabla_1^2 \rho(\mathbf{r}_1, t) + \nabla_1 \cdot [\rho(\mathbf{r}_1, t) \nabla_1 V_{\text{ext}}(\mathbf{r}_1, t)] \\ & + \nabla_1 \cdot \int d\mathbf{r}_2 \rho^{(2)}(\mathbf{r}_1, \mathbf{r}_2, t) \nabla_1 v_2(\mathbf{r}_1, \mathbf{r}_2) \\ & + \nabla_1 \cdot \int d\mathbf{r}_2 \int d\mathbf{r}_3 \rho^{(3)}(\mathbf{r}_1, \mathbf{r}_2, \mathbf{r}_3, t) \nabla_1 v_3(\mathbf{r}_1, \mathbf{r}_2, \mathbf{r}_3) \\ & + \text{higher terms}. \end{aligned} \quad (53)$$

Since we have used no approximations, equation (53) is *exact* so far. However, at the same time this equation is not useful since the distribution function $\rho^{(1)}$ is expressed

in terms of other (unknown) functions $\rho^{(n)}$ (with $n \geq 1$). This hierarchy problem³ [92] (also known as “Yvon-Born-Green hierarchy”) can be resolved by applying an (approximate) closure relation. Marconi and Tarazona [97; 98] proposed to employ an exact *equilibrium* sum rule for the direct correlation function which reads in the case of purely pairwise additive interaction potentials

$$-k_B T \rho(\mathbf{r}) \nabla c^{(1)}(\mathbf{r}) = \int d\mathbf{r}' \rho^{(2)}(\mathbf{r}, \mathbf{r}') \nabla v_2(\mathbf{r}, \mathbf{r}'), \quad (54)$$

as a “local equilibrium approximation” also for systems driven out of equilibrium. In other words, by setting the non-equilibrium two-body density distribution function at time t equal to those of an equilibrium system with the same one-body density profile leads to the dynamical density functional theory (DDFT) equation of motion, that is,

$$\gamma \frac{\partial \rho(\mathbf{r}, t)}{\partial t} = \nabla \cdot \left[\rho(\mathbf{r}, t) \nabla \frac{\delta \mathcal{F}[\rho(\mathbf{r}, t)]}{\delta \rho(\mathbf{r}, t)} \right], \quad (55)$$

where we have replaced $c^{(1)}$ using equation (32). We note that equation (55) is a generalized continuity equation for the one-body density distribution which links the macroscopic behavior of the system to the microscopic Hamiltonian.

2.3. Spatiotemporal correlations

Pair correlation functions play a fundamental role for the description of the structure inside a fluid. The central quantity for spatiotemporal correlations in *non-equilibrium* is the van Hove function $G(\mathbf{r}, t)$. In this section we derive the latter function by employing Percus’ test particle limit within the framework of DDFT.

2.3.1. Pair correlation function of the bulk system

The spatial correlations for a fluid in *equilibrium* between two arbitrary positions \mathbf{r} and \mathbf{r}' are closely related to the two-body density distribution $\rho^{(2)}(\mathbf{r}, \mathbf{r}')$ defined in

³The fact that this hierarchy problem exists for every member $\rho^{(n)}$ can be seen by deriving analogously a Fokker-Planck equation for $\rho^{(n)}$

equation (47), that is,

$$g(\mathbf{r}, \mathbf{r}') = \frac{\rho^{(2)}(\mathbf{r}, \mathbf{r}')}{\rho(\mathbf{r})\rho(\mathbf{r}')}. \quad (56)$$

In the absence of correlations, the pair correlation function is given by $g(\mathbf{r}, \mathbf{r}') \equiv 1$ such that the function $\rho^{(2)}(\mathbf{r}, \mathbf{r}')$ is equal to the product of two one-body densities evaluated at the respective positions⁴. In fact, the same is true for all fluids in the limit $|\mathbf{r} - \mathbf{r}'| \rightarrow \infty$, that is,

$$\lim_{|\mathbf{r}-\mathbf{r}'| \rightarrow \infty} \rho^{(2)}(\mathbf{r}, \mathbf{r}') = \rho(\mathbf{r})\rho(\mathbf{r}'). \quad (57)$$

In the case of an homogeneous system, the pair correlation function depends only on the relative distance between two particles such that equation (56) can be written as

$$g(|\mathbf{r} - \mathbf{r}'|)(\rho^{\text{bulk}})^2 = \rho^{(2)}(|\mathbf{r} - \mathbf{r}'|). \quad (58)$$

From a reference point, the average number of particles located within the range $[r; r + dr]$ is given by $4\pi r^2 \rho g(r)$.

2.3.2. Percus' test particle limit

Percus central idea was to consider local density perturbations $\Delta\rho(r) = \rho(r) - \rho^{\text{bulk}}$ which are generated by inserting a test particle into the bulk system. Assuming that $\Delta\rho(r)$ is a small quantity, we can approximate the excess free energy by using a Taylor series expansion of the excess free energy in $\Delta\rho(r)$, that is,

$$\begin{aligned} \mathcal{F}^{\text{ex}}[\rho] &= \mathcal{F}^{\text{ex}}[\rho^{\text{bulk}}] + \int d\mathbf{r} \left. \frac{\delta \mathcal{F}^{\text{ex}}[\rho]}{\delta \rho(r)} \right|_{\rho^{\text{bulk}}} \Delta\rho(r) \\ &+ \frac{1}{2} \int d\mathbf{r} \int d\mathbf{r}' \left. \frac{\delta^2 \mathcal{F}^{\text{ex}}[\rho]}{\delta \rho(r) \delta \rho(r')} \right|_{\rho^{\text{bulk}}} \Delta\rho(r) \Delta\rho(r') \\ &+ \mathcal{O}(\Delta\rho(r)^3). \end{aligned} \quad (59)$$

⁴Note that assuming $g(\mathbf{r}, \mathbf{r}') \equiv 1$ for all distances is equal to setting $\mathcal{F}^{\text{corr}}[\rho(\mathbf{r})] \equiv 0$ in equation (36)

The functional derivatives evaluated at $\rho(r) = \rho^{\text{bulk}}$ are related to the correlation functions $c^{(1)}$ and $c^{(2)}$, that is, [92]

$$\begin{aligned} \left. \frac{\delta \mathcal{F}^{\text{ex}}[\rho]}{\delta \rho(r)} \right|_{\rho^{\text{bulk}}} &= \mu^{\text{ex}}(r; \rho^{\text{bulk}}) = \beta^{-1} c^{(1)}(r), \\ \left. \frac{\delta^2 \mathcal{F}^{\text{ex}}[\rho]}{\delta \rho(r) \delta \rho(r')} \right|_{\rho^{\text{bulk}}} &= -\beta^{-1} c^{(2)}(r, r'; \rho^{\text{bulk}}) = -\beta^{-1} c^{(2)}(|r - r'|; \rho^{\text{bulk}}). \end{aligned} \quad (60)$$

Minimizing then the Helmholtz free energy (31) together with equation (59) yields the Euler-Lagrange equations for the chemical potential, that is,

$$\mu = \mu^{\text{id}}(\rho_0^{\text{bulk}}) + \mu^{\text{ex}}(\rho_0^{\text{bulk}}), \quad (61)$$

where $\mu^{\text{id}}(\rho_0^{\text{bulk}})$ is the ideal gas contribution evaluated at the equilibrium density $\rho(r) = \rho_0^{\text{bulk}}$.

We now carry out the test particle limit by inserting a test particle into the system and keeping its position coordinate fixed at $r' = r_0$. All other particles interact with the test particle via the pair potential $\phi(r) \equiv v(|r - r_0|)$. Solving equation (61) for the inhomogeneous density yields

$$\rho(r)/\rho^{\text{bulk}} = \exp \left(-\beta \phi(r) + \int d\mathbf{r}' c^{(1)}(|r - r'|) \Delta \rho(r') + B(r) \right), \quad (62)$$

where $B(r) = \delta \mathcal{O}(\Delta \rho(r)^3)/\delta \rho(r)$ is an unknown function [82] which contains the higher order terms of the Taylor expansion (59). The direct correlation function $c^{(1)}(r)$ is related to the total correlation function $h(r)$ through the Ornstein-Zernike equation, that is,

$$h(r) = c^{(1)}(r) + \rho^{\text{bulk}} \int d\mathbf{r}' h(r') c^{(1)}(|r - r'|). \quad (63)$$

The general solution of the integral equation (63) can be derived using diagrammatic methods which leads to the result [92]

$$h(r) = c^{(1)}(r) + \ln(g(r)) + \beta v(r) + b(r), \quad (64)$$

where $v(r)$ is the pair potential and $b(r)$ is the bridge function. Substituting equa-

tion (64) into equation (63) yields

$$g(r) = \exp \left(-\beta v(r) + \int d\mathbf{r}' c^{(1)}(|r - r'|) \rho^{\text{bulk}} h(r') + b(r) \right). \quad (65)$$

By comparing equations (65) and (62) we find the identities

$$\begin{aligned} g(r) &= \rho(r) / \rho^{\text{bulk}}, \\ h(r) &= \Delta \rho(r) / \rho^{\text{bulk}}, \end{aligned} \quad (66)$$

where $b(r) = B(r)$ and $v(r) = \phi(r)$. We thus find that the radial distribution function $g(r)$ is related to the equilibrium one-body density in the presence of a test particle interacting through the pair potential $v(r)$.

2.3.3. The van Hove function

The probability of finding a particle at position \mathbf{r} , given that one particle was at the origin at time $t = 0$, is given by the van Hove functions $G(\mathbf{r}, t)$ which can be decomposed into a “self part” and a “distinct part” [92; 82], that is,

$$G(\mathbf{r}, t) = G^s(\mathbf{r}, t) + G^d(\mathbf{r}, t), \quad (67)$$

where

$$\begin{aligned} G^s(\mathbf{r}, t) &= \frac{1}{N} \left\langle \sum_{i=1}^N \delta(\mathbf{r} - \mathbf{r}_i(t) + \mathbf{r}_i(0)) \right\rangle, \\ G^d(\mathbf{r}, t) &= \frac{1}{N} \left\langle \sum_{i=1}^N \sum_{j \neq i} \delta(\mathbf{r} - \mathbf{r}_i(t) + \mathbf{r}_j(0)) \right\rangle. \end{aligned} \quad (68)$$

At time $t = 0$ these functions fulfill the initial conditions

$$\begin{aligned}
 G^s(\mathbf{r}, t = 0) &= \delta(\mathbf{r}), \\
 G^d(\mathbf{r}, t = 0) &= \frac{1}{N} \left\langle \sum_{i=1}^N \sum_{j \neq i}^N \delta(\mathbf{r} - \mathbf{r}_i + \mathbf{r}_j) \right\rangle \\
 &= \frac{1}{N} \left\langle \sum_{i=1}^N \sum_{j \neq i}^N \int d\mathbf{r}' \delta(\mathbf{r}' + \mathbf{r} - \mathbf{r}_i) \delta(\mathbf{r}' - \mathbf{r}_j) \right\rangle \\
 &= \frac{1}{N} \int d\mathbf{r}' \rho^{(2)}(\mathbf{r}' + \mathbf{r}, \mathbf{r}').
 \end{aligned} \tag{69}$$

In the last step we have used the definition of the two-body density distribution given in equation (47). For the homogeneous system, the function $\rho^{(2)}(\mathbf{r}' + \mathbf{r}, \mathbf{r}')$ depends only on relative distances $|\mathbf{r} - \mathbf{r}'|$. In this case, the integral in equation (70) can be carried out such that the distinct part reads

$$G^d(r, t = 0) = \frac{1}{N} \int d\mathbf{r}' \rho^{(2)}(|\mathbf{r} - \mathbf{r}'|) = \frac{(\rho^{\text{bulk}})^2}{N} \int d\mathbf{r}' g(|\mathbf{r} - \mathbf{r}'|) = \rho^{\text{bulk}} g(r). \tag{71}$$

From equation (71) it follows that the equilibrium structure of an homogeneous fluid is closely linked to the distinct part of $G(r, t)$ at time $t = 0$.

For times $t > 0$, one can apply an ‘‘identification scheme’’ as suggested by references [83; 82] in order to obtain the van Hove functions from conditional one-body profiles. In the case of inhomogeneous systems the identification is

$$\begin{aligned}
 G_s(\mathbf{r}, t) &\equiv \rho_s(\mathbf{r}, t), \\
 G_d(\mathbf{r}, t) &\equiv \rho_d(\mathbf{r}, t).
 \end{aligned} \tag{72}$$

In other words, one identifies the self part and the distinct part of van Hove’s function with conditional one-body profiles of a *binary* mixture where one particle is treated separately from the rest. Thus, within this scheme one has to calculate the dynamics of the conditional profiles ρ_α which can be done by employing the DDFT equations of a mixture.

2.4. Pyragas control loop

Control theory is an important discipline originating from the field of nonlinear dynamics. A central aspect in this context is the development of control schemes with the goal of manipulating the dynamical behavior of a system. Successful examples include the stabilization of unstable steady states such as periodic oscillations or the suppression of chaos [99; 68]. A control scheme can be applied within control theory to any dynamical system where the equation of motion can be written in the general form

$$\dot{x} = f(x(t), F(t)), \quad (73)$$

where $x(t)$ represents a time-dependent system state and $F(t)$ is a control force. A special form of control is the “closed-loop” scheme where the control force F depends on the internal dynamics variables $x(t)$ compared to “open-loop” schemes which are purely based on adjusting external parameters. We focus, in particular, on the “time-delayed feedback” of closed-loop type which was proposed by Pyragas in 1992 [67], that is,

$$\tilde{F}_{\text{pyr}}(t, \tau) = K_0[g(x(t)) - g(x(t - \tau))], \quad (74)$$

where K_0 is the control amplitude, $f(t) \equiv g(x(t))$ is some (arbitrary) time-dependent signal depending on the system state, and τ is the delay. As can be seen from equation (74) the Pyragas loop is noninvasive, that is, the control force vanishes once the target state is reached. This is in contrast to most open-loop schemes where the stability of the states from the uncontrolled system is typically affected by the external parameters.

In the context of colloidal systems, we propose a slight adjustment where we replace $g(x(t))$ by a space-averaged coupling function $\bar{f}(t)$, that is,

$$F_{\text{pyr}}(t, \tau) = K_0[\bar{f}(t) - \bar{f}(t - \tau)], \quad (75)$$

In equation (75) the “control target” $\bar{f}(t)$ may be any function that is measurable in an experiment, e.g., the centre of mass of the system. Indeed, colloidal particles are typically so large that their position (and, consequently, the first moment of the density distribution) can be easily monitored by real-space methods such as video microscopy.

A block diagram of the time-delayed feedback control (75) is depicted in figure 4. The difference of the control target at time t and its value at time $t - \tau$ is being used as an

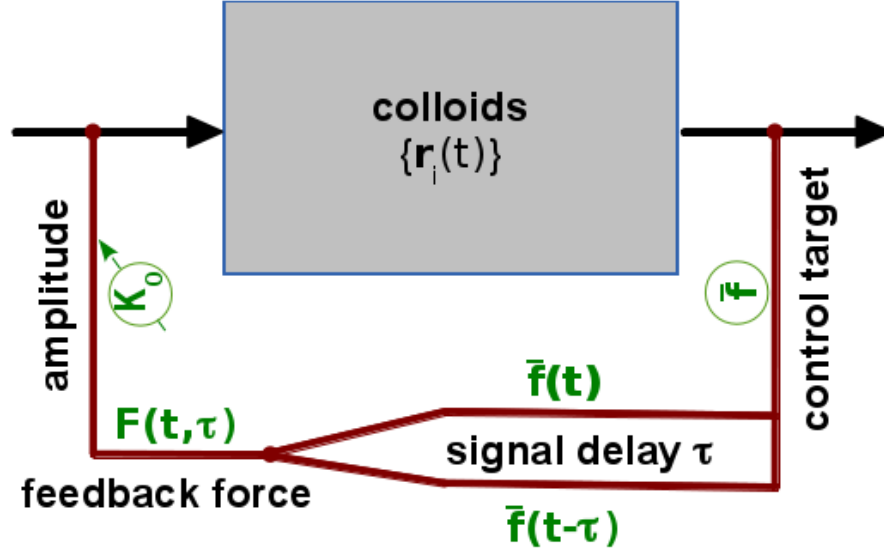


Figure 4.: A block diagram for the delayed feedback control of Pyragas type where the control target \bar{f} is a function of the particle coordinates \mathbf{r}_i . Due to a systematic time delay τ in the signal \bar{f} the control is lagging behind and cannot change the system state instantaneously. The amplitude K_0 of the feedback force is in this example adjustable through some external parameter.

input for the feedback loop and K_0 is an adjustable control parameter, e.g., through tuning external field parameters.

In fact, delayed feedback control can be found in a variety of experimental realizations including optical systems [100; 68], mechanical pendulum systems [101], and electrical systems [102]. An interesting aspect is that these schemes can be applied to situations where a detailed quantitative knowledge of the underlying system dynamics is lacking. This makes the field of control theory rather widely applicable, also in diversified areas such as biomedicine (e.g., see reference [103] for the control of cardiac arrhythmia). Beyond this more applicational motivations, feedback-controlled phenomena are also of fundamental interest due to the subtle interplay between state-dependent control protocols, thermodynamics and information theory [104; 105].

In the next chapter we make some first steps towards colloidal systems under feedback control where we address important questions concerning the roles of the control target

and the prefactor K_0 .

We close the theory part by showing how feedback forces can be implemented in the framework of DDFT. The current in the DDFT equation (55) is given by

$$\mathbf{J}(\mathbf{r}, t, \tau) = -\gamma^{-1} \rho(\mathbf{r}, t) \mathbf{F}(t, \tau), \quad (76)$$

where the drift-diffusion “force” \mathbf{F} arises from the chemical potential, that is,

$$\mathbf{F}(\mathbf{r}, t, \tau) = \nabla \mu(\mathbf{r}, t) = \nabla \frac{\delta \mathcal{F}[\rho(\mathbf{r}, t)]}{\delta \rho(\mathbf{r}, t)}. \quad (77)$$

To the contributions from the ideal gas and the excess part accounting for interactions, we add a third force stemming from the feedback loop, that is,

$$\mathbf{F}(\mathbf{r}, t, \tau) = \mathbf{F}^{\text{id}}(\mathbf{r}, t) + \mathbf{F}^{\text{ex}}(\mathbf{r}, t) + \mathbf{F}^{\text{fb}}(\mathbf{r}, t, \tau), \quad (78)$$

where

$$\mathbf{F}^{\text{fb}}(\mathbf{r}, t, \tau) \equiv \nabla \mu^{\text{fb}}(\mathbf{r}, t, \tau) = \nabla \frac{\delta \mathcal{F}^{\text{fb}}(\mathbf{r}, t, \tau)}{\delta \rho(\mathbf{r}, t)}. \quad (79)$$

By postulating that the function \mathcal{F}^{fb} exists, the feedback force \mathbf{F}^{fb} can be directly inserted into the DDFT equation (55).

3. The one-dimensional driven system

One-dimensional Brownian systems under biasing forces are interesting models for investigating transport phenomena in non-equilibrium. A large number of studies have been devoted to this topic resulting in fascinating discoveries such as anomalous diffusion with giant diffusion [106; 57; 52; 53] and single file diffusion [65] being the most prominent examples. However, most studies focus on non-interacting or single particle systems neglecting collective effects which are ubiquitous in colloidal systems. Indeed, a recent study showed for the latter that attractions can lead to novel transportation modes where the particles move as “particle trains” along modulated channels [107; 108].

In this chapter we investigate the dynamics of non-interacting and also purely repulsive colloids in tilted washboard potentials. We consider infinitely extended (“circular ring”) and finite microchannel geometries. Our primary aim is to manipulate the transport behavior with (closed-loop) time-delayed feedback schemes. Feedback control in the context of Brownian systems is a focus of growing interest, and the method has already been applied, on a theoretical level, to Brownian motors [109; 110; 110] and flashing or rocking ratchets [71]. Moreover, a first experimental realization of a feedback-controlled flashing ratchet already exists [111].

3.1. Model

Our model system consists of N colloidal particles in a one-dimensional channel of length L . The particles are subject to a spatially periodic, symmetric “washboard” potential $U_{\text{wb}}(z) = U_0 \cos^2(kz)$, where k defines the wavelength and U_0 is the amplitude. In the following we set $k\sigma = 1$ where σ corresponds to the effective radius of the particle. For a colloidal particle with spherical symmetry, σ is just the radius of the sphere while for a polymer, σ is the radius of gyration. The washboard potential is tilted by a constant force $\mathbf{F}_{\text{bias}} = F_0 \hat{\mathbf{z}}$ (with $\hat{\mathbf{z}}$ being the unit vector in z -direction) corresponding to a linear potential $U_{\text{bias}} = -F_0 z$. The tilting leads to an effective motion of the particles in the direction of $\text{sign}(F_0)$ along the z -axis. In addition to

these static potentials, we assume that the particles are subject to a time-delayed feedback control force of form

$$F_{\text{fb}}(t, \tau) = -K_0(1 - \tanh [\bar{f}(t) - \bar{f}(t - \tau)]). \quad (80)$$

For the space-averaged coupling function $\bar{f}(t)$ we set

$$\bar{f}(t) = \int_{z_0}^{z_0+L} f(z)\rho(z, t) dz, \quad (81)$$

with z_0 being the coordinate of the origin of the z -axis. Note that when the feedback term is switched on, the effective constant driving force is given by $\tilde{\gamma} = F_0 - K_0$. In the following, we choose a positive value for F_0 such that the particles move preferentially to the right when the control force is being switched off. We stress that the ansatz for the feedback force in equation (80) is clearly of heuristic nature, and thus cannot be derived from any physical potential.

Collecting all external contributions gives the total external potential

$$\begin{aligned} U_{\text{ext}} &= U_{\text{wb}}(z) + U_{\text{fb}}(t, \tau) + U_{\text{bias}}(z) \\ &= U_0 \cos^2(z) + K_0 z(1 - \tanh [\bar{f}(t) - \bar{f}(t - \tau)]) - F_0 z, \end{aligned} \quad (82)$$

where we assumed that the contribution of the feedback force is linear in the position coordinate z . In the absence of interactions between the particles, the DDFE equation (55) reduces to

$$\gamma \frac{\partial \rho(z, t)}{\partial t} = k_B T \frac{\partial^2 \rho(z, t)}{\partial z^2} - \frac{\partial}{\partial z} [\rho(z, t) \tilde{\mu}(z, t; \tau)], \quad (83)$$

where the drift coefficient $\tilde{\mu}$ can be calculated from the external potential U_{ext} via $\tilde{\mu} = -U'_{\text{ext}}$ where $'$ denotes the derivative with respect to z . The mobility coefficient in equation (83) is related to the diffusion constant via $\gamma^{-1} = \beta D_0$ [where $\beta = 1/(k_B T)$] and we set its value to $\gamma^{-1} \tau_B k_B T / \sigma^2 = 1$.

3.2. Delay-induced instability

In the absence of control ($K_0 = 0$), the driven system ($F_0 > 0$) settles into a stationary, non-oscillatory state. The corresponding distribution $\rho_s(z)$ can be found analytically

[50]

$$\begin{aligned}\rho_s(z) &= e^{-U_{\text{ext}}(z)/k_B T} \int_z^{L+z} dy e^{U_{\text{ext}}(y)/k_B T} / \mathcal{N}, \\ \mathcal{N} &:= \int_{z_0}^{L+z_0} dz \int_z^{L+z} dy e^{U_{\text{ext}}(y)-U_{\text{ext}}(z)/k_B T},\end{aligned}\quad (84)$$

where U_{ext} is the external potential given in equation (82) but with $K_0 = 0$ (or, equivalently, $\bar{f}(t) - \bar{f}(t - \tau) = 0$ since we assumed stationarity).

In the presence of control, the behavior of the system depends on the interplay of the parameters of the control term, on the one hand, and the tilted washboard potential, on the other hand. For certain parameter combinations we still find a stationary state, in which the difference $\bar{f}(t) - \bar{f}(t - \tau)$ disappears. However, as we will demonstrate, for suitable parameters the stationary distribution may become unstable, leading to a stable time-periodic distribution $\rho(z, t)$. To interpret this instability, it is useful to reconsider equations (80-81) from a somewhat different perspective. In particular, since the control target $\bar{f}(t)$ involves a spatial integral over the entire distribution $\rho(z, t)$, we have effectively introduced a coupling between the colloidal particles. Moreover, this coupling is of infinite range (within the periodic system considered). Thus, the time-delayed feedback control introduces an effective interaction of mean-field type, and it is this interaction, which may lead to new stationary states as well as new dynamic regimes, associated with time-periodic density oscillations.

3.2.1. Linear stability analysis

We start by applying a linear stability analysis in order to investigate the impact of the delayed feedback control. To this end, we rewrite the dimensionless Fokker-Planck equation in terms of the effective potential $U_{\text{eff}} = U_0 \cos^2 z + (K_0 - F_0)z$ as follows

$$\begin{aligned}\frac{\partial \rho(z, t)}{\partial t} &= \frac{\partial^2 \rho(z, t)}{\partial z^2} + \frac{\partial}{\partial z} \left[\rho(z, t) \frac{\partial U_{\text{eff}}}{\partial z} \right] \\ &\quad - K_0 \tanh [\bar{f}(t) - \bar{f}(t - \tau)] \frac{\partial \rho(z, t)}{\partial z}.\end{aligned}\quad (85)$$

The non-trivial stationary state $\rho_s(z)$ satisfies

$$0 = \frac{\partial}{\partial z} \left(\rho_s \frac{\partial U_{\text{eff}}}{\partial z} + \frac{\partial \rho_s(z)}{\partial z} \right), \quad (86)$$

which can be written as an eigenvalue problem

$$\hat{L}\rho_s = \lambda\rho_s, \quad (87)$$

with the stationary Fokker-Planck operator $\hat{L} = \partial_z^2 + (\partial_z U_{\text{eff}})\partial_z + \partial_z^2 U_{\text{eff}}$ and zero eigenvalue $\lambda = 0$. We are interested in the onset of an oscillatory instability of ρ_s . Following the approach, developed earlier [112; 113], we set

$$\rho(z, t) = \rho_s(z) + \epsilon (C(z) \cos \omega t + S(z) \sin \omega t), \quad (88)$$

where ϵ is the (small) amplitude of the perturbation, ω is the unknown onset frequency and the unknown functions $C(z)$ and $S(z)$ determine the shape of the perturbation. With this ansatz, the equation (85) can be linearized in ϵ to yield

$$\begin{aligned} -\omega C \sin \omega t + \omega S \cos \omega t = & C'' \cos \omega t + S'' \sin \omega t \\ & + \partial_z [U'_{\text{eff}}(C \cos \omega t + S \sin \omega t)] \\ & - K_0 \rho'_s [\bar{f}(t) - \bar{f}(t - \tau)], \end{aligned} \quad (89)$$

where \prime stands for the derivative with respect to z and the perturbed mean field is given by

$$\bar{f}(t) = \langle C \rangle \cos \omega t + \langle S \rangle \sin \omega t, \quad (90)$$

with $\langle C \rangle = \int_{z_0}^{L+z_0} f(z)C(z) dz$ and $\langle S \rangle = \int_{z_0}^{L+z_0} f(z)S(z) dz$. The initial moment of time can always be chosen in such a way that, for instance, $\bar{f}(t) = \cos \omega t$. This implies two additional integral conditions on the functions $C(z)$ and $S(z)$

$$\int_{z_0}^{L+z_0} f(z)C(z) dz = 1, \quad \int_{z_0}^{L+z_0} f(z)S(z) dz = 0. \quad (91)$$

Then the difference $\bar{f}(t) - \bar{f}(t - \tau)$ becomes

$$\bar{f}(t) - \bar{f}(t - \tau) = \cos \omega t(1 - \cos \omega \tau) - \sin \omega t \sin \omega \tau. \quad (92)$$

Finally, calculating the coefficients of $\sin \omega t$ and $\cos \omega t$ in equation (89), we obtain two coupled equations for the unknown functions $C(z)$ and $S(z)$

$$\begin{aligned} S'' = & -\omega C - \partial_z [U_{\text{eff}}S] - K_0 \sin \omega \tau \rho'_s \\ C'' = & \omega S - \partial_z [U_{\text{eff}}C] + K_0(1 - \cos \omega \tau) \rho'_s. \end{aligned} \quad (93)$$

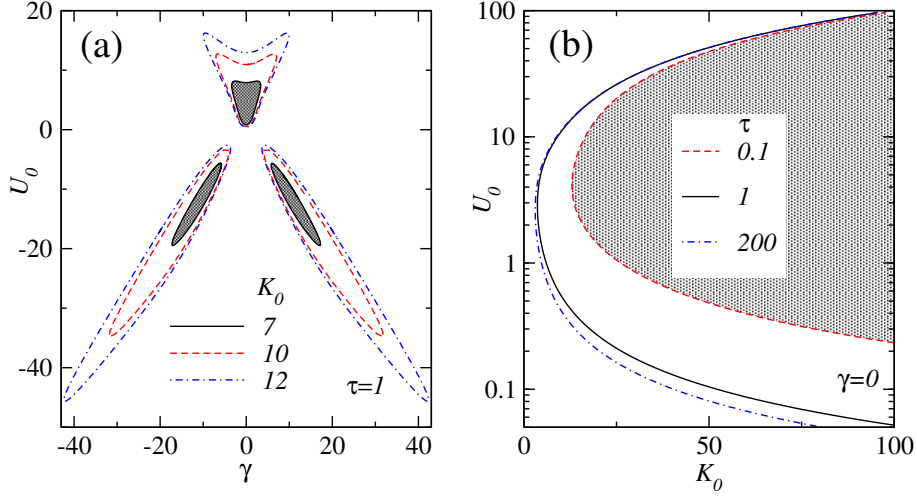


Figure 5.: (a) Stability threshold in the plane $(\tilde{\gamma}, U_0)$, obtained for $\tau = 1$ and different values of K_0 , as given in the legend. The stationary state is unstable in the area enclosed by the respective curves (shaded area for $K_0 = 7$). (b) Stability threshold in the plane (K_0, U_0) for zero drive $\tilde{\gamma} = 0$ and different delay times as in the legend. The instability region always lies to the right from the respective curve (shaded area for $\tau = 0.1$). The calculations for the results shown in (a) and (b) were carried out by A. Pototsky.

In order to find the stability threshold, one needs to solve equations (93) simultaneously with equation (87). To this end we proceed as follows. We rewrite equations (87,93) as an autonomous dynamical system of seven first order equations, including the equation for z , which takes the form $z' = 1$. The total number of the system parameters is thereby extended by two additional parameters, namely by the onset frequency ω and the (zero) eigenvalue λ . The above dynamical system of seven equations is supplemented with three integral conditions on the functions $\rho_s(z)$, $C(z)$ and $S(z)$. These are given by equations (91) and by the normalization condition on ρ_s

$$\int_{z_0}^{L+z_0} \rho_s(z) dz = N, \quad (94)$$

where N is the normalization parameter. The boundary conditions for all involved functions are taken to be periodic in the interval $z \in [z_0, z_0 + L]$. This boundary value problem (BVP) of seven equations and three integral conditions is then solved using the numerical continuation technique (AUTO). These calculations were carried out by A. Pototsky.

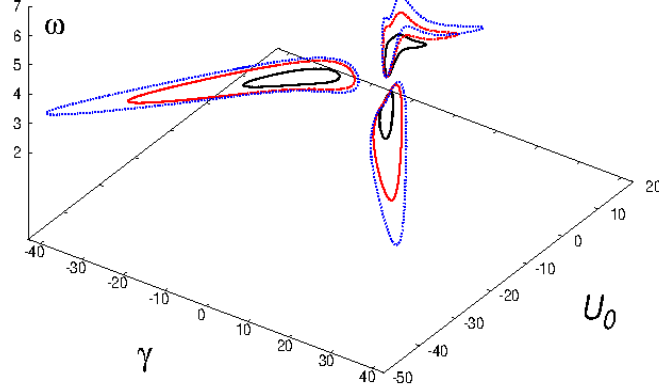


Figure 6.: Three-dimensional view of figure 5(a). The onset frequency ω as a function of U_0 and $\tilde{\gamma}$ for $\tau = 1$ and three different K_0 . The projection onto the $(\tilde{\gamma}, U_0)$ plane recovers figure 5(a). The calculations were carried out by A. Pototsky.

3.2.2. Stability thresholds

Before proceeding, it is important to notice that the linear stability of the stationary distribution ρ_s crucially depends on the choice of the coupling function $f(z)$ [see equation(81)]. Thus, the solution of the BVP equations (93) is invariant under the shift of the coordinate system $z \rightarrow z + \delta$, with arbitrary δ , only if the coupling function $f(z)$ is itself periodic with the period L . Indeed, the integrals $\int_{z_0}^{z_0+L} f(z)C(z) dz$ and $\int_{z_0}^{z_0+L} f(z)S(z) dz$, are shift-invariant if $f(z)$ is L -periodic. On the contrary, if the period of $f(z)$ is different from L , or if $f(z)$ is a non-periodic function, then the stability threshold depends on the particular choice of origin of the z -axis, i.e. it depends on z_0 . We use a linear, non-periodic coupling function $f(z) = z$. We note that this choice is motivated by recent experimental works [see, e.g., references 64; 111]. Indeed, using video microscopy it is possible to monitor the trajectories of individual colloidal particles, and therefore also their center of mass. The center-of-mass position is precisely the quantity one obtains when inserting the relation $f(z) = z$ into equation (81) for the coupling function $\bar{f}(t)$. For further calculations, the origin of the z -axis is chosen in the maximum of the washboard potential $U(z)$, implying that $z_0 = 0$.

First, we fix $\tau = 1$ and compute the stability threshold in the plane of parameters $(\tilde{\gamma}, U_0)$, where $\tilde{\gamma} = F_0 - K_0 = 0$, for three different values of the coupling strength $K_0 = 7, 10, 12$, as shown in figure 5(a). The stationary density, normalized with $N = 1$,

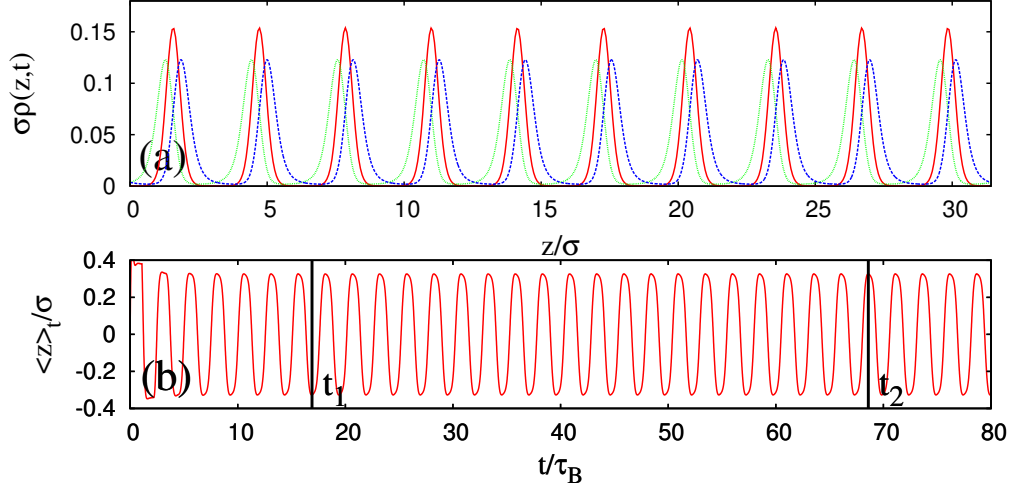


Figure 7.: Results for a controlled system in the periodic regime. (a) Density distribution $\rho(z,t)$ as a function of position for selected times $t_0/\tau_B = 0$ (red curve), $t_1/\tau_B = 16.9$ (dotted green curve) and $t_2/\tau_B = 68.6$ (dashed blue curve). (b) Average particle position $\langle z \rangle_t$ as a function of time. The parameters are $U_0 = 7k_B T$, $F_0 = 7k_B T/\sigma$, $K_0 = 7k_B T/\sigma$, $\tau = \tau_B$ and $L = 10\pi\sigma$.

i.e. $\int_0^\pi \rho_s(z) dz = N = 1$, is unstable in the regions bounded by the corresponding closed curves. Thus, for $K_0 = 7$, the instability occurs in the shaded area. As expected, the area of the instability expands if the coupling strength K_0 is increased.

Interestingly, the stability diagram for the case when the origin of the z -axis is chosen in the minimum of the washboard potential ($z_0 = \pi/2$), can be obtained from figure 5(a) by the transformation $U_0 \rightarrow -U_0$. For any other choice of z_0 , the topology of the stability threshold is much more complex and generally contains four different bounded regions (not shown).

The effect of the time delay is demonstrated in figure 5(b) for the choice $\tilde{\gamma} = 0$. The stationary density is unstable in the area, which always stretches towards larger values of the coupling strength K_0 , as shown by the shaded area for $\tau = 0.1$. Decreasing τ leads to the suppression of the instability, which clearly demonstrates that the instability is induced by the presence of the time delay in the coupling term.

However, it should be emphasized that having only a time-delayed coupling does not suffice to induce the instability. Thus, from figure 5(b) it follows that even if τ and K_0

are rather large, e.g. $\tau = 200$ and $K_0 \approx 100$, the stationary density is linearly stable for a vanishingly weak or an infinitely strong washboard potential U_0 . At fixed K_0 , only a certain combination of τ and U_0 renders the system unstable with respect to an oscillatory perturbation. Consequently, the onset of the synchronized time-periodic state is a the effect of the combined action of the time-delayed coupling and stationary periodic external modulation in the form of the washboard potential.

By following the stability threshold in the parameter space, we additionally obtain the onset frequency ω directly on the threshold. The latter carries an important information about the time scale of the newly born oscillatory states, given by $T = 2\pi/\omega$. The three-dimensional view of figure 5(a), extended by the onset frequency ω , is shown in figure 6. It can be seen that the smallest temporal period $T \sim 1$ corresponds to positive U_0 , whereas the period of the time-periodic states born at negative U_0 is up to three fold larger, i.e. $T \sim 6$.

3.2.3. Nonlinear regime: Numerical study of the one-body distribution

The observation of the linear instability with respect to oscillatory perturbations predicts possible deviations from the stationary state for a given (“overcritical”) parameter set. In order to study the full nonlinear dynamics, however, the full DDFT equation of the system has to be solved. To explore these nonlinear effect we solve equation (83) numerically. Specifically, we employ a standard “Forward-Time Centered-Space” (FTCS) finite difference method [114] and integrate equation (83) starting from an initial distribution $\rho(z, t = 0)$.

As initial density distribution we choose the equilibrium density distribution in a one-dimensional washboard potential with periodic boundary conditions and the external bias, as well as the control, being switched off. This implies

$$\rho(z, t = 0) = \rho_0 \exp \left[-\beta U_0 \cos^2 \left(\frac{z}{\sigma} \right) \right], \quad (95)$$

where ρ_0 ensures the normalization condition $\int_0^L \rho(z, t = 0) dz = N = 1$. We consider a fixed control amplitude $K_0 = 7k_B T/\sigma$ and focus on parameter values near the stability threshold [see figure 1(a)]. Specifically, we consider the “balanced case” $\tilde{\gamma} = F_0 - K_0 = 0$ and washboard amplitude values of $U_0 = 8k_B T$ (linearly stable) and $U_0 = 7k_B T$ (linearly unstable), respectively. Beginning with the latter case, we plot in figure 7(a) snapshots of the density distribution $\rho(z, t)$ for three subsequent times. The

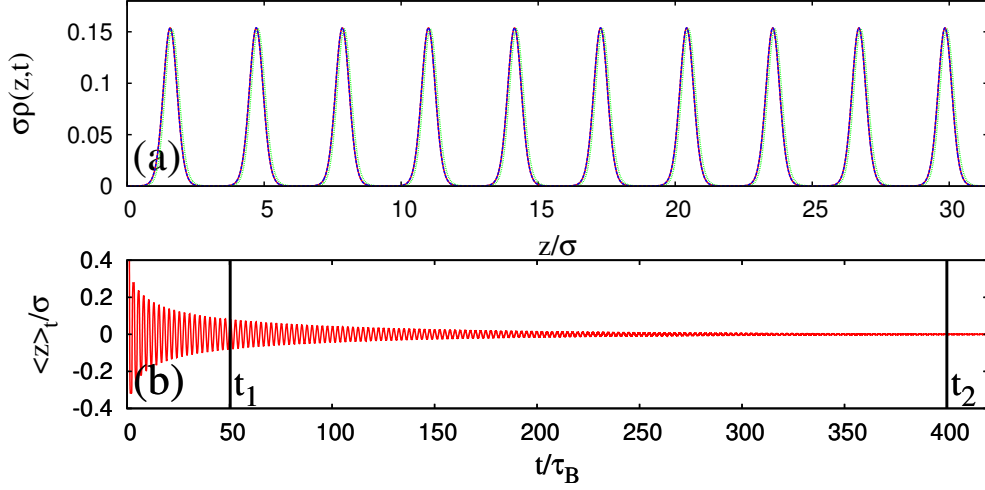


Figure 8.: Results for a controlled system in the regime where the final state is stationary. (a) Density distribution $\rho(z, t)$ as a function of position for selected times $t_0/\tau_B = 0$ (red curve), $t_1/\tau_B = 50.4$ (dotted green curve) and $t_2/\tau_B = 400.0$ (dashed blue curve). (b) Average particle position $\langle z \rangle_t$ as a function of time. The parameters are $U_0 = 8k_B T$, $F_0 = 7k_B T/\sigma$, $K_0 = 7k_B T/\sigma$, $\tau = \tau_B$ and $L = 10\pi\sigma$.

initial distribution $\rho(z, t = 0)$ is periodic in the position coordinate z with a (spatial) period that is equal to the valley-to-valley distance of the washboard potential, that is $\lambda_{\text{wb}} = \pi\sigma$. As expected, the values for the density distribution are increased at the position coordinates $z_i^{\text{valley}} = i\pi\sigma$ (where $i = [0, 1, 2, 3, \dots]$) corresponding to the valley positions of the washboard potential. The specific times t_1, t_2 are chosen such that the appertaining density distributions (shown as the dotted green curve and the dashed blue curve in figure 7(a), respectively) have a maximum displacement from the initial configuration. Inspecting the curves, we find that after a response time of roughly $5\tau_B$, the system settles indeed into a stable time-periodic density state, i.e. $\rho(z, t + T) = \rho(z, t)$, where the distribution oscillates around a washboard minimum position with a maximum displacement of approximately 0.33σ . The appearance of such stable oscillations is consistent with the stability diagram in figure 5(a). We supplement the discussion by plotting in figure 7(b) the particle position averaged over one period of the potential, that is, $\langle z \rangle_t = \int_0^{\lambda_{\text{wb}}} \rho(z, t) dz$. Clearly, $\langle z \rangle_t$ oscillates as a function of time with the same frequency ω as the frequency of the density oscillations. In the following, we therefore use the function $\langle z \rangle_t$ to obtain the cycle time $T = 2\pi/\omega$.

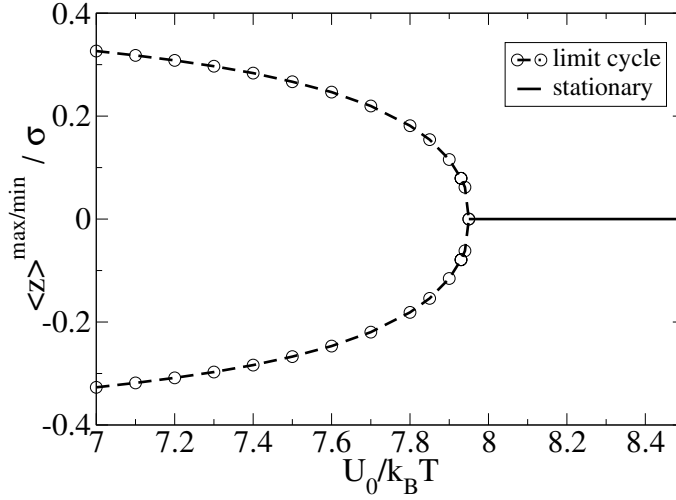


Figure 9.: Local extrema values of the function $\langle z \rangle_t$ as a function of the washboard amplitude U_0 . The parameters are $F_0 = 7k_B T/\sigma$, $K_0 = 7k_B T/\sigma$, $\tau = \tau_B$, $L = 10\pi\sigma$.

We now turn to the case $U_0 = 8k_B T$. For this parameter, the perturbing forces, specifically the constant tilting force \mathbf{F}^{bias} and the feedback force $\mathbf{F}^{\text{f.b.}}$, do not lead to an oscillating state. This is illustrated in figure 8. It is seen that the oscillations at early times are being damped resulting in a stationary, non-periodic density for times $t \gtrsim 400\tau_B$. In figure 8(a) we show the results for the stationary density profile as a dashed blue curve, as well as for two additional profiles, where the red and dotted green curves represent the initial and one intermediate state, respectively. As can be seen from figure 8(b), the average particle position $\langle z \rangle_t$, converges to a constant value $\langle z \rangle_{\text{stat}}/\sigma \approx 0$. In other words, the density displacement related to the equilibrium position at each potential valley vanishes and, thus, the profiles for times $t_2/\tau_B = 400$ and $t_0/\tau_B = 0$ coincide.

We note that for both values of U_0 considered (cf. figures 7-8), the dynamics at early times is transient. In the oscillatory case, the transient regime lasts for about $t_{\text{res}} \approx 5\tau_B$. For the linear stable case, the transient response time can be much larger. For example, for the parameter values that we considered in figure 8 the stationary state is not reached for times less than $t_{\text{res}} \approx 400\tau_B$.

We have repeated the numerical calculations described above for a range of parameters U_0 and the choice $\tilde{\gamma} = F_0 - K_0 = 0$. In this way we can construct a bifurcation diagram characterizing the nature of the instability. As a measure of the instability, we use the oscillation amplitude of $\langle z \rangle_t$. Specifically, we obtain local extrema values

$\langle z \rangle^{\max/\min}$ from the function $\langle z \rangle_t$ and average these over several periods. The results are summarized in figure 9. At large values of U_0 we only find one stable attracting fixed point $\langle z \rangle^{\max/\min} = 0$. However, by decreasing the washboard amplitude U_0 the stationary state (characterized by $\langle z \rangle^{\max/\min} = 0$ for all times t greater than the transient time) loses stability and stable limit cycle oscillations occur (see, e.g., figure 7). This happens in an essentially continuous manner, as figure 9 reveals. We thus conclude that, upon decreasing U_0 below $U_0^c \approx 7.95k_B T$ the system undergoes a supercritical Hopf bifurcation. For $U_0 < U_0^c$ all resulting trajectories perform limit cycle oscillations about the former stationary state $\langle z \rangle^{\max/\min} = 0$. We note that all neighboring trajectories approach the limit cycle. Thus, for $U_0 < U_0^c$, the limit cycle is stable and the only attractor in the system. Furthermore, due to the spatially left-right symmetry in the potential, the local extrema of $\langle z \rangle_t$ appear in symmetrical pairs at $\pm |\langle z \rangle^{\max}|$.

3.2.4. Cycle time for the oscillating density state

An interesting question is to which extent the density oscillation frequency depends on the different system parameters such as washboard potential amplitude U_0 and time delay τ . In figure 6 we have already shown results for the *onset* frequency based on the linear stability analysis. Here we present corresponding data obtained in the nonlinear regime. To this end we define the cycle time T as the overall travel time for a full maximum displacement of the density distribution (towards and back). As argued before, this time can be obtained from the average particle position $\langle z \rangle_t$ by measuring the (time) distance between two maxima [see figure 7(b) for an example].

In figure 10(a) we plot the cycle time T as a function of the delay time τ . Clearly, by increasing the delay time τ the cycle time T increases as well. To understand this behavior it is crucial to recall that the time-delayed feedback force incorporated here is of Pyragas type, i.e. a control target at time t and its value at time $t - \tau$ is used for the feedback signal. In our case the control target is the centre of mass position $\langle z \rangle_t$, which is being shifted as a function of time due to the constant force F^{bias} . Thus, a larger delay time τ implies that the system travels longer distances within the time interval τ . On the other hand, the specific form of the feedback force F^{fb} is constructed such that it always counteracts F^{bias} (see equation (80) and references [72]). Furthermore, the absolute value of F^{fb} is small for large differences $\bar{f}(t) - \bar{f}(t - \tau)$. As a result, the crossover region where the feedback force F^{fb} changes from being essentially inactive to compensating the constant tilting force F^{bias} is accessed more often when the delay time is smaller. Thus, smaller delay times τ yield decreased cycle times T up to the limit where τ is too small to induce time-periodic oscillations in the density any longer

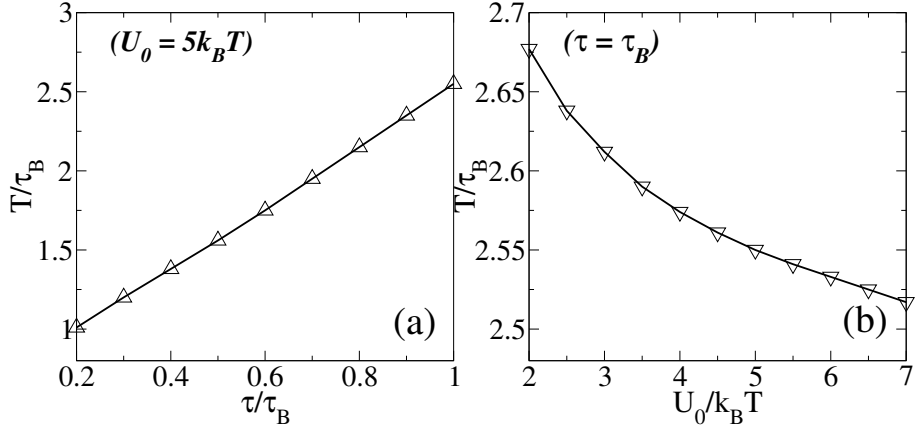


Figure 10.: Density oscillation cycle time T (a) as a function of the delay time τ and (b) as a function of the washboard potential amplitude U_0 within the oscillatory regime [see figure 5]. The parameters are $F_0 = 7k_B T/\sigma$, $K_0 = 7k_B T/\sigma$ and $L = 10\pi\sigma$. The rest of the parameters as in the legend.

[see figure 5(b)].

Figure 10(b) shows the dependence of T on the washboard amplitude U_0 . It is seen that the cycle time T decreases slightly as a function of the washboard amplitude U_0 . It is well known that the energy barrier plays a decisive role for the particle escape rate in a potential minimum for hopping processes that are thermally activated [115]. In our case, the interplay between the washboard potential, the constant tilting force and the control force determines the rate at which particles are crossing to the next potential minimum. By increasing the washboard amplitude U_0 , the energy barrier for a particle escape is increased leading to smaller displacements of the average particle position in a valley. As a result the cycle time of the oscillations is decreased.

3.2.5. Microchannel geometry

So far we have considered infinite systems (i.e. systems with periodic boundaries). In this section we explore to which extent the emergence of an oscillation instability also depends on the channel geometry. To this end, we now consider a system that consists of a microchannel of finite length L with hard walls at the ends. We focus on the nature of the oscillations and the corresponding instability as opposed to the corresponding phenomenon in the system with periodic boundaries. We choose as

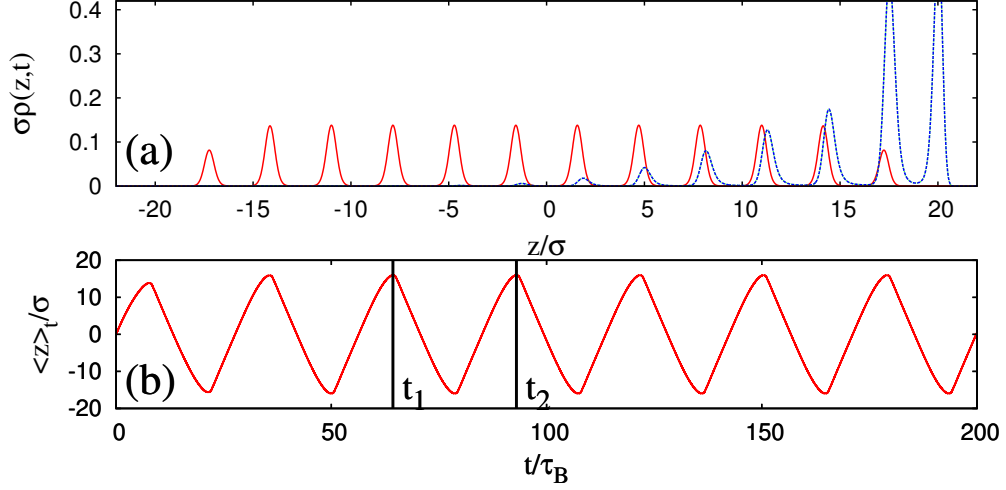


Figure 11.: Results for the microchannel, (a) density distribution $\rho(z, t)$ as a function of position for selected times $t_0/\tau_B = 0$ (red curve), $t_1/\tau_B = 64.3$ (dotted green curve) and $t_2/\tau_B = 93.0$ (dashed blue curve) and (b) shows the first moment of $\rho(z, t)$ as a function of time. The parameters are $U_0 = 8k_B T$, $F_0 = 7k_B T/\sigma$, $K_0 = 7k_B T/\sigma$, $\tau = \tau_B$ and $z_{\text{wall}} = \pm 20\sigma$.

initial distribution the equilibrium density distribution for a single particle subject to the washboard potential plus a wall potential, $\beta U^{\text{wall}} = 10(z/z_{\text{wall}})^{20}$, which confines the particle position to values $|z| \lesssim z_{\text{wall}} = 20\sigma$. Such a smooth wall potential is typically used to model situations where the diameter of the particles forming the wall is much smaller than that of the fluid particles [116]. Thus, the initial distribution is given by

$$\rho(z, t = 0) = \rho_0 \exp \left[-\beta U_0 \cos^2 \left(\frac{z}{\sigma} \right) - 10 \left(\frac{z}{z_{\text{wall}}} \right)^{20} \right]. \quad (96)$$

Again, we focus on the “balanced case” $\tilde{\gamma} = F_0 - K_0 = 0$ with a fixed control amplitude value of $K_0 = 7k_B T/\sigma$. We recall that in the case of the infinite system (periodic boundaries) a washboard amplitude value of $U_0 = 8k_B T$ is already sufficient to suppress oscillatory states, yielding a stationary state for times larger than the transient response time. We choose this specific value for U_0 as a starting point for the microchannel study. In figure 11(a) we show snapshots of the density distribution at

three different times $t_0 = 0\tau_B$, $t_1 = 64.3\tau_B$ and $t_2 = 93.0\tau_B$. We note that the initial density distribution $\rho(z, t = 0)$ (shown as a red curve) is symmetric with respect to the position $z = 0$. After a transient response time of roughly $20\tau_B$ we find stable time-periodic density oscillations where the distribution oscillates between two states characterized by a low and a high average particle position, respectively. Therefore, this state fulfills the periodicity condition $\rho(z, t + T) = \rho(z, t)$ with $T = 2\pi/\omega$ being the cycle time of the oscillations. The snapshots at times t_1 and $t_2 = t_1 + T$ (shown as a dotted green and a dashed blue curve in figure 11(a), respectively), reveal that, indeed, both density profiles appear to be identical, at least to the naked eye. We support this conclusion by plotting in figure 11(b) the average particle position $\langle z \rangle_t = \int_0^L z\rho(z, t)dz$ as a function of time. Here, the function $\langle z \rangle_t$ is averaged over the entire channel length L in contrast to the circular ring geometry (periodic boundaries) where the obtained results are periodic with respect to each valley position. Similar as in section 3.2.3, the function $\langle z \rangle_t$ oscillates as a function of time with the same frequency ω as the frequency of the density oscillations, as can be seen from the time stamps t_1 and $t_2 = t_1 + T$ that we have included as vertical lines. However, we stress that the cycle times here are much longer than for the circular ring geometry. Furthermore, the periodic states have the spatial period equal to the largest spatial period used in the system, which is the system length itself as imposed by the wall potential. As a result, the time-periodic solution oscillates back and forth between $z = \pm z_{\text{wall}}$. We also note that the finding of density oscillations for $U_0 = 8k_B T$, $\tilde{\gamma} = 0$ and $\tau = \tau_B$ is in contrast to what we found in section 3.2.3 where no (periodic) instabilities occur for this specific parameter set.

By further increasing the washboard amplitude to the value of $U_0 = 9k_B T$, on the other hand, we find that the oscillatory behavior at early times is being damped resulting in a stationary, non-periodic density for times $t \gtrsim 20\tau_B$. We conclude that the results of the linear stability analysis (cf. figure 5) can approximately be used as a reference to find states that are linearly unstable for the microchannel system. We argue that this is because the channel is so large ($L = 44\sigma$) that the system is mostly determined by the bulk properties. The instability region for the finite channel seems to be qualitatively similar, but increased in size compared to the results for the circular ring geometry.

In figure 12(a) we show results for the cycle time T as a function of the delay time τ for a fixed value of $K_0 = 7k_B T/\sigma$ and the choice $\tilde{\gamma} = F_0 - K_0 = 0$. Holding the washboard potential amplitude fixed to the value of $U_0 = 5k_B T$, we do not find oscillatory density states below $\tau = 0.3\tau_B$. By increasing τ , we find a qualitatively similar behavior as in the periodic system (see section 3.2.4) for the cycle time T . Specifically, we find a monotonic increase on T as a function of τ . On the other hand, quantitatively

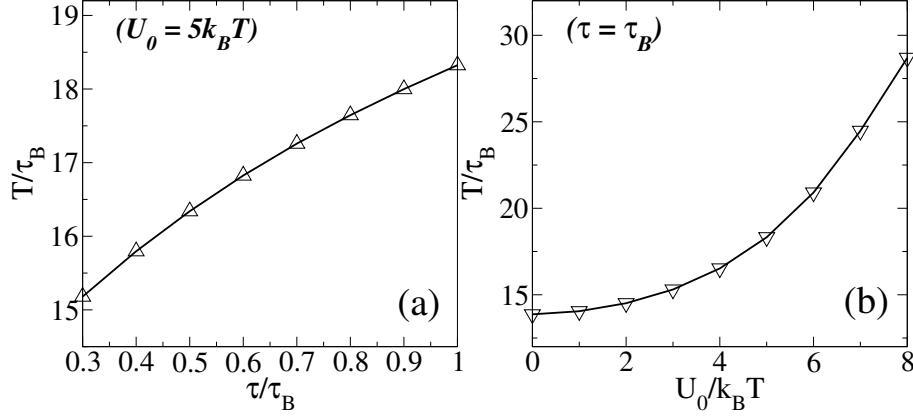


Figure 12.: Density oscillation cycle time T for the microchannel as (a) function of the delay time τ and (b) function of the washboard potential amplitude U_0 . The parameters are $F_0 = 7k_B T/\sigma$, $K_0 = 7k_B T/\sigma$ and $z_{wall} = \pm 20\sigma$. The rest of the parameters as in the legend.

comparing the results for the cycle time T to the periodic system reveals that the values increase by approximately one order of magnitude. This is clearly a consequence of the substantial differences in the oscillations that we observe for the microchannel: the underlying nonlinear terms in the dynamical equations [see equations (82-83)] drive the density propagations over the whole system size, which is given by the channel length L . Thus, it is clear that the cycle time must be significantly longer than in the periodic system, where the oscillations occur around a valley position with displacements that are smaller than $\pi\sigma$ (the spatial period of the washboard potential). We note that for the τ values that we considered (up to $\tau = 10\tau_B$), we do not find any upper boundary for the linear stability threshold. This behavior seems to be similar to the periodic system, where we showed that the oscillatory density state cannot be transformed into a stationary state by increasing the value of τ [cf. figure 5(b)].

In order to investigate the dependence of the cycle time T on the washboard amplitude U_0 , we hold the delay time fixed to the value of $\tau = \tau_B$ and increase (decrease) U_0 in steps of $\Delta U_0 = 1k_B T$ towards the linear stability threshold. We do not find oscillatory density states above $U_0^c \approx 8.63k_B T$. Furthermore, we observe a monotonic increase of T as a function of U_0 , which contrasts with the periodic system where we found monotonic decrease. Again, this is a consequence of the substantially different oscillation mode that we observe for the microchannel.

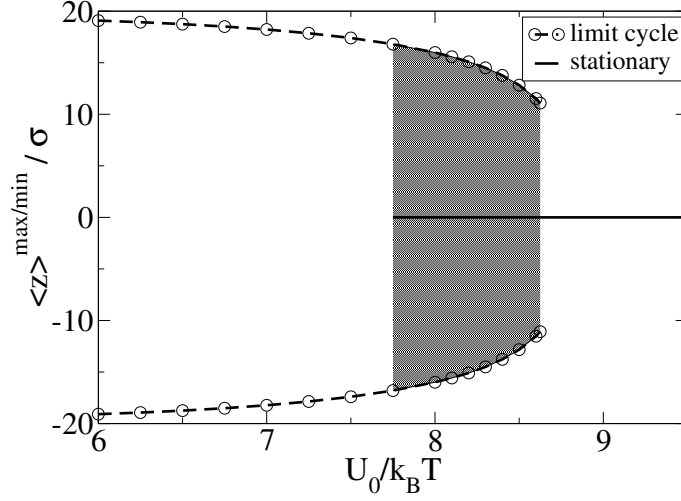


Figure 13.: Local extrema values of the function $\langle z \rangle_t$ as a function of the washboard amplitude U_0 . The shaded area marks the region where the system exhibits hysteresis. The parameters are $F_0 = 7k_B T / \sigma$, $K_0 = 7k_B T / \sigma$, $\tau = \tau_B$, $z_{\text{wall}} = \pm 20\sigma$.

As explained above, any oscillatory perturbation applied to the system travels over the whole system length. Thus, an increased value of U_0 now means that the propagation of the perturbation is hindered, which results in an increased cycle time T that corresponds to the travel time over a distance of approximately twice the system length L (see section 3.2.4).

For completeness, we show in figure 13 the bifurcation diagram for the microchannel calculated in the same fashion as in section 3.2.3. We only find stationary states for washboard amplitudes $U_0 > U_0^c$. Contrary to the infinite system, however, the average particle position $\langle z \rangle_t$ in this stationary state is principally a non-zero constant as $t \rightarrow \infty$. For simplicity, all stationary states in figure 13 have been shifted to zero. Upon increase of U_0 all density oscillations suddenly drop off at $U_0 = U_0^c$ with a jump in the (oscillation) amplitude from the value $|\langle z \rangle^{\text{max}}|$ to zero; i.e., a subcritical Hopf bifurcation occurs. As the parameter U_0 is reversed, a stationary solution can be found below the Hopf bifurcation point for values ranging to $U_0^m \approx 7.75k_B T$. Thus, the system exhibits hysteresis within the parameter region $U_0^m < U_0 < U_0^c$ (shown as the shaded area in figure 13).

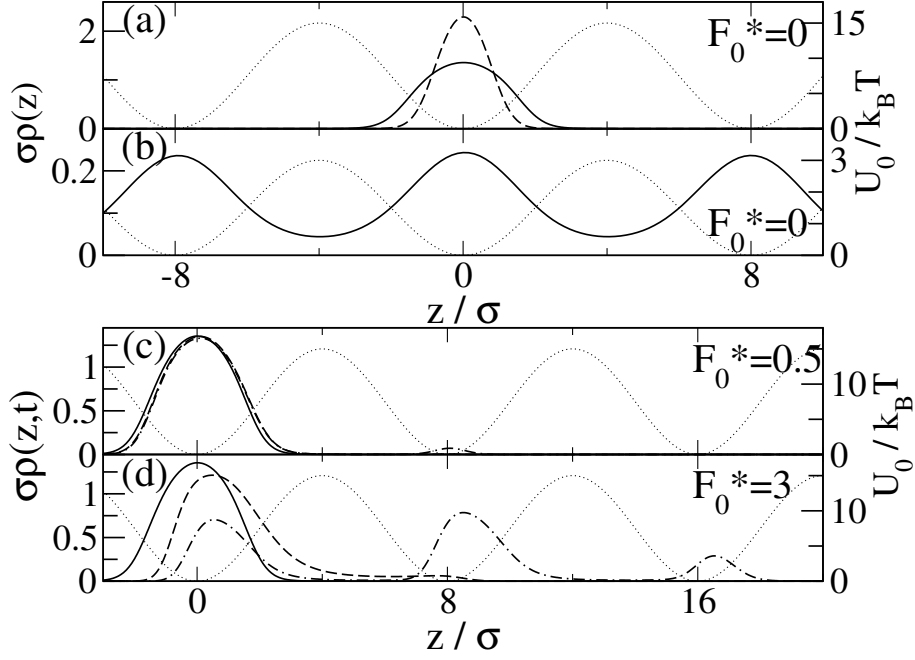


Figure 14.: Density profiles as a function of the particle position at $\varepsilon = 4k_B T$ and $N = 4$. The washboard potential $U^{\text{wb}}(z)$ (with $k = \pi/(8\sigma)$) is indicated by the dotted lines. Top: profiles for non-driven systems ($F_0 = 0$) at (a) $U_0 = 15k_B T$ and (b) $U_0 = 3k_B T$. In (a) we have included a profile for $\varepsilon = 1k_B T$ (dashed line). Bottom: profiles for driven systems at (c) $F_0 = 0.5k_B T/\sigma$ and (d) $F_0 = 3k_B T/\sigma$ and times $t = 0$ (solid), $t = \tau_B$ (dashed) and $t = 10\tau_B$ (dot-dashed). The total length of the microchannel is $L = 60\sigma$.

3.3. Influence of repulsive particle interactions

In many real colloidal systems, interactions between the particles cannot be neglected. In this section, we consider the case of purely repulsive interactions. Particles at positions z_1 and z_2 in the channel interact via a repulsive Gaussian potential $V^{\text{GCM}}(z_1 - z_2) = \varepsilon_0 \exp[-(z_1 - z_2)^2/\sigma^2]$ (with $\varepsilon_0 > 0$), a typical coarse-grained potential modeling a wide class of soft, partially penetrable macroparticles (e.g., polymer coils) with effective (gyration) radius σ [117; 93]. The particles are subject to a tilted washboard potential in a microchannel of finite length L (see section 3.2.5).

Typical distributions of the system in the absence of an external drive are illustrated in figure 14(a) and figure 14(b). Specifically, we consider the space-dependent one-particle density $\rho(z)$ at two values of the interaction strength ε . The particle number is fixed

to $N = \int_{-L/2}^{L/2} dz \rho(z, t) = 4$.

The data have been obtained numerically using equation (55), with the initial configuration ($t = 0$) being a single density peak centered in one potential well. The data in figure 14(a) pertain to a washboard potential of strength $U_0 = 15k_B T$. Here, thermal fluctuations are too weak to allow for barrier crossing within the observation time and, consequently, the particles remain localized in the potential well. This is true both for strong interactions ($\varepsilon = 4k_B T$) and in a small-coupling case ($\varepsilon = 1k_B T$), where the narrower peak of $\rho(z)$ suggests an even more pronounced localization. Figure 14(b) shows, for comparison, a profile corresponding to $U_0 = 3k_B T$ (and $\varepsilon = 4k_B T$, $F_0 = 0$), yielding a fluid-like situation with the density becoming non-zero everywhere. Within our calculations, we did not identify a threshold value of U_0 separating the two regimes, consistent with the continuous dependence of the equilibrium mobility on U_0 in the corresponding (exactly solvable) single-particle problem [94].

In the following, we focus on the more interesting localized situation depicted in figure 14(a). As described in section 3.2.3, an effective motion of the particles can be induced by a constant tilting force $\mathbf{F}^{\text{bias}} = F_0 \hat{\mathbf{z}}$ (with $\hat{\mathbf{z}}$ being the unit vector in z -direction), corresponding to a linear potential $U^{\text{bias}}(z) = -F_0 z$. The non-equilibrium dynamics of the driven system is investigated via the DDFT equation (55). Here we employ the mean-field (MF) approximation for the excess free energy, that is, $\mathcal{F}^{\text{int}} = (1/2) \int dz_1 \int dz_2 \rho(z_1, t) V^{\text{GCM}}(|z_1 - z_2|) \rho(z_2, t)$. Due to the penetrable nature of the Gaussian potential (which allows an, in principle, infinite number of neighbors) the MF approximation is known to become quasi-exact in the high-density limit and yields reliable results even at low and moderate densities [93].

The impact of the external drive on the density profile is illustrated in figure 14(c) and figure 14(d), where we consider two values of the driving strength F_0 . The numerical calculations have been performed in channels with closed boundaries, such that any drift motion is, strictly speaking, of transient character. However, by choosing channels of sufficient lengths ($L \geq 60\sigma$) we have ensured that all shown profiles are free of boundary effects.

In the small-drive situation depicted in figure 14(c) ($F_0 = 0.5k_B T/\sigma$), the peak barely moves within the time range considered, indicating that the probability for the particles to jump over the barriers is still small. This changes at $F_0 = 3k_B T/\sigma$ [see figure 14(d)] where the drive causes a shift of the entire density peak to the right. At the same time, the distribution broadens in the sense that now several potential wells are (potentially) occupied by particles. The influence of F_0 is also reflected by the time-dependence of the mean-squared displacements (MSD), $w(t) = N^{-1} \sum_{i=1}^N \langle (z_i(t) - z_i(0))^2 \rangle$. Since, within the DDFT formalism, we do not have direct access to the particle positions,

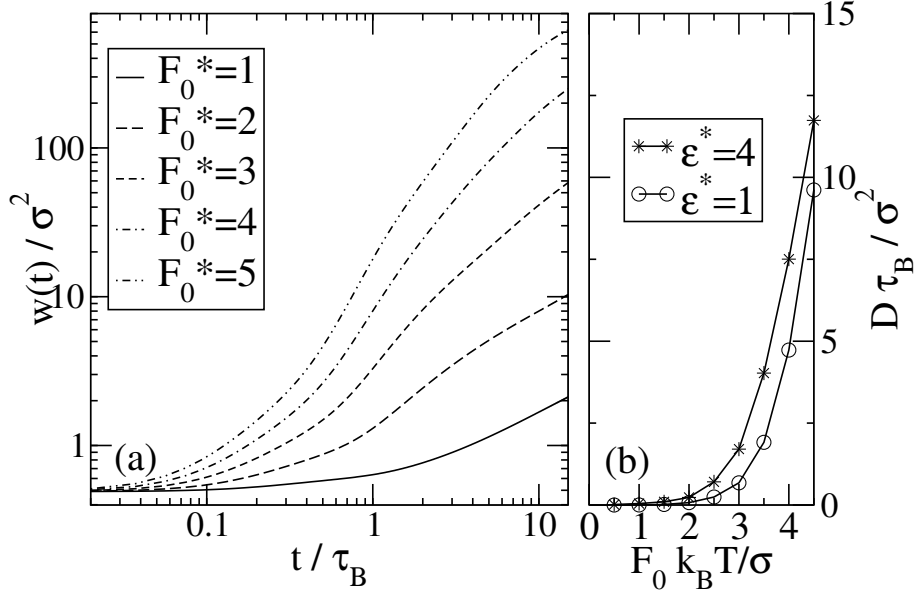


Figure 15.: (a) Mean-square displacement as a function of time at several driving strengths ($\epsilon = 4k_B T$, $N = 4$) and (b) corresponding diffusion constants. Included are data for $\epsilon = 1k_B T$.

we obtain the MSD rather via the relation $w(t) = \int_{-\infty}^{+\infty} dz z^2 G_s(z, t)$. Here, $G_s(z, t)$ is the self-part of the van Hove correlation function measuring the probability that a particle moves over a distance z during time t . We calculate this function, as well as its distinct counterpart $G_d(z, t)$ measuring the time dependence of two-particle correlations, within the DDFT formalism via the test particle method (see section 2.3). Some numerical results for the resulting MSD are given in figure 15(a); corresponding diffusion constants $D = \lim_{t \rightarrow \infty} w(t)/2t$ are plotted in figure 15(b).

Within the time range considered, we find diminutive values of D for driving strength $F_0 \lesssim 0.5k_B T/\sigma$, consistent with the behavior of the density profile in figure 14(c). Upon further increase of F_0 , the MSD at intermediate times first displays sub-diffusion (where $w(t)$ increases slower than linearly with t) and then superdiffusion characterized by much faster growth. In the long-time limit, the systems reach true diffusive behavior with $w(t) \propto t$ as expected from the Brownian friction incorporated in the DDFT. Exemplary data for the functions $G_s(z, t)$ [at $F_0 = 3k_B T/\sigma$] are plotted in figure 16(a). The appearance of several peaks in $G_s(z, t)$ reflects the existence of several "populations" of particles, one consisting of particles that remain in their original potential valley and the other ones consisting of moving particles. Clearly, the self-van Hove function

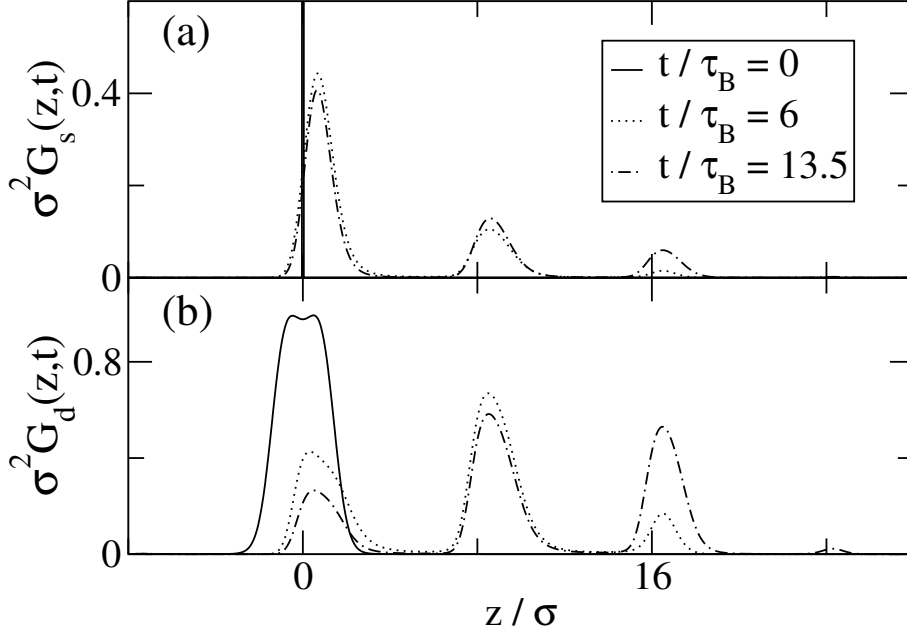


Figure 16.: (a) and (b) show the self and distinct part of the van Hove function at $F_0 = 3k_B T / \sigma$, $\varepsilon = 4k_B T$, and some characteristic times.

strongly deviates from the gaussian behavior expected in a "normal", liquid-like diffusing system.

Coming back to figure 15(b) we note that the maximum value of F_0 considered here is still smaller than the "critical" force $F_{\text{crit}} = \max(dU^{\text{wb}}/dz) \approx 5.9k_B T / \sigma$, beyond which the potential barriers are eliminated, and a single particle can slide freely. Therefore, we do not see the maximum and subsequent decrease of D expected in the vicinity of F_{crit} [106; 57] (indeed, investigation of that range is hindered by the finite length of our system which eventually yields boundary effects). We recall in this context that the particles in our system are interacting such that one may expect deviations of the behavior of D from the uncorrelated case [118]. Indeed, as indicated in figure 15(b), a decrease of the coupling strength yields a shift of the curve $D(F_0)$ towards larger driving strength. Thus, the repulsive interactions in our model support the particles in crossing the barriers. Finally, figure 16(b) shows the distinct van Hove function, $G_d(z, t)$, as calculated by the test particle method [83]. At $t = 0$, where G_d is proportional to the usual pair distribution function, the correlations are restricted to the first potential well in which the particle where confined initially (note the correlation hole at $t = 0$). At later times $G_d(z, t)$ develops additional peaks in

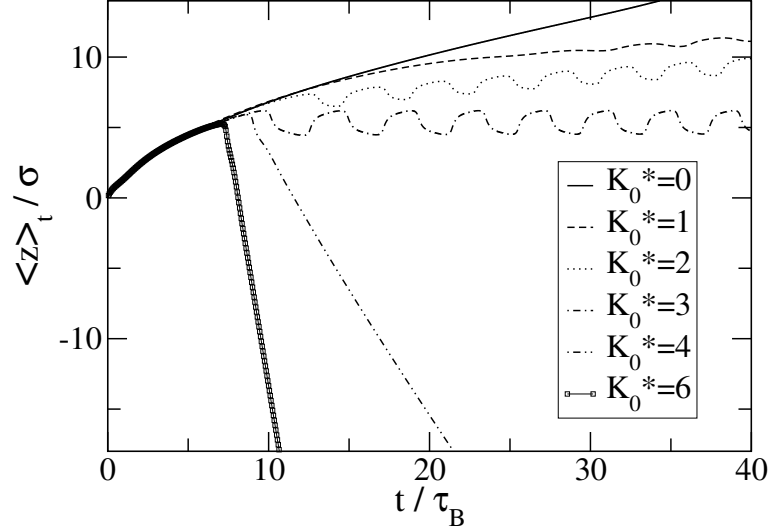


Figure 17.: Normalized first moment as a function of time for various control amplitudes K_0 (see equation (97)). The parameters are $F_0 = 3k_B T / \sigma$, $\tau = \tau_B$, $t_{\text{start}} = 1.5\tau_B$.

the neighboring potential valleys at $z > 0$, indicating pronounced spatiotemporal correlations in the driven system.

We now turn to the dynamics under time-delayed feedback control. We explore two distinct control strategies. The first protocol is chosen to be the same as in equation (80), that is,

$$F_1^c(t, \tau) = -K_0 (1 - \tanh [\bar{f}(t) - \bar{f}(t - \tau)]), \quad (97)$$

where \bar{f} is the first moment of the density corresponding to the average particle position [see equation (81)]. In the numerical calculations we switch on the control force at $t_{\text{start}} = 1.5\tau_B$ [i.e., $F_1^c(t < t_{\text{start}}) = 0$].

The impact of the control force F_1^c on the normalized first moment $\langle z \rangle_t = \bar{f}(t) / N$ is illustrated in figure 17, where we have chosen $F_0 = 3k_B T / \sigma$ and $\tau = \tau_B$. This delay time corresponds roughly to an intrinsic time scale of the system. Indeed, as seen from figure 15(a), $t = \tau_B$ is within the time range where the crossover from sub-diffusive into diffusive behavior of the MSD of the uncontrolled system occurs.

In the absence of control ($K_0 = 0$) the first moment plotted in figure 17 just increases with t , reflecting the rightward motion expected at $F_0 = 3k_B T / \sigma$ [see figure 14(d)]. The slope of the function $\langle z \rangle_t$ at large t may be interpreted as an average velocity

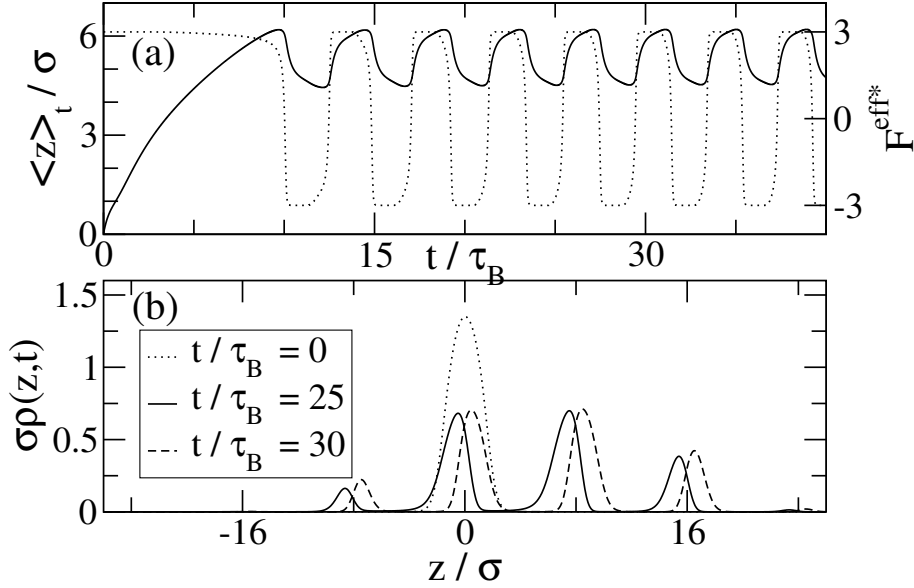


Figure 18.: (a) First moment (solid line) and effective bias (dashed) at $K_0 = 3k_B T/\sigma$. (b) Density profiles for various times ($F_0 = 3k_B T/\sigma$, $\tau = \tau_B$, $t_{\text{start}} = 1.5\tau_B$).

$v = \lim_{t \rightarrow \infty} (d\langle z \rangle_t / dt)$. Increasing K from zero, the velocity first decreases until the peak motion stops (i.e., the time-average of $\langle z \rangle_t$ becomes constant) at $K_0 = 3k_B T/\sigma$. This value corresponds to a balance between control force and bias. Even larger control amplitudes then result in a significant backward motion, i.e., $\langle z \rangle_t$ and v become negative.

We now consider in more detail the time-dependence of the feedback control. First, a significant influence on $\langle z \rangle_t$ appears only at relatively large times $t \gg t_{\text{start}}$ (which depend, in turn, on the actual value of K_0). At earlier times, the density peak moves so quickly that $\bar{f}(t) \gg \bar{f}(t - \tau)$ and the tanh-function in equation (97) approaches 1, yielding $F_1^c(t, \tau) \approx 0$. With the "slow-down" of $\langle z \rangle_t$ at somewhat later times (visible also at $K_0 = 0$), the argument of the tanh decreases. Thus, the control sets in, yielding an effective biasing force $F^{\text{eff}}(t) = F_0 + F_1^c(t; \tau) \leq F_0$. The behavior of $F^{\text{eff}}(t)$ and the function $\langle z \rangle_t$ is shown in figure 18(a) for the "balanced" case $K_0 = 3k_B T/\sigma$. One sees that the control becomes effective at $t \approx 10\tau_B$. After that, the first moment displays an oscillating behavior changing between small backward motion and forward motion. These oscillations yield, in turn, oscillations of $F^{\text{eff}}\sigma/k_B T$ between its maximum value, $F_0 = 3k_B T/\sigma$, and its minimum $F_0 - 2K_0 = -3k_B T/\sigma$. As a consequence, the overall motion stops. Interestingly, the oscillations (which seem to persist in the long-time

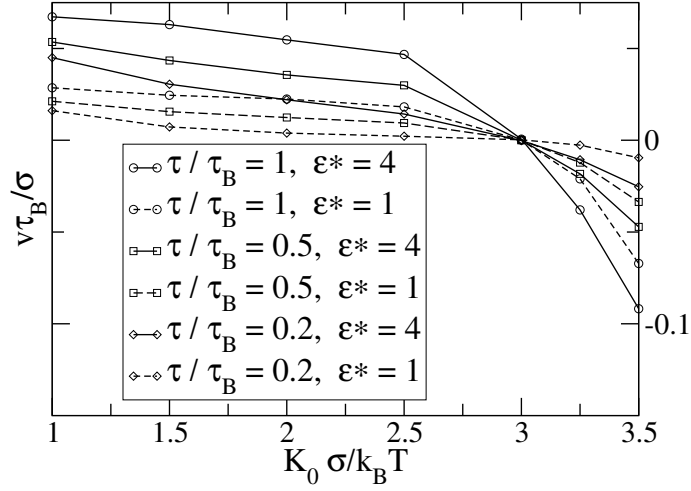


Figure 19.: Long-time velocity as function of K_0 for several values of τ and ε ($F_0 = 3k_B T/\sigma$, $t_{\text{start}} = 1.5\tau_B$). Lines are guides for the eye.

limit) have a period of about $5\tau_B$, that is, much larger than the delay time ($\tau = \tau_B$). Density profiles related to one "cycle" of $\langle z \rangle_t$ and $F^{\text{eff}}(t)$ are plotted in figure 18(b), where $t/\tau_B = 25$ and 30 correspond roughly to the minimum and maximum of F^{eff} , respectively [see figure 18(a)]. It is seen that the entire particle distribution is shifted with the periodic changes of F^{eff} . These shifts are accompanied by changes in the peak shapes, which become most asymmetric when F^{eff} is minimal, i.e., the control is maximal ($t/\tau_B = 25$). To complete the picture, we plot in figure 19 the long-time velocity v (averaged over the oscillations of $\langle z \rangle_t$, if present) as function of the control amplitude. We have included data for different delay times τ and different interaction (i.e., repulsion) strengths ε . All systems considered display a clear current reversal at $K_0 = 3k_B T/\sigma$, where the velocity v changes from positive to negative values irrespective of ε and τ . These parameters, however, do have an impact on the magnitude of the velocities in the two regimes $K_0 < 3k_B T/\sigma$ and $K_0 > 3k_B T/\sigma$. Specifically, reduction of ε (at fixed τ) yields a decrease of v as compared to the case $\varepsilon = 4k_B T$. Similarly, v decreases in magnitude when the delay time decreases (at fixed ε) from $\tau = \tau_B$ towards $\tau = 0.2\tau_B$. In other words, the time delay supports the current reversal in the parameter range considered. We also note that all of these results are robust, on a qualitative level, against slight changes of the control protocol, such as a reversal the argument of the transcendental function in equation (97).

The control scheme considered so far focuses on the average particle position. However, given that the basic dynamical variable in DDFT is the density profile $\rho(z, t)$, it is

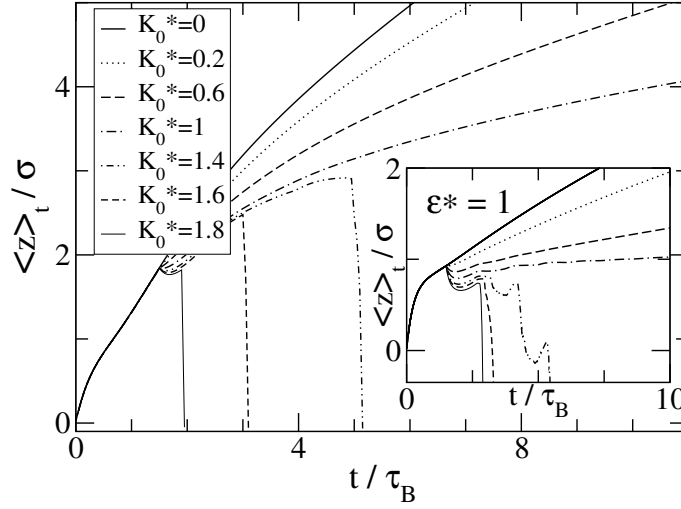


Figure 20.: Normalized first moment as a function of time and various control amplitudes K_0 for the second control loop (see equation (98)) and $\varepsilon = 4k_B T$. The inset contains data for $\varepsilon = 1k_B T$ at otherwise same parameters $F_0 = 3k_B T / \sigma$, $\tau = \tau_B$, and $t_{\text{start}} = 1.5\tau_B$.

interesting to briefly discuss a control loop based on that quantity. Specifically, we consider the potential

$$U_2^c(z, [\rho]) = -K_0 z (1 - \tanh[\rho(z, t - \tau) - \rho(z, t)]). \quad (98)$$

The impact of this scheme on the function $\langle z \rangle_t$ is shown in figure 20, where the inset contains data for the weakly interacting case $\varepsilon = 1k_B T$.

For small control amplitudes ($K < 1k_B T / \sigma$), the behavior of both systems, $\varepsilon = 4k_B T$ and $\varepsilon = 1k_B T$, is similar to what is observed with the previous control loop [see equation (97)] in the sense that the long-time velocity decreases with increasing K . However, contrary to this previous loop, further increase of K then yields an abrupt reversal of the motion, that is, the particles "bounce backwards" in the sense that $v \rightarrow -\infty$. Moreover, this abrupt change occurs at values of K much smaller than the biasing force ($F_0 = 3k_B T / \sigma$). The spatiotemporal behavior of the microscopic density profile $\rho(z, t)$ related to the sudden reversal of motion is illustrated in figure 21. At $t = 3.5\tau_B$, that is, before the reversal, the initial density peak centered at $z = 0$ has extensions to the next potential wells at positive z , indicating that the particles move rightwards. However, already at this time, there is a small bump at positions $z < 0$ not present within the first control scheme [see figure 18(b)]. At time $t = 5\tau_B$ after the

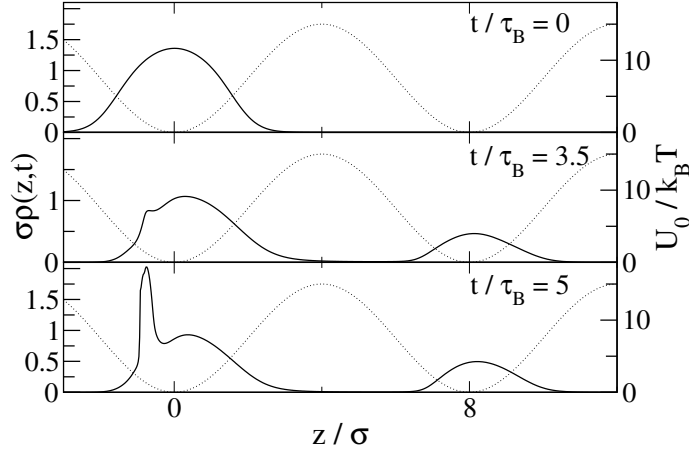


Figure 21.: Density profiles at some characteristic times for $K_0 = 1.4k_B T/\sigma$. The washboard potential is indicated by the dotted lines.

reversal this additional bump has increased significantly along with a left-ward shift of the center of mass. In a future publication we will analyze in more detail to which extent the sudden reversal and the associated complex behavior of $\rho(z, t)$ is a true instability. Nevertheless, already the results in figure 20 indicate that a local control scheme could be more efficient, in the sense that much smaller perturbations K are required to yield current reversal, compared to control focussing on a space-averaged quantity.

We briefly address the question if the oscillatory state is affected by the repulsive interaction. To this end, we turn our attention back to the circular ring geometry (see section 3.2.3) and consider the case of $N = 2$. We note that, even in the non-interacting case, the results from the linear stability analysis from section 3.2.1 cannot be used as a basis for comparison. The reason is that the calculations in section 3.2.1 were done with $N = 1$. Rather, the washboard amplitude U_0 must be increased significantly to find a stable stationary state. For example, for the “balanced case” $\tilde{\gamma} = F_0 - K_0 = 0$ (and $\varepsilon_0 = 0$) we find oscillatory density states for a broad spectrum of values for U_0 ranging up to $U_0 \approx 14k_B T$ (recall that $U_0 = 8k_B T$ is sufficient to suppress oscillatory states for $N = 1$ and the rest of the parameters being the same).

In figure 22 we show results for the average particle position $\langle z \rangle_t$ for $U_0 = 15k_B T$ and $N = 2$. In the case of the non-interacting system $\varepsilon_0 = 0$ (shown as a solid curve in figure 22) the function $\langle z \rangle_t$ is indeed being damped as a function of time, reflecting a stationary state for times larger than the transient response time, which is here of the

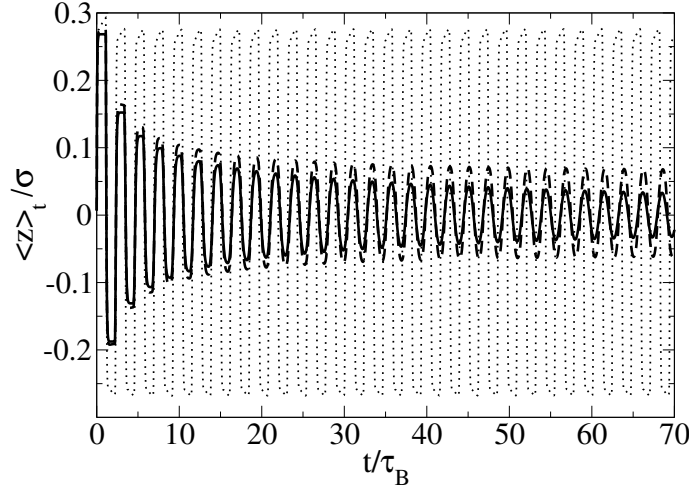


Figure 22.: Results for the average particle position $\langle z \rangle_t$ as a function of time for different repulsion strengths: $\varepsilon_0 = 0k_B T$ (solid curve), $\varepsilon_0 = 12k_B T$ (dashed curve) and $\varepsilon_0 = 15k_B T$ (dotted curve). The parameters are $U_0 = 15k_B T$, $F_0 = 7k_B T/\sigma$, $K_0 = 7k_B T/\sigma$, $\tau = \tau_B$, $L = 10\pi\sigma$ and $N = 2$.

order of $t_{\text{res}} \approx 2000\tau_B$.

Upon increase of the repulsion strength ε_0 the extrema of the function $\langle z \rangle_t$ increase (see the dashed curve and the dotted curve in figure 22, respectively). This is consistent with our earlier finding that repulsive interactions support the particles in crossing the barrier (see e.g. figure 15), yielding an increase of the long-time diffusion coefficient. Moreover, for $\varepsilon_0 = 15k_B T$ we find stable (time-periodic) density oscillations with cycle time $T = 2.315\tau_B$. Thus, repulsive interparticle interactions can be successfully used to stabilize the oscillatory density state. We note, however, that for the present system increasing the average density (via the particle number N) has a considerably greater impact on the linear stability of the system.

3.4. Summary

In this chapter we have investigated the dynamics of colloidal particles subject to a one-dimensional, tilted washboard potential under time-delayed feedback control. One major point was to identify conditions under which the control can induce oscillatory states which are absent in the uncontrolled system. Our starting point was a non-

interacting system in the absence of pair interactions. We have investigated infinite systems with periodic boundaries and microchannels of finite length L bounded by repulsive walls. For the first case, we have obtained, based on linear stability analysis, a full state diagram. This diagram predicts that oscillations of the density field do indeed occur for finite values of the delay time and control strengths comparable to the strengths of the conservative forces. Investigating the time dependence of the same system via numerical solution of the DDFT equation, we found full consistency with the results of the linear stability analysis for all model parameters considered. In addition, the numerical solution provides results for the (likewise oscillating) moments of the density distribution. In particular, from the oscillations of the first moment (i.e., the current) we could identify the cycle time. The latter was found to monotonically decrease with the delay time. In the finite system which we have investigated via the DDFT approach alone, we also found oscillations. However, the spatial extension of these oscillations corresponds to the wall-to-wall separation, rather than to the width of one valley, as in the infinite-system case. Despite these differences, the parameter region where the finite system exhibits feedback-induced oscillations is rather similar to that found in the infinite case. We attribute this to the fact that the finite system under consideration was still so large ($L \gg \lambda_{\text{wb}} = \pi\sigma$), that boundary effects are not dominant.

As a next step we have considered the case that the colloidal particles interact. Using a purely repulsive (GCM) pair potential, we have demonstrated that the *transport* in an interacting, driven colloidal system can be efficiently manipulated by time-delayed feedback control. Specifically, our control goal here was to stop or reverse the motion in a tilted washboard potential below the critical driving strength F_{crit} beyond which the washboard becomes ineffective. We have shown that this goal can be achieved with different control schemes that involve the same delay time τ (chosen equal to the intrinsic, Brownian time scale) but different control targets (average particle position $\langle z \rangle_t$ versus density profile $\rho(z, t)$). Concerning the oscillatory states, we have shown that these are stabilized by repulsive interactions. However, to see this effect the strength of repulsion must be of the order of the washboard amplitude (and both must be significantly larger than $k_B T$).

The fact that the schemes produce comparable results indicates a certain robustness of the feedback control method for transport phenomena in 1D systems, consistent with earlier theoretical findings for ratchet systems [66; 71; 111; 70] and for non-interacting particles in tilted washboards [72; 73]. In that sense, our study also supports the more general perspective that time-delayed feedback control can be extremely useful for the manipulation of non-linear systems [68].

Taken together, we have shown that colloidal particles in modulated potentials under

time-delayed feedback control can display highly non-trivial dynamics, particularly oscillations. One way to understand these differences to the uncontrolled case is that our feedback control term, which relies on the average particle position and thus involves *all* particles, introduces effectively time-dependent interactions between the particles. We note that feedback-induced spatiotemporal effects have been recently also been found in other extended systems such as optical resonators, where the delayed feedback generates spontaneous motion of cavity solutions [78], and, more generally, systems describable by the Swift-Hohenberg equation [119].

4. The phase-separating magnetic mixture

In this chapter we turn our attention to the pattern formation in colloidal systems at surfaces. To this end, we extend our model from chapter 3 towards a binary mixture where one species carries a classical spin of Heisenberg type inducing additional attractive interactions. Heisenberg fluids [24; 25; 26; 27; 28] are basic models for continuum systems exhibiting ferromagnetic order, particularly for the description of ferromagnetism in undercooled liquid metal alloys. Indeed, for sufficiently large coupling strengths and densities, we find a demixing phase transition driven by the ferromagnetic interactions of the magnetic species.

We investigate states deep inside the two-phase region far away of the two-phase coexistence, the binodal, and from the spinodal, i.e. the line of points where the barrier for nucleation vanishes. Inside the spinodal region of the phase diagram density perturbations with certain wavenumbers k grow over time regardless of the amplitude. This eventually results in a demixing process, that is, spinodal decomposition [95; 120]. We provide a microscopic description (i.e., density profiles) of the resulting non-magnetic/magnetic fluid-fluid interface. We also consider the nucleation of non-magnetic clusters surrounded by the metastable bulk phase and compare the results of three models, namely classical nucleation theory, DFT and DDFT. Further, we address briefly the issue of the nucleation pathway.

Our investigations are based on DFT for the equilibrium phase behavior and DDFT for the demixing dynamics. Recently, DDFT has been applied to a variety of phase-separating systems including colloids with critical Casimir forces [121], colloidal mixtures under gravity [122], heterogeneous nucleation at solid surfaces [123; 124; 125], or even more far-reaching problems such as the growth of cancer cells [126].

4.1. Model

The fluid system that we investigate is a binary mixture composed of two species. One species (n) is composed of spherical particles which interact via purely isotropic and repulsive forces. The other species (m) consists of magnetic particles. In addition to the repulsive interaction induced by the particle cores, these particles carry magnetic moments. The interaction part of the Hamiltonian may therefore be decomposed into a core part and a contribution from the spin-spin interaction

$$\mathcal{H}^{\text{int}} = \frac{1}{2} \sum_{\alpha, \beta} \sum_{\substack{i, j=1 \\ i \neq j}}^N V^{\alpha\beta}(\mathbf{r}_i, \mathbf{r}_j, \mathbf{s}_i, \mathbf{s}_j), \quad (99)$$

where $\alpha, \beta = \{n, m\}$ and

$$V^{\alpha\beta}(\mathbf{r}_i, \mathbf{r}_j, \mathbf{s}_i, \mathbf{s}_j) = V_{\text{core}}(\mathbf{r}_i, \mathbf{r}_j) + V_{\text{mag}}(\mathbf{r}_i, \mathbf{r}_j, \mathbf{s}_i, \mathbf{s}_j) \delta_{\alpha, B} \delta_{\beta, B}. \quad (100)$$

In our model, the particles are confined to a (two-dimensional) plane, so that the position of particle i , denoted $\mathbf{r}_i = (x_i, z_i)$, but the magnetic moment is represented by a three-dimensional normalized classical spin \mathbf{s}_i whose orientation is described by the Euler angles $\omega = (\theta, \varphi)$. For the magnetic interaction, we choose the Heisenberg model,

$$V_{\text{mag}}(|\mathbf{r} - \mathbf{r}'|, \omega, \omega') = J(|\mathbf{r} - \mathbf{r}'|) \mathbf{s}_1 \cdot \mathbf{s}_2, \quad (101)$$

where $J(|\mathbf{r} - \mathbf{r}'|)$ determines the range of the spin-spin interaction. We further assume that $J(|\mathbf{r} - \mathbf{r}'|)$ can be described by Yukawa's potential, that is,

$$J(|\mathbf{r} - \mathbf{r}'|) = \begin{cases} 0, & \text{if } |\mathbf{r} - \mathbf{r}'| < \sigma, \\ -J \frac{e^{-(|\mathbf{r} - \mathbf{r}'|/\sigma - 1)}}{|\mathbf{r} - \mathbf{r}'|/\sigma}, & \text{else.} \end{cases} \quad (102)$$

For interparticle distances $|\mathbf{r} - \mathbf{r}'| < \sigma$ the interaction between two magnetic particles is assumed to be small as compared to the repulsion from the core potentials (see below) and we therefore set the Yukawa potential in our model to zero in this region. The sign of the coupling constant $J^* = J/(k_B T)$ in equation (102) determines which type of spin ordering is preferred. As we show below in section 4.2.2, the choice $J^* > 0$ yields a spontaneous ferromagnetic ordering of the magnetic component of the mixture at temperatures T below a Curie temperature T_C . On the other hand, the choice $J^* < 0$ favors antiferromagnetic ordering.

The Heisenberg model has been successfully applied to spin fluids with ferromagnetic ordering where the Heisenberg spin exchange dominates the magnetic dipole-dipole coupling. Paradigm examples are liquid alloys with a melting point below the Curie temperature such as Co/X alloys where the primary constituent is the metallic element cobalt and X is the secondary constituent, e.g., gold [127] or the nonmetallic element phosphorus [128].

To model the repulsion between the particles, we choose a Gaussian with height ε and width σ . The resulting ‘‘Gaussian core’’ model (GCM), first studied by Stillinger [129], is given by

$$V_{\text{core}}(|\mathbf{r} - \mathbf{r}'|) = \varepsilon \exp(-|\mathbf{r} - \mathbf{r}'|^2/\sigma^2). \quad (103)$$

The GCM is often used as an approximation for the effective interactions between the centre of mass of two ‘‘soft’’ particles, such as polymers and star-polymers [130; 117] or dendrimers [131; 132; 133]. The dimensionless quantity $\varepsilon^* = \varepsilon/(k_B T) > 0$ determines the strength of the repulsion, and the range parameter σ roughly corresponds to the radius of gyration of the ‘particles’. For the magnetic interaction, we choose a positive coupling constant $J^* > 0$. Hence, in the ferromagnetic phase the magnetic contribution to the pair potential acts effectively as an attractive tail to the repulsive (soft) core.

4.2. Equilibrium theory of the demixing transition

4.2.1. The density functional for the mixture

The central quantity in density functional theory is the singlet (one body) density distribution $\rho_\alpha(\mathbf{r}, \omega)$. Following other studies of molecular magnetic fluids [24] we assume that the singlet density can be factorized into a translational (number density) part, $\rho_\alpha(\mathbf{r})$, and an orientational distribution function, $h_\alpha(\mathbf{r}, \omega)$, that is,

$$\rho_\alpha(\mathbf{r}, \omega) = \rho_\alpha(\mathbf{r})h_\alpha(\mathbf{r}, \omega). \quad (104)$$

The orientational distribution is normalized, so that,

$$\int d\omega h_\alpha(\mathbf{r}, \omega) = 1, \quad (105)$$

which yields $h_n = 1/(4\pi)$ for the particles without orientational degrees of freedom (non-magnetic species). The equilibrium fluid singlet density distribution is that which minimizes the grand free energy functional [45]

$$\Omega[\{\rho_\alpha\}] = \mathcal{F}[\{\rho_\alpha\}] - \sum_\alpha \int d\omega \int d\mathbf{r} [\mu_\alpha - V_{\text{ext}}(\mathbf{r}, \omega)] \rho_\alpha(\mathbf{r}, \omega), \quad (106)$$

where \mathcal{F} is the Helmholtz free energy functional and μ_α denotes the chemical potential for species α . Note also that $\int d\mathbf{r} = \int dx \int dz$ denotes a two-dimensional spatial integral. For a given external potential V_{ext} and interaction potentials, the functional in equation (106) has a minimum at the equilibrium density $\rho_\alpha^0(\mathbf{r}, \omega)$. The functional $\Omega_V[\{\rho_\alpha^0\}]$ is then identical to the grand canonical potential Ω (cf. reference [45]). In the present study we set the external potential $V_{\text{ext}} = 0$. The Helmholtz free energy functional can be split up into two contributions:

$$\mathcal{F}[\{\rho_\alpha\}] = \mathcal{F}_{\text{id}}[\{\rho_\alpha\}] + \mathcal{F}_{\text{ex}}[\{\rho_\alpha\}], \quad (107)$$

where $\mathcal{F}_{\text{id}}[\{\rho_\alpha\}] = \sum_\alpha \int d\mathbf{r} \int d\omega \rho_\alpha(\mathbf{r}, \omega) [\ln(\Lambda_\alpha^2 \rho_\alpha(\mathbf{r}, \omega)) - 1]$ is the ideal gas contribution and $\mathcal{F}_{\text{ex}}[\{\rho_\alpha\}]$ is the excess part. Using equations (104) and (105), the ideal gas contribution becomes

$$\mathcal{F}_{\text{id}}[\{\rho_\alpha\}] = k_B T \int d\mathbf{r} \rho_n(\mathbf{r}) \left[\ln(\Lambda_n^2 \rho_n(\mathbf{r})) - \ln 4\pi - 1 \right] \quad (108)$$

$$+ k_B T \int d\mathbf{r} \rho_m(\mathbf{r}) \left[\ln(\Lambda_m^2 \rho_m(\mathbf{r})) - 1 \right] \\ + k_B T \int d\mathbf{r} \rho_m(\mathbf{r}) \int d\omega h_m(\mathbf{r}, \omega) \ln [h_m(\mathbf{r}, \omega)], \quad (109)$$

where Λ_α denotes the thermal de Broglie wavelength of species α . The particle interactions enter into the excess part of the free energy functional, which can be written as [45]

$$\mathcal{F}_{\text{ex}}[\{\rho_i\}] = \frac{1}{2} \sum_{\alpha, \beta} \int_0^1 d\lambda \int d\mathbf{r} \int d\mathbf{r}' \int d\omega \int d\omega' \\ \times \rho_{\alpha\beta}^{(2)}(\mathbf{r}, \mathbf{r}', \omega, \omega'; \lambda) V^{\alpha\beta}(|\mathbf{r} - \mathbf{r}'|, \omega, \omega'). \quad (110)$$

Equation (110) is exact for systems with pair interactions. The function $\rho_{\alpha\beta}^{(2)}(\mathbf{r}, \mathbf{r}', \omega, \omega'; \lambda)$ is the two-body density distribution function which is determined by the pair inter-

actions $V^{\alpha\beta}(|\mathbf{r} - \mathbf{r}'|, \omega, \omega')$, and λ is a ‘‘charging’’ parameter (cf. section 2.1.5). In general, the function $\rho_{\alpha\beta}^{(2)}$ is not known exactly. Here we employ a mean-field (MF) approximation by setting $\rho_{\alpha\beta}^{(2)}(\mathbf{r}, \mathbf{r}', \omega, \omega'; \lambda) = \rho_{\alpha}(\mathbf{r}, \omega)\rho_{\beta}(\mathbf{r}', \omega')$, i.e. that the pair correlation function is set to one. Previous studies [117; 93] have shown that this simple MF approximation for the GCM yields reliable results for the fluid structure and thermodynamics, particularly at higher densities. Within the MF approximation, the excess part of the Helmholtz free energy may be written as the following sum

$$\mathcal{F}_{\text{ex}} = \mathcal{F}_{\text{ex}}^{nn} + \mathcal{F}_{\text{ex}}^{mm} + \mathcal{F}_{\text{ex}}^{nm} + \mathcal{F}_{\text{ex}}^{mn} \quad (111)$$

where the contribution due to the interactions between the non-magnetic particles is

$$\mathcal{F}_{\text{ex}}^{nn}[\{\rho_n\}] = \frac{1}{2} \int d\mathbf{r} \int d\mathbf{r}' \rho_n(\mathbf{r})\rho_n(\mathbf{r}')V_{\text{core}}(|\mathbf{r} - \mathbf{r}'|), \quad (112)$$

and for the magnetic particles

$$\begin{aligned} \mathcal{F}_{\text{ex}}^{mm}[\{\rho_m\}] &= \frac{1}{2} \int d\omega \int d\omega' h_m(\mathbf{r}, \omega)h_m(\mathbf{r}', \omega') \int d\mathbf{r} \int d\mathbf{r}' \\ &\times \rho_m(\mathbf{r})\rho_m(\mathbf{r}') \left[V_{\text{core}}(|\mathbf{r} - \mathbf{r}'|) + J(|\mathbf{r} - \mathbf{r}'|)\mathbf{s} \cdot \mathbf{s}' \right]. \end{aligned} \quad (113)$$

The contributions $\mathcal{F}_{\text{ex}}^{nm}$ and $\mathcal{F}_{\text{ex}}^{mn}$ to the excess free energy functional are equal because of the symmetry of the pair potentials between both species [cf. equation (100)], that is,

$$\begin{aligned} \mathcal{F}_{\text{ex}}^{nm}[\{\rho_{\alpha}\}] &= \frac{1}{2} \int d\mathbf{r} \int d\mathbf{r}' \rho_n(\mathbf{r})\rho_m(\mathbf{r}')V_{\text{core}}(|\mathbf{r} - \mathbf{r}'|) \\ &= \mathcal{F}_{\text{ex}}^{mn}[\{\rho_{\alpha}\}] \end{aligned} \quad (114)$$

The equilibrium densities $\rho_{\alpha}^{(0)}(\mathbf{r}, \omega)$ are found by minimizing the grand free energy functional given in equation (106):

$$\begin{aligned} \left. \frac{\partial \Omega[\rho_{\alpha}, h]}{\partial \rho_{\alpha}(\mathbf{r})} \right|_{\rho_{\alpha}^{(0)}(\mathbf{r})} &= 0, \\ \left. \frac{\partial \Omega[\rho_{\alpha}, h]}{\partial h_{\alpha}(\mathbf{r}, \omega)} \right|_{h_{\alpha}^{(0)}(\mathbf{r}, \omega)} &= 0. \end{aligned} \quad (115)$$

Equation (115) yields an implicit equation for $h_m(\mathbf{r}, \omega)$,

$$h_m(\mathbf{r}, \omega) = \frac{\exp(\mathbf{B}(\mathbf{r}) \cdot \mathbf{s}(\omega))}{\int d\omega \exp(\mathbf{B}(\mathbf{r}) \cdot \mathbf{s}(\omega))}, \quad (116)$$

where the effective field is given by

$$\mathbf{B}(\mathbf{r}) = -\int d\mathbf{r}' \int d\omega' \rho_m(\mathbf{r}') h_m(\mathbf{r}', \omega') J(|\mathbf{r} - \mathbf{r}'|) \mathbf{s}'. \quad (117)$$

Thus, the orientational distribution is determined solely by the scalar product between the spin and the effective field $\mathbf{B}(\mathbf{r})$. This is an exact result within the MF approximation, which has been previously applied also to three-dimensional Heisenberg fluids [27; 28; 24] as well as in other contexts such as in liquid crystal theory [134].

In the low-temperature ferromagnetic state, the orientational order is uniaxial with respect to a director \mathbf{n} . Thus, the angular distribution reduces to $h_m(\mathbf{r}, \omega) = h_m(\mathbf{r}, u)$, where $u = \mathbf{s} \cdot \mathbf{n} = \cos \theta$. The integration over orientation in equation (117) then becomes [24; 28]

$$\int d\omega' h_m(\mathbf{r}', \omega') \mathbf{s}' \longrightarrow 2\pi \int_{-1}^1 du h_m(\mathbf{r}, u) u = L(\mathbf{r}), \quad (118)$$

where $L(\mathbf{r}) = \coth B(\mathbf{r}) - 1/B(\mathbf{r})$ is the Langevin function. The latter also defines the local magnetization $M(\mathbf{r}) = \int d\omega h_m(\mathbf{r}, \omega) \cos \theta = L(\mathbf{r})$. Inserting equation (118) into equation (113), the Heisenberg contribution to the free energy functional can be written as

$$\begin{aligned} \mathcal{F}_{\text{ex}}^{mm}[\rho] = & \frac{1}{2} \int d\mathbf{r} \int d\mathbf{r}' \rho_m(\mathbf{r}) \rho_m(\mathbf{r}') \\ & \times \left[V_{\text{core}}(|\mathbf{r} - \mathbf{r}'|) + L(\mathbf{r})L(\mathbf{r}')J(|\mathbf{r} - \mathbf{r}'|) \right]. \end{aligned} \quad (119)$$

4.2.2. Phase behavior

In this section, we employ the density functional approach introduced above to investigate the phase behavior of the bulk binary mixture. We restrict ourselves to fluid phases. The state of the system can be characterized by the strength of the repulsion $\varepsilon^* = \varepsilon/(k_B T)$, the magnetic coupling parameter $\delta = J/\varepsilon$, the reduced total number density $\rho\sigma^2$ in the system, and the concentration x of the magnetic component.

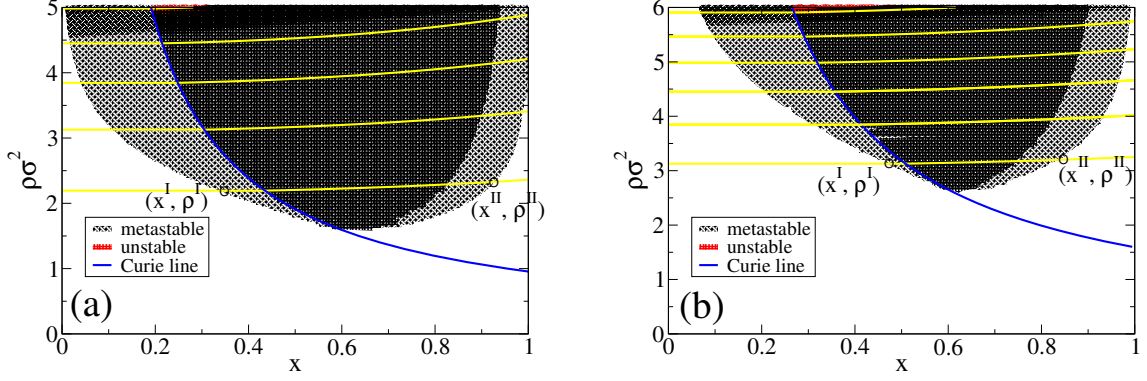


Figure 23.: The phase diagram for a two-component GCM mixture, where one component is characterized by an additional Heisenberg interaction. The coupling parameters are (a) $\varepsilon^* = 5.0$, $\delta = 0.1$ and (b) $\varepsilon^* = 5.0$, $\delta = 0.06$. The yellow lines are isobars with line-to-line pressure difference of $\Delta P^* = \Delta P \sigma^2 / (k_B T) = 40$. The black circles denote coexisting state points for $P^* = 40$ (a) and $P^* = 80$ (b), respectively. In (a) the highest isobar indicated corresponds to $P^* = 160$, and the (tri)critical point occurs at $\rho_c \sigma^2 = 1.5$, $x_c = 0.63$. The corresponding data in (b) is $P^* = 280$, $\rho_c \sigma^2 = 2.6$, and $x_c = 0.61$.

The densities of the individual component can then be written as $\rho_n = (1 - x)\rho$ and $\rho_m = x\rho$. Assuming that the system is homogeneous, the Helmholtz free energy per particle $f = \mathcal{F}/N$ follows from equations (107)-(110) as

$$\begin{aligned}
 f^{\text{MF}}(\rho, x) &= f_{\text{id}}(\rho, x) + f_{\text{ex}}^{\text{MF}}(\rho, x) \\
 &= x \ln x + (1 - x) \ln(1 - x) + x \int d\omega h_m(\omega) \ln [h_m(\omega)] + \\
 &\quad \frac{1}{2} \rho \left[(1 - x)^2 \hat{V}^{nn}(0) + 2x(1 - x) \hat{V}^{nm}(0) + x^2 \hat{V}^{mm}(0) \right]. \quad (120)
 \end{aligned}$$

In equation (120), the coupling matrix elements $\hat{V}^{nn}(0)$ and $\hat{V}^{nm}(0)$ denote the integrated strength of the repulsive core potential, or equivalently the $k \rightarrow 0$ limit of the Fourier transform of equation (103), that is,

$$\hat{V}^{nn}(0) = \int d\mathbf{r} V_{\text{core}}(|\mathbf{r}|) = \hat{V}^{nm}(0). \quad (121)$$

The element $\hat{V}^{mm}(0)$ involves, in addition, an integral over the magnetic interaction, i.e.

$$\begin{aligned} \hat{V}^{mm}(0) &= \int d\mathbf{r} V_{\text{core}}(|\mathbf{r}|) \\ &+ \int d\mathbf{r} \int d\omega \int d\omega' h_B(\omega) h_B(\omega') J(|\mathbf{r}|) \mathbf{s} \cdot \mathbf{s}'. \end{aligned} \quad (122)$$

In the following, we investigate the possibility of fluid-fluid phase separation. The thermodynamic stability conditions for a binary mixture are given by [93; 34]

$$\begin{aligned} \left(\frac{\partial^2 f}{\partial \nu^2} \right)_x &> 0, \\ \left(\frac{\partial^2 f}{\partial x^2} \right)_\nu &> 0, \\ \left(\frac{\partial^2 f}{\partial \nu^2} \right)_x \left(\frac{\partial^2 f}{\partial x^2} \right)_\nu - \left(\frac{\partial^2 f}{\partial \nu \partial x} \right)^2 &> 0, \end{aligned} \quad (123)$$

where $\nu = 1/\rho$ is the volume per particle. The first stability condition expresses that the compressibility must be positive, the second ensures stability against spontaneous demixing at constant volume, and the last inequality is the condition for stability at constant pressure. As shown in previous studies [34], it is more convenient to use these stability conditions in a constant-pressure ensemble. To this end, we perform a Legendre transform of the Helmholtz free energy per particle, yielding the Gibbs free energy per particle

$$g(x, P) = f(x, \nu) - \left(\frac{\partial f}{\partial \nu} \right)_x \nu. \quad (124)$$

For two phases I and II to coexist in equilibrium, the chemical potentials of each species $\alpha = n, m$ have to be equal, and the same holds for the pressure and the temperature. In other words, one has $\mu_\alpha^{\text{I}}(\rho_n^{\text{I}}, \rho_m^{\text{I}}) = \mu_\alpha^{\text{II}}(\rho_n^{\text{II}}, \rho_m^{\text{II}})$, $P^{\text{I}}(\rho_n^{\text{I}}, \rho_m^{\text{I}}) = P^{\text{II}}(\rho_n^{\text{II}}, \rho_m^{\text{II}})$ and $T^{\text{I}}(\rho_n^{\text{I}}, \rho_m^{\text{I}}) = T^{\text{II}}(\rho_n^{\text{II}}, \rho_m^{\text{II}})$, where $\rho_\alpha^{\text{I(II)}}$ are the densities of the components in the two phases. These equilibrium conditions lead to a common-tangent construction on the

Gibbs free energy,

$$\left(\frac{\partial g}{\partial x}\right)_P \Big|_{x_I} = \left(\frac{\partial g}{\partial x}\right)_P \Big|_{x_{II}} = \frac{g(x_I, P) - g(x_{II}, P)}{x_I - x_{II}}, \quad (125)$$

where P is the (bulk) pressure at coexistence. The spinodal is given by the inflection points of g , that is

$$\left(\frac{\partial^2 g}{\partial x^2}\right)_P = 0. \quad (126)$$

Figure 23 shows the phase diagram for the (2D) bulk binary mixture whose free energy is given by equation (120). We consider a fixed repulsion strength $\varepsilon^* = 5.0$ and two different magnetic coupling parameters, $\delta = J^*/\varepsilon^* = 0.1$ and $\delta = 0.06$. For both parameter sets we find a first-order demixing phase transition appearing at densities above a critical density ρ_c . Moreover, the demixing is coupled to a transition from a paramagnetic phase ($M = 0$), which is rich in n -particles, to a ferromagnetic phase ($M > 0$) rich in m -particles. The onset of magnetic order is determined by the Curie line (blue line in figure 23), which is obtained by making a Taylor expansion of the Langevin function L [see equation (118) and below] around $M = 0$ combined with the expression for the effective field B [see equation (117)] (note that we consider spatially homogeneous systems here). The resulting critical concentration x_{Curie} as function of the total density is given by

$$x_{\text{Curie}}(\rho, J^*) = \frac{3}{2\pi J^* \rho \sigma^2}. \quad (127)$$

Inspecting the position of the Curie line in the phase diagrams in figure 23, we see that the system is entirely disordered, regardless of the concentration, for values of the total density $\rho \sigma^2 \lesssim 1$ (1.5) for $\delta = 0.1$ (0.06). Increasing the density from these values towards the critical density, the transition from the paramagnetic into the ferromagnetic phase is of second order, until the Curie line meets with the demixing coexistence curve. This merging occurs directly at the demixing critical density (and critical concentration), corresponding to a tricritical point. At densities $\rho > \rho_c$, the Curie line then coincides with the low-concentration branch of the demixing spinodal. This reflects the fact that it is the spin-spin interaction [see equation (100)] which drives the phase separation. Indeed, as can be seen from equation (119), the spin-spin interaction reduces the free energy of the system whenever the magnetization is non-zero.

The demixing spinodal has been calculated using equation (126). Inside the spinodal the mixture is thermodynamically unstable, as indicated by the red areas in figure 23. The black areas in figure 23 indicate the metastable regions between the spinodal and the coexistence curve. The corresponding coexisting densities ρ^I, ρ^{II} and concentrations x^I, x^{II} are calculated using equation (125). Recall that coexisting phases are at equal pressure; we display a number of isobars in the density-concentration plane, which are indicated by the yellow lines in figure 23. For each value of the interaction parameter δ we also display, for one particular exemplary pressure value, a pair of coexisting state points (see circles). From this one may observe that the first-order phase transition is indeed mainly a demixing transition in the sense that the total density change on crossing the transition is small. A comparison of figures 23 (a) and (b) reveals that as δ is reduced, the general topology remains unchanged, but the critical point shifts to larger values of ρ . This is because an increase of the number density of the magnetic component supports the ferromagnetic phase transition [cf. equation (117)]. Finally, we stress that the general topology of the phase diagram does not depend on the precise shape of the interaction pair potentials (as long as the latter are short-ranged) because within our mean-field model, for the bulk fluid with uniform densities, the form of the phase diagram is solely dependent on the integrated strength of the pair potentials; i.e. only the $k = 0$ limit of the Fourier transformed interaction pair potentials influence the phase behavior [cf. equation (120)].

4.2.3. Linear stability of the demixing transition

In the absence of an external potential and under thermodynamically stable conditions [i.e. the system fulfills relations (123)], the stationary solution of equations (144) corresponds to homogeneous number densities, ρ_α^0 . These solutions ρ_α^0 , however, are unstable inside the coexistence region [95; 135; 136; 120; 137]. In the following we aim at describing the onset of this instability. To this end, we investigate the stability against spatiotemporal perturbations up to linear order. Following previous studies [138] we consider small harmonic perturbations where it is assumed that the growth rate $\gamma(k)$ is the same for both species, that is,

$$\begin{aligned}\rho_n(\mathbf{r}, t) &= \rho_n^0 + \Delta\rho(\mathbf{r}, t) = \rho_n^0 + \phi e^{i\mathbf{k}\cdot\mathbf{r}} e^{\gamma(k)t}, \\ \rho_m(\mathbf{r}, t) &= \rho_m^0 + \psi\Delta\rho(\mathbf{r}, t) = \rho_m^0 + \psi\phi e^{i\mathbf{k}\cdot\mathbf{r}} e^{\gamma(k)t}.\end{aligned}\tag{128}$$

Here, $\Delta\rho(\mathbf{r}, t)$ is a small density perturbation where ϕ is the amplitude and $|\mathbf{k}| = k$ is the wave number. We use ψ as the ratio for the perturbation amplitudes between the non-magnetic species and the magnetic species. To describe the dynamics of $\Delta\rho(\mathbf{r}, t)$,

we approximate equations (144) by using a truncated Taylor series expansion of the functional derivatives of the free energy in $\Delta\rho(\mathbf{r}, t)$, that is,

$$\begin{aligned}
& \frac{\delta\mathcal{F}[\rho_n, \rho_m]}{\delta\rho_\alpha} = \frac{\delta\mathcal{F}[\rho_n, \rho_m]}{\delta\rho_\alpha} \Big|_{\rho_n^0, \rho_m^0} \\
& + \int d\mathbf{r}' \frac{\delta^2\mathcal{F}[\rho_n, \rho_m]}{\delta\rho_\alpha\delta\rho_\alpha} \Big|_{\rho_n^0, \rho_m^0} (1 - \delta_{\alpha m}) \Delta\rho(\mathbf{r}', t) \\
& + \psi \int d\mathbf{r}' \left[\frac{\delta^2\mathcal{F}[\rho_n, \rho_m]}{\delta\rho_\alpha\delta\rho_\alpha} \Big|_{\rho_n^0, \rho_m^0} \delta_{\alpha m} \right. \\
& \quad \left. + \frac{\delta^2\mathcal{F}[\rho_n, \rho_m]}{\delta\rho_\alpha\delta\rho_\beta} \Big|_{\rho_n^0, \rho_m^0} (1 - \delta_{\alpha m}) \right] \Delta\rho(\mathbf{r}', t) \\
& + \int d\mathbf{r}' \frac{\delta^2\mathcal{F}[\rho_n, \rho_m]}{\delta\rho_\alpha\delta\rho_\beta} \Big|_{\rho_n^0, \rho_m^0} \delta_{\alpha m} \Delta\rho(\mathbf{r}', t). \quad (\beta \neq \alpha) \tag{129}
\end{aligned}$$

In equation (129), $\delta_{\alpha m}$ is Kronecker's delta representing 1 if $\alpha = m$ and 0 otherwise. Since we are interested in the local stability of an equilibrium solution ρ_α^0 , it is sufficient to truncate the expansion in equation (129) after the linear term. Inserting the resulting terms into equations (144) yields two coupled differential equations representing each species. For the non-magnetic species we obtain

$$\begin{aligned}
\frac{\partial\Delta\rho(\mathbf{r}, t)}{\partial t} &= \Gamma \vec{\nabla} \cdot \vec{\nabla} \left[\Delta\rho(\mathbf{r}, t) \right. \\
& + \rho_n^0 \int d\mathbf{r}' \frac{\delta^2\mathcal{F}_{\text{ex}}[\rho_n, \rho_m]}{\delta\rho_n\delta\rho_n} \Big|_{\rho_n^0, \rho_m^0} \Delta\rho(\mathbf{r}', t) \\
& \left. + \psi \rho_n^0 \int d\mathbf{r}' \frac{\delta^2\mathcal{F}_{\text{ex}}[\rho_n, \rho_m]}{\delta\rho_n\delta\rho_m} \Big|_{\rho_n^0, \rho_m^0} \Delta\rho(\mathbf{r}', t) \right], \tag{130}
\end{aligned}$$

and for the magnetic species,

$$\begin{aligned} \psi \frac{\partial \Delta \rho(\mathbf{r}, t)}{\partial t} &= \Gamma \vec{\nabla} \cdot \vec{\nabla} \left[\psi \Delta \rho(\mathbf{r}, t) \right. \\ &+ \psi \rho_m^0 \int d\mathbf{r}' \left. \frac{\delta^2 \mathcal{F}_{\text{ex}}[\rho_n, \rho_m]}{\delta \rho_m \delta \rho_m} \right|_{\rho_n^0, \rho_m^0} \Delta \rho(\mathbf{r}', t) \\ &+ \rho_m^0 \int d\mathbf{r}' \left. \frac{\delta^2 \mathcal{F}_{\text{ex}}[\rho_n, \rho_m]}{\delta \rho_m \delta \rho_n} \right|_{\rho_n^0, \rho_m^0} \Delta \rho(\mathbf{r}', t) \right], \end{aligned} \quad (131)$$

where $\Gamma = D/(k_B T)$. At this point we introduce the pair direct correlation functions $c_{\alpha\beta}^{(2)}(|\mathbf{r} - \mathbf{r}'|; \rho_n^0, \rho_m^0)$ for the binary mixture, defined as

$$\begin{aligned} k_B T c_{\alpha\beta}^{(2)}(|\mathbf{r} - \mathbf{r}'|; \rho_n^0, \rho_m^0) &= k_B T c_{\alpha\beta}^{(2)}(\mathbf{r}, \mathbf{r}') \\ &= - \frac{\delta^2 \mathcal{F}_{\text{ex}}}{\delta \rho_\alpha(\mathbf{r}') \delta \rho_\beta(\mathbf{r})}. \end{aligned} \quad (132)$$

It is then helpful to perform a Fourier transform with respect to the position coordinates. Since we are expanding around a homogeneous state, the correlation functions $c_{\alpha\beta}^{(2)}(k; \rho_n^0, \rho_m^0)$ depend only on the magnitude of k , and the same is assumed to be true for the function $\gamma(k)$. This yields equations (130) and (131) in momentum space

$$\begin{aligned} \gamma(k) \Delta \rho(\mathbf{k}, t) &= -k^2 \Gamma \Delta \rho(\mathbf{k}, t) \left[1 - \rho_n^0 c_{nn}^{(2)}(k; \rho_n^0, \rho_m^0) \right. \\ &\quad \left. - \psi \rho_n^0 c_{nm}^{(2)}(k; \rho_n^0, \rho_m^0) \right] \\ \psi \gamma(k) \Delta \rho(\mathbf{k}, t) &= -k^2 \Gamma \Delta \rho(\mathbf{k}, t) \left[\psi - \psi \rho_m^0 c_{mm}^{(2)}(k; \rho_n^0, \rho_m^0) \right. \\ &\quad \left. - \rho_m^0 c_{mn}^{(2)}(k; \rho_n^0, \rho_m^0) \right]. \end{aligned} \quad (133)$$

We search for the solution $\gamma(k)$, which satisfies equations (133) simultaneously. To this end, we rewrite both equations in a matrix representation, that is,

$$\gamma(k) \begin{pmatrix} 1 \\ \psi \end{pmatrix} = \underline{\underline{M}} \cdot \underline{\underline{G}} \begin{pmatrix} 1 \\ \psi \end{pmatrix}. \quad (134)$$

Here, the matrices $\underline{\underline{M}}$ and $\underline{\underline{G}}$ are of dimension 2×2 . It follows that

$$\underline{\underline{M}} = \begin{pmatrix} -k^2\Gamma & 0 \\ 0 & -k^2\Gamma \end{pmatrix}, \quad (135)$$

$$\underline{\underline{G}} = \begin{pmatrix} 1 - c_{nm}^{(2)}\rho_n^0 & -c_{nm}^{(2)}\rho_n^0 \\ -c_{mn}^{(2)}\rho_m^0 & 1 - c_{mm}^{(2)}\rho_m^0 \end{pmatrix}. \quad (136)$$

Since $\underline{\underline{M}}$ is diagonal and all diagonal elements are non-zero, the inverse $\underline{\underline{M}}^{-1}$ exists and the solution of equations (134)-(136) reads

$$\begin{aligned} \gamma(k) &= \frac{\text{Tr}(\underline{\underline{M}} \cdot \underline{\underline{G}})}{2} \pm \sqrt{\frac{\text{Tr}(\underline{\underline{M}} \cdot \underline{\underline{G}})^2}{4} - \det(\underline{\underline{M}} \cdot \underline{\underline{G}})} \\ &= \frac{k^2\Gamma^2}{2} (c_{mm}^{(2)}\rho_m^0 + c_{nn}^{(2)}\rho_n^0 - 2) \\ &\quad \pm \frac{k^2\Gamma^2}{2} \left[(c_{nn}^{(2)})^2 (\rho_n^0)^2 + (c_{mm}^{(2)})^2 (\rho_m^0)^2 \right. \\ &\quad \left. + 4c_{nm}^{(2)}\rho_n^0 c_{mn}^{(2)}\rho_m^0 - 2c_{mm}^{(2)}\rho_m^0 c_{nn}^{(2)}\rho_n^0 \right]^{\frac{1}{2}}. \end{aligned} \quad (137)$$

Our ansatz in equation (128) shows that, for positive values of $\gamma(k)$, the density perturbation $\Delta\rho$ with wave number k grows exponentially in time. Therefore, we search for the region $k_< < k^* < k_>$ where $\gamma(k^*) > 0$. Since $\gamma(k_<) = \gamma(k_>) = 0$, the wave numbers $k_<$ and $k_>$ mark the transition points where the homogeneous fluid is linearly unstable ($\gamma(k) > 0$) or linearly stable ($\gamma(k) < 0$).

We now discuss the linear stability against spatiotemporal perturbations based on numerical solution of equation (137). Specifically, we choose a number density of $\rho\sigma^2 = 3.2$ as it is known that the mean-field approximation is particularly accurate at high densities, i.e., in situations where the average number of next neighbors is large for each particle [93; 34]. We focus on concentrations x inside the unstable region of the phase diagram [see figure 23(a)]. For all concentrations x considered the growth rate is $\gamma \approx 0$ for $k \rightarrow 0$ (corresponding to large wave lengths $\lambda = 2\pi/k$) as can be seen in figure 24(a). For concentrations $0.42 < x < 0.86$, we find solutions $\gamma > 0$ for $k \neq 0$ and $k < k_>$ where the critical wavenumber $k_>$ depends on the concentration x . All γ -curves exhibit local maxima (e.g., $k_{\max}\sigma \approx 0.42$ for $x = 0.6$), i.e. density perturbations with wave number k_{\max} are expected to grow the fastest. By increasing the wave number further such that $k \geq k_>(x)$, the growth rate becomes negative for all k .

We note that the predictions from linear stability analysis become inconsistent with

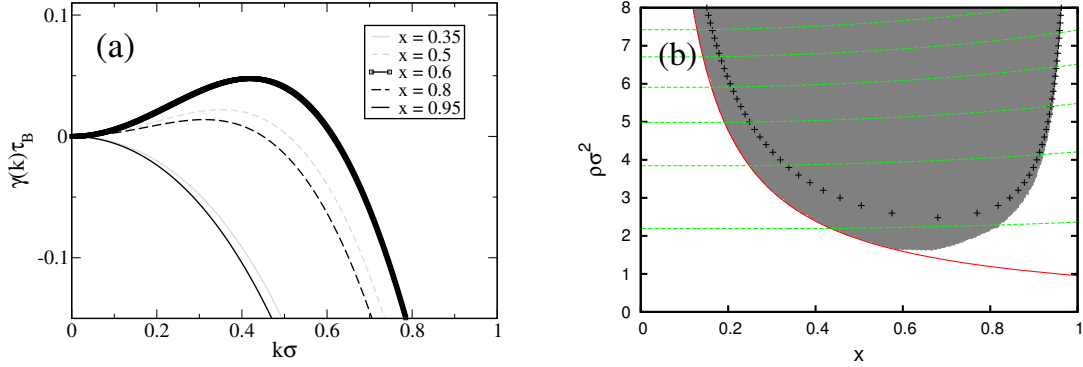


Figure 24.: (a) shows results for the growth rate $\gamma(k)$ obtained from equation (137) at density $\rho\sigma^2 = 3.2$ at different concentrations within the meta- and unstable part of the phase diagram. (b) shows the unstable region of the phase diagram. The black crosses mark the crossover region where solutions $\gamma(k) > 0$ can be found within the linear analysis. The green lines are isobars with a line-to-line pressure difference of $\Delta P^* = 80$ (where the lowest curve is for $P^* = 40$). The Curie line is indicated by the red curve. The parameters are $\varepsilon^* = 5$ and $J^* = 0.5$.

the phase diagram near the spinodal [boundary of the grey area in figure 24(b)]. This becomes clear, when we calculate the region where we find critical wavenumbers $k_{>}(x)|_{\rho} \neq 0$ for different number densities ρ . The black crosses in figure 24(b) mark the crossover region where $k_{>}(x)|_{\rho} \rightarrow 0$, i.e. outside this region the linear stability analysis predicts that spinodal decomposition does not occur. However, from figure 24(b) we see that this region is always *inside* the spinodal; thus, the size of the unstable region is underestimated. Only for higher densities the black crosses seem to approach the spinodal (we checked values up to $\rho\sigma^2 = 12$).

The fact that the linear analysis becomes wrong close to the spinodal is also confirmed by our numerical solution of the full DDFT equations (including the nonlinear terms): These numerical calculations reveal spontaneous demixing to occur even close to the spinodal. A similar conclusion regarding the performance of a linear analysis close to the spinodal was reported in a study [139] based on the nonlinear Smoluchowski equation (which is closely related to DDFT, see reference [95]). There, it was argued that terms linear in $\Delta\rho$, which are related to the absolute stability conditions of the system and are therefore proportional to inverse susceptibilities, become small upon approach of the spinodal. Thus, the terms linear in $\Delta\rho$ are no longer dominant near the spinodal and nonlinear terms have to be taken into account. A further reason for the observed inconsistency between our linear stability analysis and the full DDFT

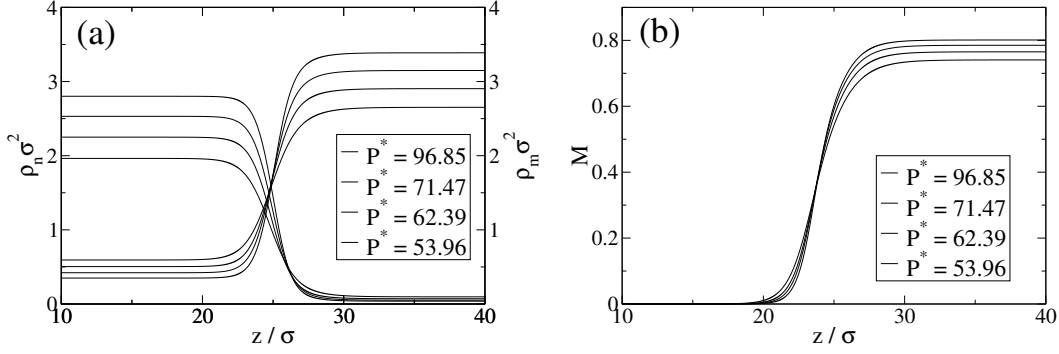


Figure 25.: (a) The density profiles of the two demixed phases and (b) the magnetization profile (species m) at the interface for different values of P^* . The coupling parameters are $\varepsilon^* = 5.0$ and $\delta = 0.1$.

calculations may be the approximate character of the direct correlation functions entering our theory. In fact, similar inconsistencies occur in the context of equilibrium properties [92], although we should note that, at least for the pure GCM fluid, these inconsistencies are typically small [93].

4.2.4. Interfacial structure

In sections 4.2.2 and 4.2.3 we showed that the magnetic mixture displays a first-order demixing phase transition for a broad range of densities ρ and concentrations x . In this section, we focus on the structure of the fluid-fluid interface between the two demixed phases for densities above ρ_c . The grand canonical free energy Ω for the non-uniform binary mixture is given by equation (106). Setting the external potential $V_{\text{ext}} = 0$ yields a well-defined (one-dimensional) interface between one region enriched with particles from the non-magnetic species and a second region enriched with magnetic particles. Setting the functional derivative of equation (106) to zero yields the Euler-Lagrange equations for the chemical potential of species n

$$\mu_n = k_B T \ln [\rho_n(z)] + \int d\mathbf{r}' [\rho_n(z') + \rho_m(z')] V_{\text{core}}(|\mathbf{r} - \mathbf{r}'|), \quad (138)$$

and species m , respectively,

$$\begin{aligned}
\mu_m = k_B T & \left\{ \ln [\rho_m(z)] + B(z) \coth [B(z)] - 1 \right. \\
& \left. + \ln \left[\frac{B(z')}{\sinh [B(z')]} \right] \right\} \\
& + \int d\mathbf{r}' [\rho_n(z') + \rho_m(z')] \beta V_{\text{core}}(|\mathbf{r} - \mathbf{r}'|) \\
& + L[B(z)] \int d\mathbf{r}' L[B(z')] \rho_m(z') \beta J(|\mathbf{r} - \mathbf{r}'|), \tag{139}
\end{aligned}$$

where $\beta = 1/(k_B T)$. Using the (bulk) coexisting densities $\rho_n^{\text{bulk}} = \rho_n^{\text{I}}$, $\rho_m^{\text{bulk}} = \rho_m^{\text{II}}$ found from the calculation of the binodal in section 4.2.2, the chemical potentials μ_n and μ_m can be eliminated from equations (138) and (139). This leads to the equations for the one-body density profiles across the free interface. Specifically, we obtain for the non-magnetic component

$$\begin{aligned}
\rho_n(z) = \rho_n^{\text{bulk}} \\
\times \exp \left[\sum_{\alpha=n}^m \int d\mathbf{r}' (\rho_\alpha^{\text{bulk}} - \rho_\alpha(z')) \beta V_{\text{core}}(|\mathbf{r} - \mathbf{r}'|) \right], \tag{140}
\end{aligned}$$

and for the magnetic component

$$\begin{aligned}
\rho_m(z) = \rho_m^{\text{bulk}} \exp & \left[\sum_{\alpha=n}^m \int d\mathbf{r}' (\rho_\alpha^{\text{bulk}} - \rho_\alpha(z')) \beta V_{\text{core}}(|\mathbf{r} - \mathbf{r}'|) \right. \\
& + L(B^{\text{bulk}})^2 \int d\mathbf{r}' (\rho_m^{\text{bulk}} - \rho_m(z')) \beta J(|\mathbf{r} - \mathbf{r}'|) \\
& + \frac{B^{\text{bulk}}}{\sinh(B^{\text{bulk}})} - \frac{B(z')}{\sinh[B(z')]} + B^{\text{bulk}} L^{\text{bulk}} - B(z') L(z') \\
& \left. - L[B(z)] \int d\mathbf{r}' L[B(z')] (\rho_m^{\text{bulk}} - \rho_m(z')) \beta J(|\mathbf{r} - \mathbf{r}'|) \right]. \tag{141}
\end{aligned}$$

Equations (140) and (141) can be solved self-consistently. The results for the density profiles and the magnetization are shown in figure 25 for a fixed magnetic coupling parameter $\delta = 0.1$ [see figure 23(a) for the corresponding phase diagram]. The decay of the density profiles into the two bulk phases in figure 25 is monotonic. In previous studies of binary mixtures of soft particles [34; 140] and also of colloid-polymer mixtures

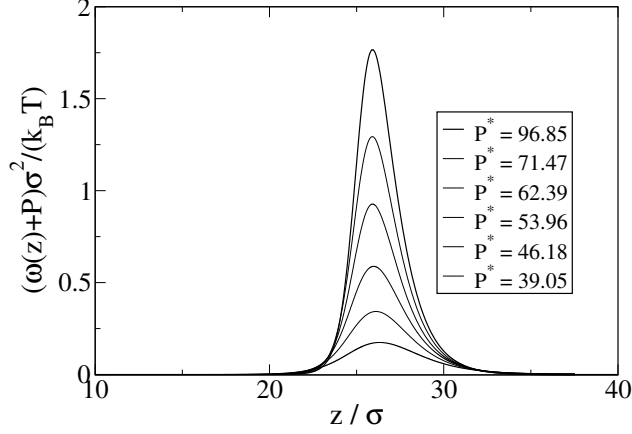


Figure 26.: The grand potential density as function of z with the interface being located at $z = 25.6\sigma$. The coupling parameters are $\varepsilon^* = 5.0$ and $\delta = 0.1$.

[141; 142] it was found that non-monotonic oscillatory decay of the density profiles can occur for the free interface between coexisting state points that are sufficiently far removed in the phase diagram from the critical point. We expect a similar scenario for the present system as that observed in the systems studied in references [34; 140], i.e. we expect to observe oscillatory behavior in the density profiles also for the present system, but for higher values of the total bulk density, i.e. further away from the critical point. Note that the freezing transition [117] of the pure GCM fluid in three dimensions occurs only at much lower temperatures (i.e. much larger values of ε^*) than we consider here. Indeed, the corresponding freezing temperature of the GCM in three dimensions is $t_u = k_B T / \varepsilon_u \approx 0.008$, i.e. $\varepsilon_u / (k_B T) \approx 125$. At $\varepsilon^* = 5$, the system therefore remains fluid at all densities [143].

Approaching the critical density from above, the interface softens, resulting in a reduced pressure parallel to the interface. Physically, this softening is reflected by a decreasing line tension (in 2D). To calculate the line tension we assume that the dividing surface is a line that is orientated along the x -direction. The pressure tensor \mathbf{P} is a (2×2) -matrix characterized by one component parallel to the interface (P_T) and one component normal to the interface (P_N), that is

$$\mathbf{P} = P_T(z)\hat{e}_x\hat{e}_x + P_N(z)\hat{e}_z\hat{e}_z. \quad (142)$$

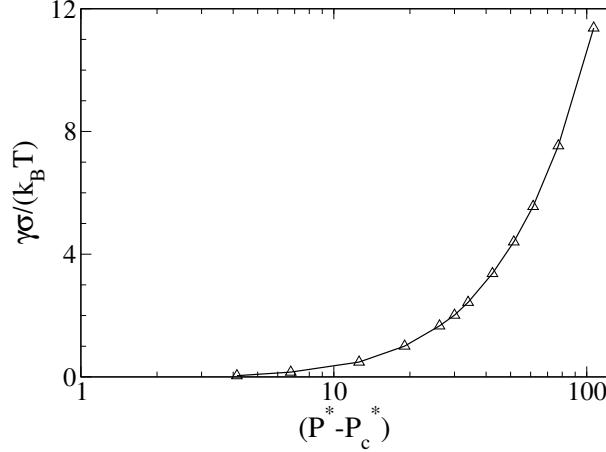


Figure 27.: *The interfacial (line) tension $\gamma^* = \gamma\sigma/(k_B T)$ between the demixed phases as function of the pressure difference relative to the critical point. The coupling parameters are $\varepsilon^* = 5.0$, $\delta = 0.1$.*

Here, \hat{e}_x and \hat{e}_z are normalized unit vectors in the x -direction and z -direction, respectively. In equilibrium, the normal pressure $P_N(z)$ is constant and equals the bulk pressure P at coexistence. Furthermore, the tangential component P_T only depends on z . The interfacial (line) tension γ is then defined as the excess force resulting from the dividing interface [144; 145], that is,

$$\gamma = \int_{-\infty}^{\infty} dz (P - P_T(z)). \quad (143)$$

To actually calculate $P_T(z)$, we use the relation [144] $P_T(z) = -\omega(z)$, where $\omega(z)$ is defined as the grand canonical free energy per unit length calculated in the absence of an external potential. Numerical results for the function $(\omega(z) + P)$ [i.e., the integrand in equation (143)] at various total densities $\rho\sigma^2$ are shown in figure 26. We only find non-vanishing values of the function $(\omega(z) + P)$ near the interface. This reflects the simple fact that the interfacial tension stems from the density inhomogeneities at the interface. From figure 25 we see that the density profiles become smoother as the critical point is approached. This behavior is mirrored by the function $(\omega(z) + P)$ (see figure 26), resulting in a vanishing interfacial tension at the critical point. The

behavior of γ as a function of the pressure difference ($P - P_c$) is displayed in figure 27.

4.3. Demixing dynamics

We now turn to discuss the dynamics of phase separation in the present system. To this end, we employ the DDFT approach from section 2.2.3 in which the time evolution of the one-particle densities are governed by a generalized continuity equation.

For the present system, where one species (the m -particles) has internal degrees of freedom, one should employ the DDFT equations for anisotropic particles recently proposed in reference [146], which shows that the equations of motion for the position- and angle-dependent densities involve both the usual translational currents $\mathbf{j}_\alpha = -D_\alpha \rho_\alpha \nabla \delta \mathcal{F} / \delta \rho_\alpha$, and also ‘rotational current’ terms resulting from application of the angular momentum operator to the thermodynamic driving force $\delta \mathcal{F} / \delta \rho_m$. However, the numerical solution of the resulting set of equations of motions for the demixing problems that we consider here (see below) involve simultaneously determining not only the two-dimensional (isotropic) number density profiles of the n - and m -particles, respectively, but also of the orientational distribution function $h_m(\mathbf{r}, \omega, t)$. The angle-dependence of the latter induces additional dimensions making the numerical calculations rather involved.

In the present study, we somewhat simplify the problem by assuming that the magnetic degrees of freedom are at each moment in time in equilibrium with the density profiles. Physically, this assumption implies that the relaxation time of the magnetic moments is much shorter than that of the translational degrees of freedom. We are aware that this assumption certainly oversimplifies the physical behavior expected in a real magnetic/non-magnetic mixture. Indeed, in a recent DDFT study it was shown that the relaxation dynamics of an anisotropic fluid is characterized by a nontrivial interplay between rotational and translational degrees of freedom if the rotational degrees of freedom do not relax faster in comparison with the translational ones (see figures 7 and 8 in reference [146]). However, in that study, the interplay between rotations and translations is induced by time dependent external fields that couple directly to the alignment vector of the particles. One may argue that the rotational degrees of freedom are strongly out of equilibrium due to the time-dependent field in this case. In our model, however, the anisotropic particles are for all times preferentially orientated in one direction without any external fields coupling to the particles. Given our assumption that the magnetic moment relaxation time is short compared to the translational (density) relaxation time scale, this argument implies that the functional derivative $\delta \mathcal{F} / \delta h(\mathbf{r}, \omega, t) = 0$ at all times t , i.e., there is no driving torque. Under these

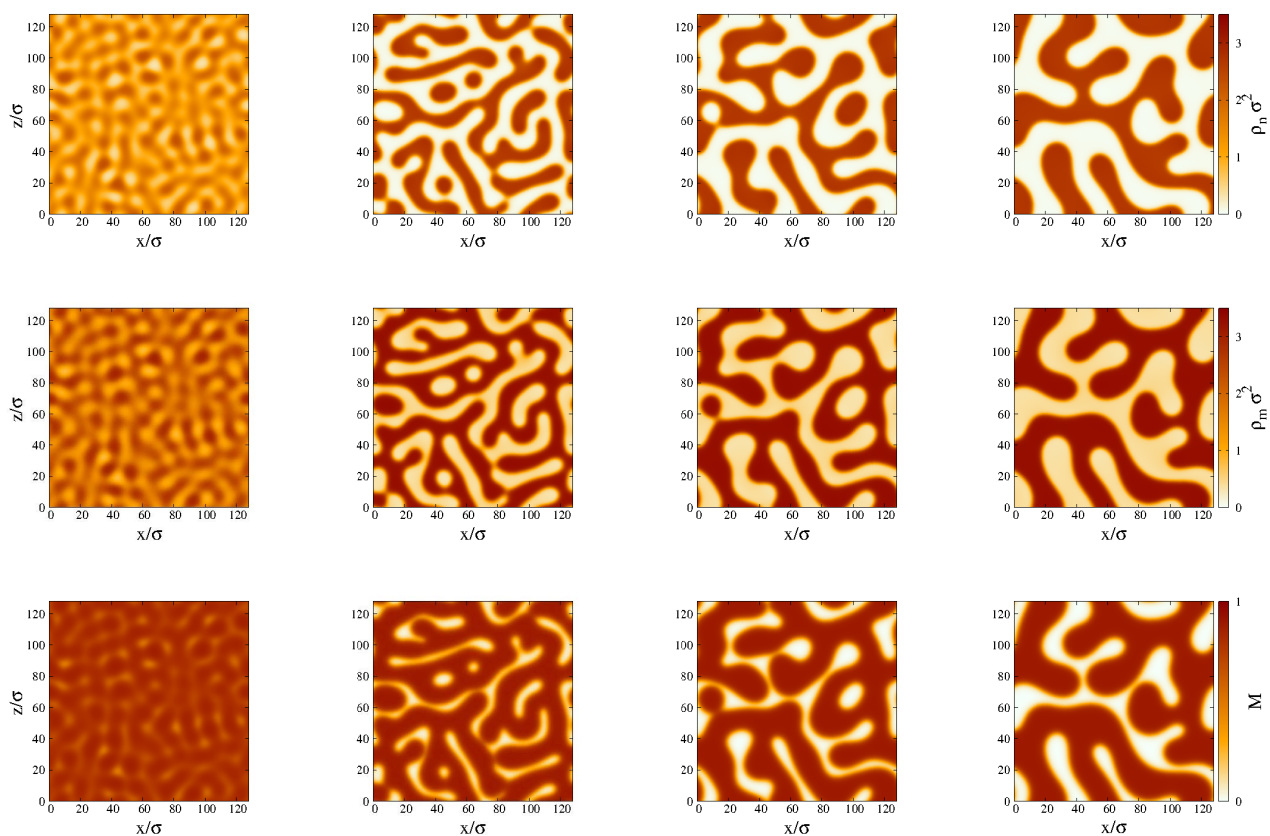


Figure 28.: Density profiles of the isotropic particles (upper row), magnetic particles (middle row) and the magnetization (bottom row) as a function of the position. The time increases from the left to the right: $t_1 = 60\tau_B$, $t_2 = 200\tau_B$, $t_3 = 400\tau_B$ and $t_4 = 800\tau_B$. The parameters are $\rho\sigma^2 = 3.2$, $x = 0.6$, $\varepsilon^* = 5.0$ and $\delta = 0.1$.

conditions, the DDFT equations for the present system reduce to a coupled set of equations for the number density profiles of the n - and m -particles (cf. section 2.2.3)

$$\Gamma_\alpha^{-1} \frac{\partial \rho_\alpha(\mathbf{r}, t)}{\partial t} = \nabla \cdot \left[\rho_\alpha(\mathbf{r}, t) \nabla \frac{\delta \mathcal{F}[\rho_n(\mathbf{r}, t), \rho_m(\mathbf{r}, t)]}{\delta \rho_\alpha(\mathbf{r}, t)} \right], \quad (144)$$

combined with the self-consistency relation

$$h_B(\mathbf{r}, \omega, t) = \frac{\exp(\mathbf{B}(\mathbf{r}, t) \cdot \mathbf{s}(\omega, t))}{\int d\omega \exp(\mathbf{B}(\mathbf{r}, t) \cdot \mathbf{s}(\omega, t))}, \quad (145)$$

where the time-dependent effective field $\mathbf{B}(\mathbf{r}, t)$ is given by equation (117) and where \mathcal{F} is the MF Helmholtz free energy functional developed in section 4.2.1. The mobility coefficients Γ_α in equation (144) are related to the diffusion constants via $\Gamma_\alpha = D_\alpha/(k_B T)$, where $\alpha = n$ or m . In what follows we assume that these are equal: $\Gamma_n = \Gamma_m = \Gamma$.

When the external potential $V_{\text{ext}} = 0$, the uniform density distributions, $\rho_\alpha(\mathbf{r}, t) = \rho_\alpha^{\text{bulk}}$, always correspond to a stationary solution of the DDFT equation (144), since in this case the functional derivatives $\delta \mathcal{F}/\delta \rho_\alpha$ are constants. However, if one considers applying small harmonic perturbations to the uniform densities $\rho_\alpha(\mathbf{r}, t) = \rho_\alpha^{\text{bulk}} + \delta \rho_\alpha(\mathbf{r}, t)$, where $\delta \rho_\alpha(\mathbf{r}, t) \sim \sin(\mathbf{k} \cdot \mathbf{r})$, with wave number $|\mathbf{k}| = k$, and where $\delta \rho_\alpha \sigma^2 \ll 1$, then one finds that inside the spinodal region (the red region in figure 23) density fluctuations with certain wavenumbers k grow with time (see section 4.2.3) – i.e. within the spinodal the fluid is linearly unstable. Outside the spinodal, the system is linearly stable, i.e. the amplitude of any small amplitude density fluctuations decrease over time. In the region between the binodal and the spinodal (the black regions in figure 23), the fluid is linearly stable, but is not absolutely stable: if the amplitude of a given density perturbation is large enough, then the amplitude of this density fluctuation will grow over time. This is due to the non-linear terms in equation (144). For densities outside of the binodal, the uniform fluid is absolutely stable and all density modulations diminish in amplitude over time. The above description of the system is therefore qualitatively very similar to the results from Cahn-Hilliard theory [147].

Thus, there are two phase separation mechanisms: Firstly, spinodal demixing, which is triggered by the presence of small amplitude density modulations, which in reality are always present due to thermal fluctuations. This is the dominant mechanism inside the spinodal. Secondly, for state points in the region between the spinodal and the binodals, where the uniform fluid is linearly stable, phase separation must proceed via the nucleation of density fluctuations with sufficiently large amplitude. We present

results pertaining to these two mechanisms below.

4.3.1. Spinodal demixing

To study the phase separation dynamics in the spinodal region, we set the time $t = 0$ density profiles to be $\rho_\alpha(\mathbf{r}, t = 0) = \rho_\alpha^{\text{bulk}} + \chi(\mathbf{r})$, where $\chi(\mathbf{r})$ is a small amplitude random white noise field, which is equivalent to adding many harmonic density perturbations, with randomly chosen amplitude, phase and wavenumbers k . The density and magnetization profiles are then evolved forward in time using equations (144) and (145). Note that we only add noise to the initial $t = 0$ density profiles and do not add noise at any other subsequent time. This corresponds to taking an uniform system and then rapidly quenching it into the unstable region of the phase diagram, by decreasing the temperature. Inside the spinodal, the density perturbations with wave numbers $0 < k < k_c$ grow over time (see section 4.2.3). The density modulations with wavenumber $k \approx k_*$, where $0 < k_* < k_c$, grows fastest in amplitude over time, leading to density profiles having density modulations with a typical length scale $\approx 2\pi/k_*$, at short times after the quench. As is illustrated by the results displayed in figure 28, the domains of demixed fluid then coarsen over time. Since in the present system this demixing is between a magnetic and a non-magnetic phase, we also observe a similar pattern in the local magnetization; see the bottom row in figure 28. The results in this figure are for a fluid with total density $\rho\sigma^2 = 3.2$, concentration $x = 0.6$ and with $\varepsilon^* = 5.0$ and $\delta = 0.1$. The phase diagram for this system is displayed in figure 23. For a given total density ρ within the spinodal region, on varying the concentration x one may observe bicontinuous labyrinthine patterns, such as those displayed in figure 28, or alternatively one observes phase separated morphologies consisting of ‘islands’ of the minority phase surrounded by a ‘sea’ of the majority phase. A more detailed discussion of this phenomenon follows in section 4.5.

4.3.2. Dynamical test particle theory

We now turn to the calculation of dynamical correlation functions. To this end we recall that, within the static DFT, there are two routes towards the calculation of the partial pair correlation functions for the homogeneous fluid [148]: the first one is the integral equation theory [149; 92] based on the Ornstein-Zernike equation supplemented by an appropriate closure relation. The second one is the test particle method [81], where one particle of a given species is fixed at the origin and the partial pair correlation functions can be obtained from the one-body density profiles of the resulting inhomogeneous fluid [148]. Here, we employ the dynamical extension [82; 83]

of the latter method, where the test particle is allowed to move away from the origin where it was at $t = 0$.

To begin with, we define the relevant spatiotemporal correlation functions for the present system (cf. section 2.3.3 for the monatomic fluid). The probability of finding a particle of species α at time t at position \mathbf{r} , given that one particle of species β was at the origin at time $t = 0$, is characterized by the van Hove functions $G_{\alpha\beta}(\mathbf{r}, t)$. Similar as for monodisperse suspensions, $G_{\alpha\beta}$ for a binary mixture can be decomposed into its respective “self” and “distinct” parts: [82; 92]

$$G_{\alpha\beta}(\mathbf{r}, t) = G_{\alpha\beta}^s(\mathbf{r}, t) + G_{\alpha\beta}^d(\mathbf{r}, t), \quad (146)$$

where

$$\begin{aligned} G_{\alpha\beta}^s(\mathbf{r}, t) &= \frac{\delta_{\alpha\beta}}{N_\alpha} \left\langle \sum_{i=1}^{N_\alpha} \delta(\mathbf{r} - \mathbf{r}_i^\alpha(t) + \mathbf{r}_i^\alpha(0)) \right\rangle, \\ G_{\alpha\beta}^d(\mathbf{r}, t) &= \frac{1 - \delta_{\alpha\beta}}{\sqrt{N_\alpha N_\beta}} \left\langle \sum_{i=1}^{N_\alpha} \sum_{j \neq i}^{N_\beta} \delta(\mathbf{r} - \mathbf{r}_i^\alpha(t) + \mathbf{r}_j^\beta(0)) \right\rangle \\ &\quad + \delta_{\alpha\beta} \frac{1}{N_\alpha} \left\langle \sum_{i=1}^{N_\alpha} \sum_{j \neq i}^{N_\alpha} \delta(\mathbf{r} - \mathbf{r}_i^\alpha(t) + \mathbf{r}_j^\alpha(0)) \right\rangle, \end{aligned} \quad (147)$$

with $\delta_{\alpha\beta}$ being Kronecker’s delta. Further, $N = N_\alpha + N_\beta$ is the total number of particles in the system. At time $t = 0$ these functions fulfill the initial conditions

$$\begin{aligned} G_{\alpha\beta}^s(\mathbf{r}, t = 0) &= \delta_{\alpha\beta} \delta(\mathbf{r}), \\ G_{\alpha\beta}^d(\mathbf{r}, t = 0) &= \rho_\alpha^{\text{bulk}} g_{\alpha\beta}(\mathbf{r}), \end{aligned} \quad (148)$$

where $g_{\alpha\beta}(\mathbf{r})$ denotes the partial (static) pair distribution functions.

As explained in section 2.3, one can find the equilibrium structure of a fluid from Percus’ test particle limit [81]. In order to obtain the time-dependent (off-equilibrium) van Hove functions $G_{\alpha\beta}(\mathbf{r}, t)$, we carry out the identification scheme together with Percus’ test particle route as suggested by references [82; 83]. The dynamics of the conditional profiles is in the case of the magnetic mixture given by the DDFT equations of a *four-component* fluid mixture, where both of the original components ($\alpha = \{m, n\}$)

are decomposed into a self part (s) and a distinct part (d),

$$\frac{\partial \rho_\alpha^i(\mathbf{r}, t)}{\partial t} = D \nabla \cdot \left[\rho_\alpha^i(\mathbf{r}, t) \nabla \frac{\delta \mathcal{F}[\{\rho_\alpha^i(\mathbf{r}, t)\}]}{\delta \rho_\alpha^i(\mathbf{r}, t)} \right], \quad i = \{s, d\}. \quad (149)$$

The self part refers to a single particle and the distinct part to the remaining $N_\alpha - 1$ particles. Further, the free energy functional entering equations (149) is given as $\mathcal{F} = \mathcal{F}_{\text{id}} + \mathcal{F}_{\text{ex}}$ where we have (as a generalization of the conventional mixture)

$$\begin{aligned} \mathcal{F}_{\text{id}}[\{\rho_\alpha^i\}] &= k_B T \sum_i^{\{s,d\}} \sum_\alpha^{\{m,n\}} \int d\mathbf{r} \int d\omega \rho_\alpha^i(\mathbf{r}, \omega, t) \\ &\quad \times [\ln(\rho_\alpha^i(\mathbf{r}, \omega, t) \Lambda_\alpha^2) - 1], \\ \mathcal{F}_{\text{ex}}[\{\rho_\alpha^i\}] &= \frac{1}{4} \sum_{i,j}^{\{s,d\}} \sum_{\alpha,\beta}^{\{m,n\}} \int d\mathbf{r} \int d\mathbf{r}' \int d\omega \int d\omega' \rho_\alpha^i(\mathbf{r}, \omega, t) \\ &\quad \times V_{\alpha\beta}^{ij}(|\mathbf{r} - \mathbf{r}'|, \omega, \omega') \rho_\beta^j(\mathbf{r}', \omega', t). \end{aligned} \quad (150)$$

The interactions $V_{\alpha\beta}^{ij}$ entering equations (150) are determined by the pair potentials $V_{\alpha\beta}$ as defined in equation (100-101). Specifically, we set $V_{\alpha\beta}^{dd} = V_{\alpha\beta}^{sd} = V_{\alpha\beta}$ where

$$\begin{aligned} V_{nn} &= V_{mn} = V_{nm} = V^{\text{core}}(|\mathbf{r} - \mathbf{r}'|), \\ V_{mm} &= V^{\text{core}}(|\mathbf{r} - \mathbf{r}'|) + J(|\mathbf{r} - \mathbf{r}'|) \mathbf{s} \cdot \mathbf{s}'. \end{aligned} \quad (151)$$

Moreover, to take into account the fact that there is only one test particle in the system, we set $V_{\alpha\beta}^{ss} = 0$ for all α, β where $V_{\alpha\alpha}^{ss} = 0$ takes the absence of self-interactions into account. The self-consistent solution for the effective field is given by

$$\begin{aligned} \mathbf{B}(\mathbf{r}, t) &= - \int d\mathbf{r}' \int d\omega' [\rho_m^s(\mathbf{r}', t) + \rho_m^d(\mathbf{r}', t)] \\ &\quad \times h_m(\mathbf{r}', \omega', t) J(|\mathbf{r} - \mathbf{r}'|) \mathbf{s}'. \end{aligned} \quad (152)$$

In order to suffice the initial conditions given by equations (148) we evolve the one-body profiles $\rho_\alpha^i(\mathbf{r}, t)$ via equations (144) [together with equations (117-119)] while holding the position of the test particle fixed. This ‘‘relaxation’’ procedure yields the static pair correlation functions. After this initial preparation we release the test particle and evolve the one-body profiles forward in time which gives the time-dependent van

Hove correlation functions via the identification scheme

$$G_{\alpha\beta}^s(\mathbf{r}, t) = \rho_\beta^s(\mathbf{r}, t), \quad \text{and} \quad G_{\alpha\beta}^d(\mathbf{r}, t) = \rho_\alpha^d(\mathbf{r}, t). \quad (153)$$

Note that we consider a single test particle of species α surrounded by the remaining fluid, i.e. we set $\rho_\beta^s(\mathbf{r}, \omega, t) = 0$ (with $\beta \neq \alpha$) for all times t . This reduces equations (149) to three coupled equations. Furthermore, we note that in contrast to equation (117) the effective field in equation (152) is given by the “full” (magnetic) van Hove function $G_{m\alpha}(\mathbf{r}, t)$ where α is a test particle either from the magnetic or from the non-magnetic species. This result can be obtained by using for $G_{m\alpha}^s(\mathbf{r}, t)$ and $G_{m\alpha}^d(\mathbf{r}, t)$ the same ansatz equation (145) for the orientational distribution function, i.e. we set $h_m^s(\mathbf{r}, \omega, t) = h_m^d(\mathbf{r}, \omega, t)$. Minimizing then equation (150) with respect to the effective field $B(\mathbf{r}, t)$ yields equation (152).

4.4. Spinodal decomposition kinetics

An important point related to pattern formation is the dynamics of disordered systems undergoing phase separation. Results from theories, simulations and experiments indicate that phase separation processes show common characteristics at late stages [150]. Indeed, *at late stages* the coarsening often follows a power law behavior for the characteristic length of the system, that is, $l(t) \propto t^\alpha$. The exponent α depends strongly on the nature of the variables that drive the phase separation; e.g., for diffusive systems with a scalar conserved (non-conserved) order parameter the exponent for the corresponding kinetic universality class is $\alpha = 1/3$ ($\alpha = 1/2$). However, also exponents differing from these “classical” scaling laws have been reported recently such as in studies concerning active Brownian particles where the exponent seems to be smaller than $1/3$ [151]. For molecular fluids the diffusive coarsening regime may be skipped over in favor of viscous hydrodynamic growth characterized by linear growth in time [152; 40]. It is this complexity that makes the precise understanding of the underlying phase separation mechanisms important.

For a fluid undergoing spinodal decomposition three different time regimes have to be distinguished [150]. At early times the density fluctuations are small. Thus, on a theoretical description level one may consider the terms linear in the density fluctuation, such as in the Cahn-Hilliard theory [153; 147; 154]. For intermediate times the interfacial width ξ plays an important role, but sharp interfaces have not been fully formed yet. This does not happen until the late stages of the domain coarsening, where the ratio $\xi/l(t)$ becomes negligible small [150].

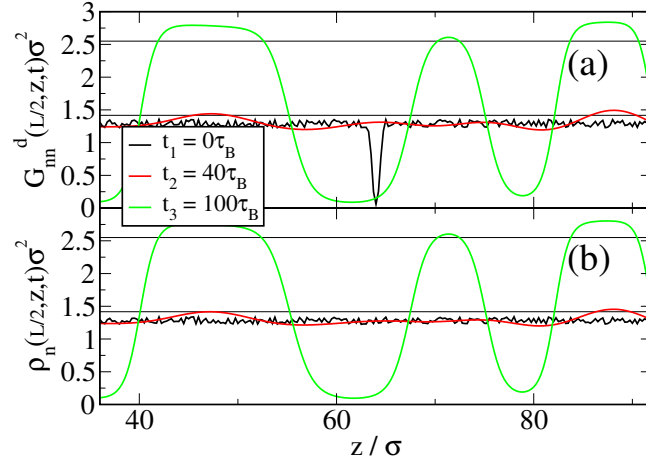


Figure 29.: Time series for the phase separating system for a slice through $x = L/2$ (where $L = 128\sigma$). The times are $t_1 = 0\tau_B$, $t_2 = 40\tau_B$ and $t_3 = 100\tau_B$. (a) shows the distinct part of the van Hove function for the non-magnetic species, where a non-magnetic test particle has been placed at position $x = z = 64\sigma$ at time $t_1 = 0\tau_B$ leading to a correlation hole at the same position (see black curve). (b) shows the one-body density as a function of z -position for the same species. The black horizontal lines [plotted at the same values in (a) and (b)] are a guide to the eye. The coupling parameters are $\varepsilon^* = 5.0$, $J^* = 0.5$.

In the present system the demixing transition is coupled to the spatiotemporal changes of the one-body profiles $\rho_\alpha(\mathbf{r}, t)$, which are conserved quantities, i.e., the particle numbers

$$N_n = \int d\mathbf{r} \rho_n(\mathbf{r}, t), \quad N_m = \int d\mathbf{r} \rho_m(\mathbf{r}, t), \quad (154)$$

are constant for all times t . This is a general feature of the DDFT method. We stress that the magnetization profile $m(\mathbf{r}, t)$ is coupled to the corresponding one-body profile $\rho_m(\mathbf{r}, t)$ at any time instant [see equation (117)]. Thus, the cluster growth behavior should be determined mainly by the conserved order parameters $\rho_m(\mathbf{r}, t)$ and $\rho_n(\mathbf{r}, t)$. In the following, we aim for a more detailed study of the demixing kinetics within our system focusing on the time-dependent average cluster size $l_\alpha(t)$.

4.4.1. Correlation functions

Our main target quantities are the van Hove correlation functions $G_{\alpha\beta}(\mathbf{r}, t)$, from which the average domain sizes $l_\alpha(t)$ can be calculated quite straightforwardly [see equation (156) below]. To illustrate the time-dependence of these functions we place exemplarily a non-magnetic test particle at position $x = z = L/2$ (centre position of the system) at time $t = 0$. We note that we approximate the initial conditions given in equations (148) by preparing a “correlation hole” for the non-magnetic distinct part G_{nn}^d such that $G_{nn}^d + G_{nn}^s = \text{const}$. The constant is adjusted to a bulk density value where we expect spinodal decomposition to occur [e.g., $\rho\sigma^2 = 3.2$ at $x = 0.6$, see figure 23(a)]. After adding noise to each (partial) van Hove function $G_{\alpha\beta}^i$ we use equations (149) to iterate the functions forward in time.

In figure 29(a) we show a time series for the distinct part G_{nn}^d for a constant $x = L/2$ -slice (where L is the system size). For comparison we have also included results for the one-body density profile $\rho_n(L/2, z, t)$ obtained from solving equations (144) together with equations (117-119). At time $t = 0$ the correlation hole in the region of $z = 64\sigma (= L/2)$ corresponding to a very localized test particle can be clearly seen for the function G_{nn}^d [see black curve in figure 29(a)]. For times $t \lesssim 20\tau_B$, this correlation hole is being “filled up” again by neighboring particles since the released test particle can move on the substrate. By comparing the results of G_{nn}^d with ρ_n in figure 29, we can define a correlation time t_c after which the local density-density correlations induced by the test particle (completely) disappear. Close inspection shows that for times $t < t_c \simeq 100\tau_B$ the interfaces are more pronounced for the function G_{nn}^d [compare, e.g., the local maxima at $z = 88\sigma$ for the red curves in figure 29]. For later times $t \geq t_c$, these differences become unnoticeable to the eye.

In order to further illustrate the density-density correlations in the surrounding region of the initial position of the test particle, we present snapshots for various partial van Hove functions $G_{\alpha\beta}^i$ in figure 30. It is seen that, after a time period of order $t_c \simeq 100\tau_B$, the spatial structures displayed by the self part $G_{nn}^s(\mathbf{r}, t)$ [shown in the upper row of figure 30] are similarly extended in space as those of the distinct part $G_{nn}^d(\mathbf{r}, t)$ (as well as with similar topology but with different absolute values since the test particle is normalized to $\int d\mathbf{r} G_{nn}^s(\mathbf{r}, t) = 1$). This indicates that the spatiotemporal correlations between different particles became weak after the correlation time t_c . At later times $t \gtrsim t_c$, one observes labyrinth structures with sharp boundaries between two species. This is the typical coarsening behavior characterizing late-stage spinodal decomposition. We note that these structures are similar in character to those displayed

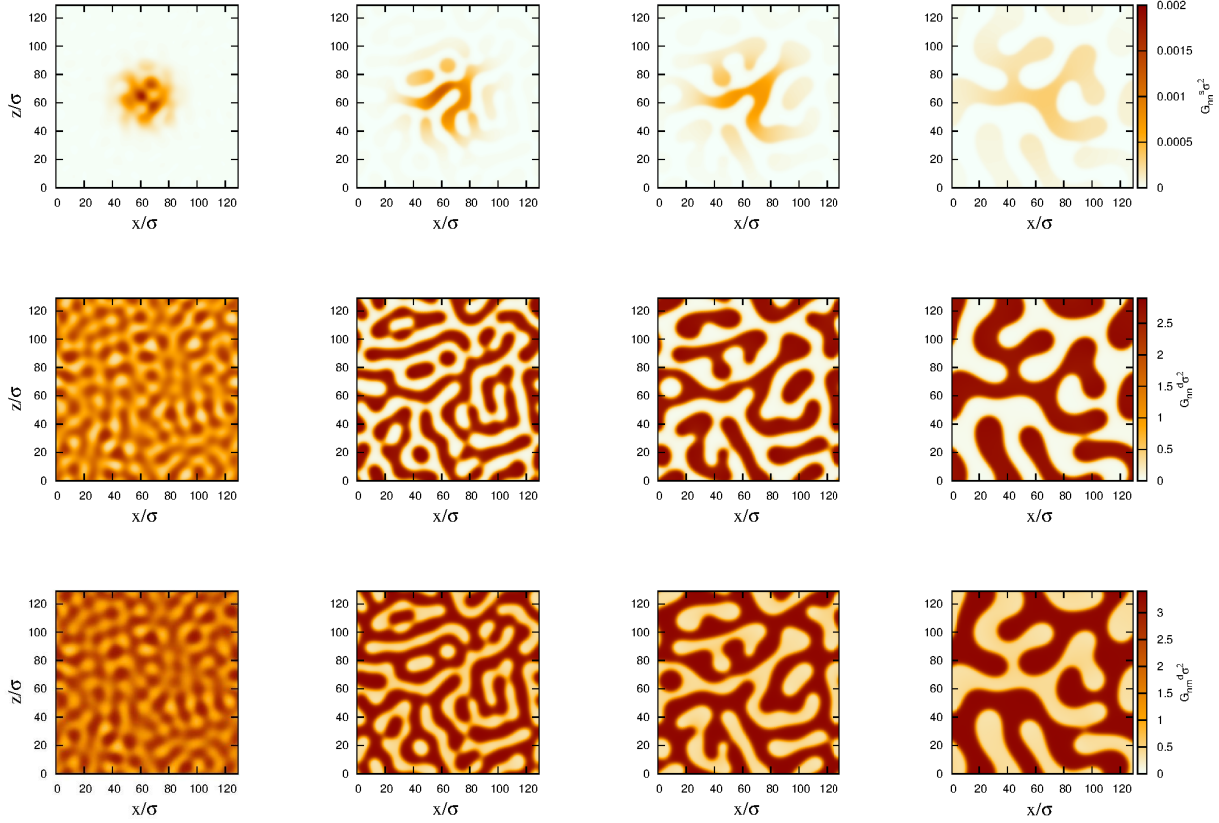


Figure 30.: Snapshots of the partial correlation functions $G_{\alpha\beta}^i(\mathbf{r}, t)$ for the non-magnetic self part (upper row), the non-magnetic distinct part (middle row) and the magnetic distinct part (bottom row) as a function of the position. The non-magnetic test particle was inserted at the position $x = z = 64\sigma$ at time $t = 0$. The time increases from the left to the right: $t_1 = 60\tau_B$, $t_2 = 140\tau_B$, $t_3 = 280\tau_B$ and $t_4 = 800\tau_B$. The parameters are $\rho\sigma^2 = 3.2$, $x = 0.6$, $\varepsilon^* = 5.0$ and $J^* = 0.5$.

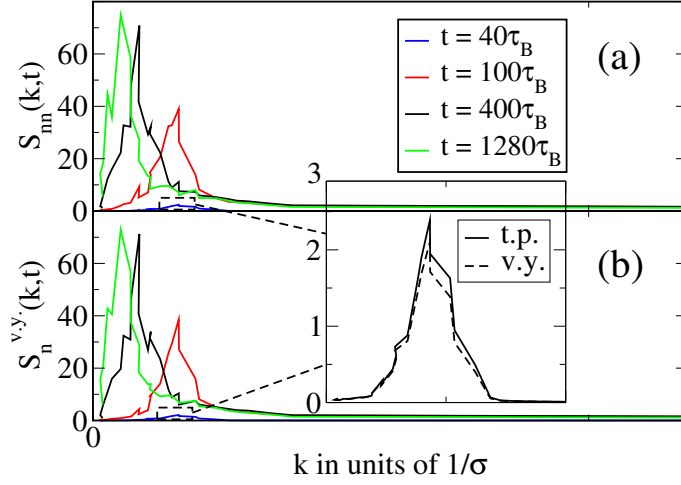


Figure 31.: Dynamic structure factor $S(k,t)$ for the non-magnetic species as a function of the angular-averaged wave number k . (a) shows results obtained from the test particle method and the data in (b) is calculated via a Vineyard type approximation. The inset shows an enlarged view of the curves for the time $t = 40\tau_B$.

by the individual density fields reported in figure 28.

4.4.2. Domain size

In the following, we aim to determine the average domain size $l_\alpha(t)$ for each species α . There are several established routes for calculating the function $l_\alpha(t)$: first, one could determine $l_\alpha(t)$ from the first zero-crossing of $G_{\alpha\beta}(\mathbf{r}, t)$. Second, one may obtain $l_\alpha(t)$ from the first moment of the dynamic structure factor. This is the route we are following here.

The dynamic structure factor corresponds to the Fourier transform of the (full) van Hove function [see equation (146)], that is,

$$S_{\alpha\alpha}(\mathbf{k}, t) = \int d\mathbf{r} e^{i\mathbf{k}\mathbf{r}} [G_{\alpha\alpha}^s(\mathbf{r}, t) + G_{\alpha\alpha}^d(\mathbf{r}, t)]. \quad (155)$$

Here we average the angle-dependent function $S_{\alpha\alpha}(\mathbf{k}, t)$ over all directions of \mathbf{k} within the x - z -plane yielding the angle-averaged structure factor $S_{\alpha\alpha}(k, t)$. The first moment

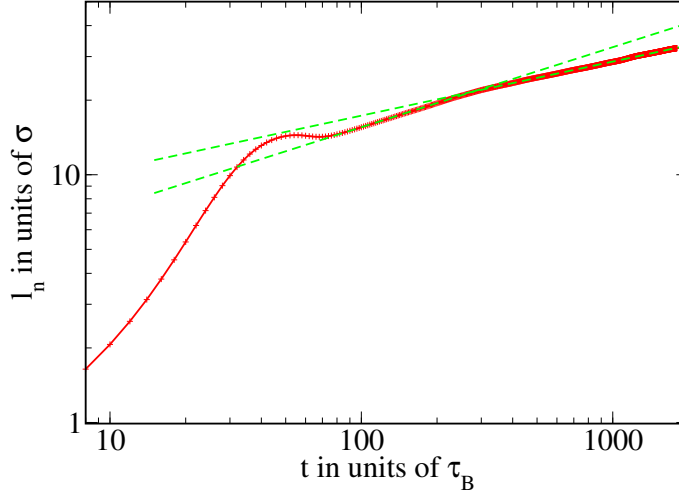


Figure 32.: The average domain size $l_n(t)$ for the non-magnetic species as a function of time in a double logarithmic representation as obtained from equation (155) via the test particle route. The fitting functions are shown as dashed lines. The coupling parameters are $\varepsilon^* = 5.0$ and $J^* = 0.5$.

of this function is given by

$$\langle k_\alpha \rangle_t = \frac{\int k S_{\alpha\alpha}(k, t) dk}{\int S_{\alpha\alpha}(k, t) dk}. \quad (156)$$

From that we can calculate the average domain size as $l_\alpha(t) = 2\pi/\langle k_\alpha \rangle_t$.

In figure 31(a) we show results for the (angle averaged) dynamic structure factor $S_{nn}(k, t)$ obtained from equation (155) [choosing data for the non-magnetic species as an example]. Clearly, we find one dominating average cluster size for all considered times as can be seen from the single peak structure of $S_{nn}(k, t)$. As time increases, the peak is shifted towards smaller wave numbers corresponding to larger average cluster sizes in the system.

We now turn to the time dependence of the resulting domain sizes. For times $t \lesssim 100\tau_B$ we recall that sharp interfaces have still not fully evolved in both parts of the van Hove functions $G_{nn}^s(\mathbf{r}, t)$, $G_{nn}^d(\mathbf{r}, t)$ [cf. figures 29(a) and 30]. Consequently, we do not observe a power law behavior for $l_n(t)$ on this time scale as can be seen in figure 32.

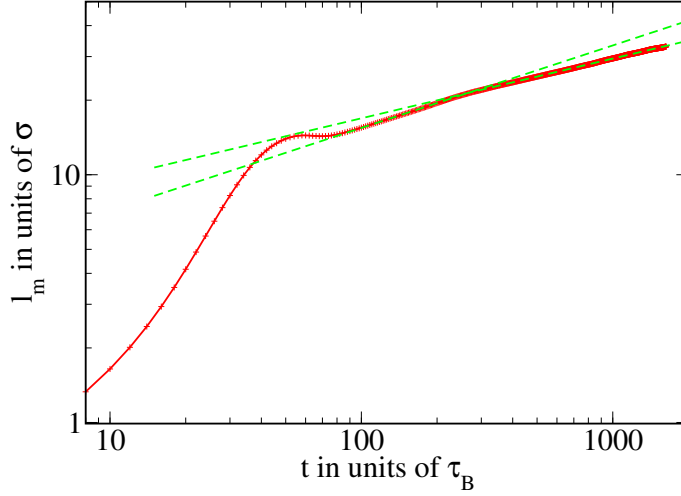


Figure 33.: Same as figure 32, but for the magnetic species. The fitting functions are shown as dashed lines. The coupling parameters are $\varepsilon^* = 5.0$ and $J^* = 0.5$.

For later times $t \gtrsim 100\tau_B$, on the other hand, we find that the function follows a power law behavior $l_n(t) \propto t^{\delta_n}$ with exponent $\delta_n \simeq 0.323$ similar to the power-1/3 rule that is expected for systems with conserved order parameters [150]. However, this exponent changes abruptly to $\delta_n \simeq 0.218$ for times $t \gtrsim 280\tau_B$. We suspect that this crossover could be a consequence of a finite size effect: at $t \gtrsim 280\tau_B$ the domain growth has progressed so far that some domains penetrate the boundaries. We recall that we use periodic boundary conditions, i.e. any particle transport current going through the boundary reenters from the other side. Thus, each affected domain artificially separates into two “distinct” domains resulting in decreased values for $l_n(t)$. Supporting our arguments, Brownian dynamics simulations for Lennard-Jones-type particles have shown that spinodal decomposition kinetics only follows the “classical” power law behavior with exponent $\delta = 1/3$ (for conserved systems) as long as the average domain size does not approach the scale of the simulation cell [155; 156].

In figure 33 we show the corresponding results for the magnetic species. After sharp interfaces have been formed (cf. figures 29,30), we observe a t^{δ_m} power law behavior for the characteristic length $l_m(t)$, where $\delta_m \simeq 0.333$. For times $t \gtrsim 280\tau_B$ this exponent changes to $\delta_m \simeq 0.241$. Hence, the general behavior for the growth of the average magnetic domain is consistent with our observations made for the non-magnetic species.

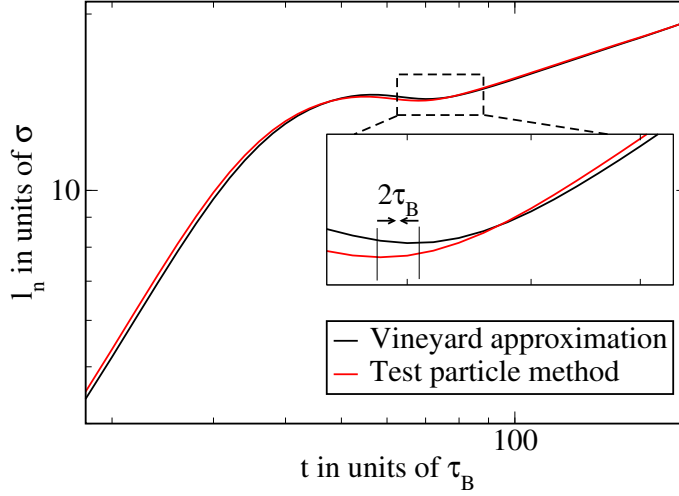


Figure 34.: Log-log representation of the average domain size (non-magnetic species) as a function of time. The black curve is a result obtained from a Vineyard type approximation [calculated via the relation $l_n^{v,y} = 2\pi / \langle k_n \rangle_t^{v,y}$ using equations (156,157)] and the red curve is a test particle method result. The inset shows a close-up view of the range of times where the formation of sharp interfaces occurs [cf. figure 30]. The parameters are $\rho = 3.2$, $\varepsilon^* = 5$ and $J^* = 0.5$.

Finally, it is interesting to compare the results based on the true dynamic structure factor (obtained from the van Hove function) with those from the so-called Vineyard approximation [95; 139]. Within the latter, the dynamic structure factor is given by the absolute value of the one-body density profile $\rho_\alpha(\mathbf{r}, t)$, that is,

$$S_\alpha^{v,y}(\mathbf{k}, t) = |\hat{\rho}_\alpha(\mathbf{k}, t)|, \quad (157)$$

$$\hat{\rho}_\alpha(\mathbf{k}, t) = \int d\mathbf{r} e^{i\mathbf{k}\mathbf{r}} \rho_\alpha(\mathbf{r}, t), \quad \alpha = \{m, n\}.$$

Thus, the Vineyard approximation is a mean-field approximation which neglects spatiotemporal correlations. Typical results for the angle-averaged function $S_\alpha^{v,y}(k, t)$ are shown in figure 31(b). Comparing with those for the full structure factor, we find that for times $t > t_c \simeq 100\tau_B$ the results obtained from both approaches are very similar. On the other hand, for smaller times $t \lesssim t_c$ (where, according to the van Hove functions [see figures 29(a) and 30], sharp interfaces are yet not present) the differences become apparent. In order to further illustrate this, we show a comparison for the

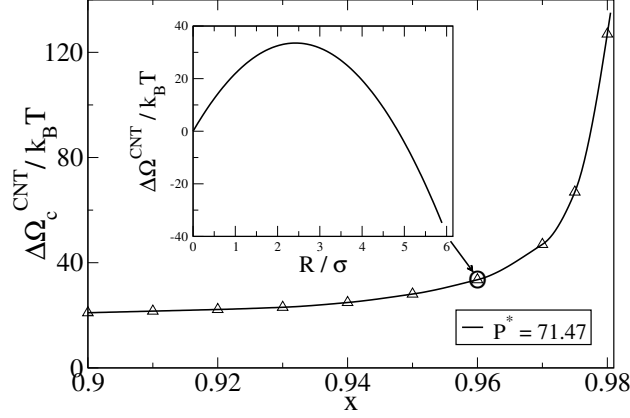


Figure 35.: The nucleation barrier $\Delta\Omega_c^{CNT}$ obtained from classical nucleation theory as a function of the concentration x for fixed total density $\rho\sigma^2 = 3.2$. The inset shows the excess grand potential of the nucleus as a function of the radius R for fixed concentration $x = 0.96$. The coupling parameters are $\varepsilon^* = 5.0$ and $\delta = 0.1$.

resulting average domain size $l_n(t)$ in figure 34. Again, we find quantitative differences for the cluster growth for the time regime $t \lesssim t_c$. It seems that the spatiotemporal density-density correlations induced by inserting a test particle in the center of the system act as a catalyzer for the demixing transition: we find that the average domain growth in the test particle method is “ahead” in time by approximately $2\tau_B$ compared to the simple Vineyard type approximation. After $t_c \simeq 100\tau_B$ the Vineyard type approximation produces similar results compared to the results from the test particle approach. This is again a sign that all (initial) density-density correlations have disappeared after the correlation time t_c .

4.5. Nucleation

Before using DDFT to investigate the dynamics of nucleation, it is worth recalling the main results from classical nucleation theory (CNT) and also approaches to nucleation using equilibrium DFT.

4.5.1. Classical nucleation theory

Nucleation is normally considered to be the relevant phase separation mechanism within the *metastable* regions of the phase diagram, i.e., within the regions between the binodals and the spinodal. In these metastable regions, one may consider forming (circular, in 2D) clusters of the new (globally stable) phase with radius R , surrounded by the metastable bulk phase. One finds that the free energy as a function of R initially increases, reaches a maximum at $R = R_c$, the critical radius, and then decreases for $R > R_c$. It is assumed that clusters of a given radius are randomly formed in the system by thermal fluctuations. Clusters with radius $R < R_c$ then typically shrink, since this lowers the system free energy. On the other hand, clusters with $R > R_c$ must grow without limit (in an infinite size system), since doing this also reduces the system free energy, thereby initiating the transformation into the new (stable) phase. Thus, the excess free energy corresponding to the ‘critical cluster’, i.e. the cluster with radius R_c , is important, because this is the free energy barrier which must be surmounted for the phase separation to occur.

CNT treats the nucleation process on the simplest possible level. The key assumption of CNT is that any cluster (regardless of its actual size) can be regarded as a macroscopic object with a homogeneous density (and thus, pressure) inside and outside its surface. Moreover, interfacial curvature effects are typically neglected. As a consequence, the free energy related to creation of a nucleus can be written as a sum of two terms: a negative contribution stemming from the difference of the (bulk) pressures inside and outside the nucleus, and a positive contribution related to the increase of surface free energy. The latter is determined by the interfacial tension γ of a planar interface (we use the interfacial tension calculated in Sec. 4.2.4 above). Applying this concept to the two-dimensional system at hand, the grand potential for the creation of a n -rich phase nucleus in the surrounding “sea” of m -rich phase is

$$\Omega^{\text{CNT}}(R) = -P_m \mathcal{A} - \pi R^2 |\Delta P| + 2\pi R \gamma, \quad (158)$$

where \mathcal{A} is the total system area, $\Omega_0 \equiv -P_m \mathcal{A}$ is the grand potential of the uniform m -rich phase and ΔP is the difference between the bulk pressure P_m and the pressure of the n -rich phase that is being nucleated. The nucleation barrier is then given by the maximum of $\Delta\Omega^{\text{CNT}} = \Omega^{\text{CNT}} - \Omega_0$ which follows from equation (158) as

$$\Delta\Omega_c^{\text{CNT}} = \frac{\pi\gamma^2}{|\Delta P|}. \quad (159)$$

The corresponding critical radius is

$$R_c = \frac{\gamma}{|\Delta P|}. \quad (160)$$

For $R > R_c$ the grand potential decreases, indicating the absence of a sustaining force against the growth of a drop of the new phase.

In the present calculations we focus on nucleation on the right-hand side of the phase diagram, i.e., the formation of non-magnetic clusters predominantly containing n -particles, out of the ferromagnetic, m -dominated liquid. We consider the nucleus and its environment (i.e., the undersaturated magnetic liquid) at the same pair of chemical potentials μ_n, μ_m . Because we are working on the right side of the phase diagram, these chemical potentials are typically smaller than those corresponding to phase coexistence. The quantity ΔP appearing in equations (158)-(160) is then defined as the difference between the pressure corresponding to the actual magnetic state on the right side, and the pressure of the corresponding non-magnetic state on the left hand side of the phase diagram. These states with equal chemical potentials (as well as the associated pressures) are found from the bulk free energy given in equation (120), which yields the desired quantities through the relations

$$\mu_n = f + \rho \left(\frac{\partial f}{\partial \rho} \right)_x - x \left(\frac{\partial f}{\partial x} \right)_\rho, \quad (161)$$

$$\mu_m = f + \rho \left(\frac{\partial f}{\partial \rho} \right)_x + (1-x) \left(\frac{\partial f}{\partial x} \right)_\rho, \quad (162)$$

$$P = \rho^2 \left(\frac{\partial f}{\partial \rho} \right)_x. \quad (163)$$

In figure 35 we plot CNT results for the free energy barrier height $\Delta\Omega_c^{\text{CNT}}$ for a range of concentrations x of the magnetic species within the metastable regime. The chosen path corresponds to states at constant total density $\rho\sigma^2 = 3.2$. The inset shows the grand potential [see equation (158)] as a function of R for one particular state point. As expected from the structure of equation (159), the nucleation barrier according to CNT becomes infinitely large at the coexistence line, where $\Delta P = 0$. For the total density $\rho\sigma^2 = 3.2$, the binodal is at the concentration $x = 0.985$. Decreasing then the concentration towards the spinodal value, the barrier height decreases. Note, however, that the barrier directly at the spinodal is not exactly zero, as one would expect at the limit of metastability. This deficiency is a well-known artefact of CNT. Indeed, given that CNT is a macroscopic theory, it is not surprising that its predictions become unreliable when the critical clusters become so small that they contain only a few

particles. Under such conditions, a microscopic theory such as DFT is clearly more appropriate.

4.5.2. DFT approach to nucleation

Since the important work of Oxtoby and Evans [157] there has been much work done using DFT to obtain a more reliable (microscopic) estimate for the free energy barrier $\Delta\Omega_c$ – see e.g. references [158; 159; 160; 161; 135] for examples of recent work. Here, we use the Oxtoby-Evans approach to study the nucleation of isotropic clusters of the phase rich in n -particles, and compare the resulting free energy barrier with the corresponding CNT results discussed in section 4.5.1.

The key idea in all equilibrium DFT based approaches to nucleation is that the density profile characterizing the critical nucleus corresponds to a saddle point of the grand canonical free energy [157]. Assuming a symmetric droplet in the center of the system, the goal is thus to find the density profiles $\rho_\alpha(\mathbf{r}, \omega) = \rho_\alpha(x, z, \omega)$ for which

$$\frac{\delta\Omega[\{\rho_\alpha\}]}{\delta\rho_\alpha(\mathbf{r}, \omega)} = \frac{\delta\mathcal{F}[\{\rho_\alpha\}]}{\delta\rho_\alpha(\mathbf{r}, \omega)} - \mu_\alpha = 0, \quad (164)$$

with the boundary conditions

$$\lim_{r \rightarrow \infty} \rho_\alpha(x, z, \omega) = \rho_\alpha^{\text{bulk}}(x, z, \omega)|_{\{\mu_\alpha\}} \quad (165)$$

$$= \rho_\alpha^{\text{bulk}} h_\alpha^{\text{bulk}}(\omega), \quad (166)$$

where $r = \sqrt{x^2 + z^2}$. As demonstrated by Oxtoby and Evans [157], these density profiles may be found by iterating the Euler-Lagrange equations, beginning with a simple approximation for the initial profiles. The latter are characterized by spherical symmetry and a sharp (step-wise) change of the number density at a radius R . The idea then is that if the guessed radius is too small (large), the droplet will shrink (grow) during the iteration procedure until the profiles eventually approach the density values corresponding to the globally stable (unstable) phase. However, to identify the critical droplet one must iterate the Euler-Lagrange equations a limited number of times (for each initial guess R). This procedure allows for an estimate of the grand potential Ω as function of R . The critical droplet then follows as the position of the maximum. Inspired by these ideas we have performed additional calculations, not with the DDFT (which will be discussed below), but with a simple,

relaxational algorithm which is equivalent to the Oxtoby-Evans method. Importantly, this algorithm keeps the chemical potentials fixed (just as in the original Oxtoby-Evans

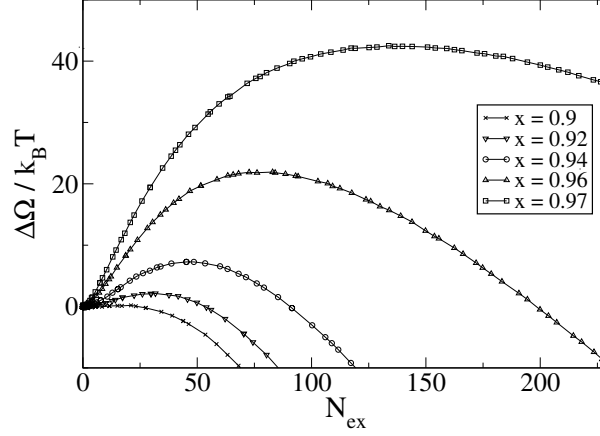


Figure 36.: The grand potential $\Delta\Omega$ of the nucleus obtained from the DFT approach as function of the excess number N_{ex} for different concentrations. The parameters are $\rho\sigma^2 = 3.2$, $\varepsilon^* = 5.0$ and $\delta = 0.1$.

work [157]), while the number densities themselves are not conserved. Using this algorithm we investigated the evolution of several initial profiles of the form

$$\rho_\alpha(x, z) = \begin{cases} \rho_\alpha^{\text{I}}, & \text{if } r < R \\ \rho_\alpha^{\text{II}}, & \text{else} \end{cases},$$

$$M(x, z) = \begin{cases} 0, & \text{if } r < R \\ M^{\text{II}}, & \text{else} \end{cases}. \quad (167)$$

The initial values for the densities inside (ρ_α^{I}) and outside (ρ_α^{II}) the nucleus, are set to the bulk densities determined by the chosen value of the chemical potentials. The magnetization for these state points is obtained self-consistently from equation (117). For each initial guess, we performed about 300 iterations of the density profiles and the corresponding orientational profile, keeping the chemical potentials fixed. In this way we obtained an estimate of the excess free energy $\Delta\Omega$ for each given cluster size. As it turns out, the actual density profiles characterizing the clusters are rather smooth, such that the definition of a radius becomes ambiguous. As an alternative ‘reaction

coordinate', we thus consider the quantity

$$N_{\text{ex}} = \int dx \int dz (\rho_n(x, z) - \rho_n^{\text{bulk}}). \quad (168)$$

which counts the number of n -particles in the cluster (recall that we are considering the nucleation of isotropic n -dominated clusters). Numerical results for the functions $\Delta\Omega(N_{\text{ex}})$ at various chemical potentials within the metastable regime are plotted in figure 36. More precisely, the chemical potentials considered are associated to concentrations (of m -particles) between the spinodal and the binodal along a path with fixed total number density $\rho\sigma^2 = 3.2$ (CNT results along this path are presented in figure 35). As may be seen from figure 36, all the curves reveal a clear maximum and thus, a clearly identifiable nucleation barrier, the height and position of which increase upon increasing the associated (bulk) concentration x . This finding is fully consistent with our expectation that the nucleation barrier and the size of the critical droplet are smallest close to the spinodal and then increase monotonically upon approaching coexistence. From the positions of the maxima in $\Delta\Omega(N_{\text{ex}})$ we also see that typical critical droplets contain between a few ten and a few hundred of particles, consistent with results of other DFT studies [135; 161]. Our data for the height of the nucleation barrier as function of the concentration are summarized in figure 37, where we have included the corresponding macroscopic (CNT) results from figure 35. The main difference between the two approaches is that the microscopic DFT calculation yields, contrary to CNT, a vanishing nucleation barrier at the spinodal, as one should expect on physical grounds. On the other hand, approaching the binodal the two curves merge, reflecting the increasingly macroscopic character of the critical cluster.

4.5.3. DDFT approach to nucleation

Whilst it is clear that the above and other equilibrium DFT based approaches are able to calculate the density profiles corresponding to the critical droplet, it is not clear whether the other density profiles (i.e. those not corresponding to the critical droplet) have any physical significance. Of particular interest are the density profiles corresponding to the most likely pathway (MLP) that go up to and then descend from the critical droplet state [160; 161; 135; 162]. These MLP profiles should correspond to what one would observe experimentally for nucleation in the system.

Recently, Lutsko [162] argued that one should be able to determine the MLP using DDFT by initiating the system at the critical droplet density profiles. Since these profiles correspond to a saddle point, and in reality one is never able to initiate the

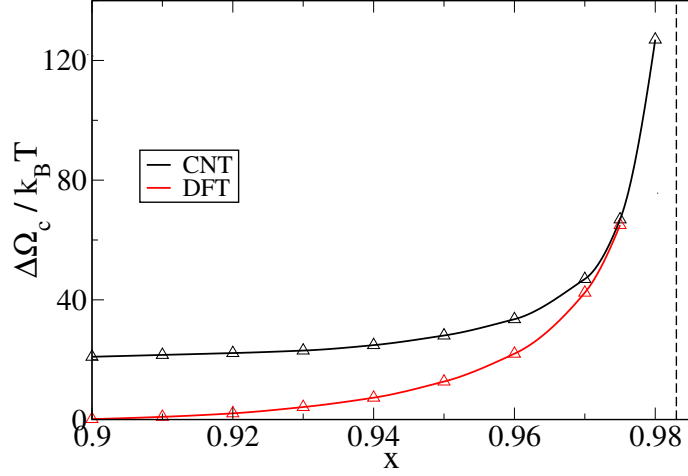


Figure 37.: The nucleation barrier $\Delta\Omega_c$ obtained from classical nucleation theory (black curve) and from the DFT approach (red curve) as function of the concentration x . The dashed curve denotes the state point of coexistence. The parameters are $\rho\sigma^2 = 3.2$, $\varepsilon^* = 5.0$ and $\delta = 0.1$.

system exactly at the saddle point, the density profiles evolve under the DDFT away from this point. There are two directions the system may move: firstly, towards a state corresponding to the drop disappearing, with the excess density being spread uniformly throughout the system and secondly, the drop may grow.

The performance of DDFT in this context is not yet fully understood (see reference [162]), contrary to with the static DFT approaches mentioned above. One issue in this context is the fact that, within the DDFT, the number densities are conserved quantities [as reflected by the appearance of a divergence in front of the free energy derivative in equation (144)]. This is in contrast to traditional (static) DFT approaches towards nucleation, where the fixed quantity is the chemical potential(s).

In view of this subtle point, and given the rather plausible results from the DFT approach described so far, it is an important question whether a different algorithm, and particularly the conserved dynamics implied by the DDFT [see equations(144)-(145)], yields consistent results. We recall that the DDFT is constructed such that the density evolves towards a profile which minimizes the free energy (one can prove that the free energy always decreases or remains constant under the time evolution of the DDFT, unless the system is externally driven [120]). Therefore, one would expect that the critical profile found in the approach discussed above, also ‘behaves’ as a saddle point within DDFT calculations.

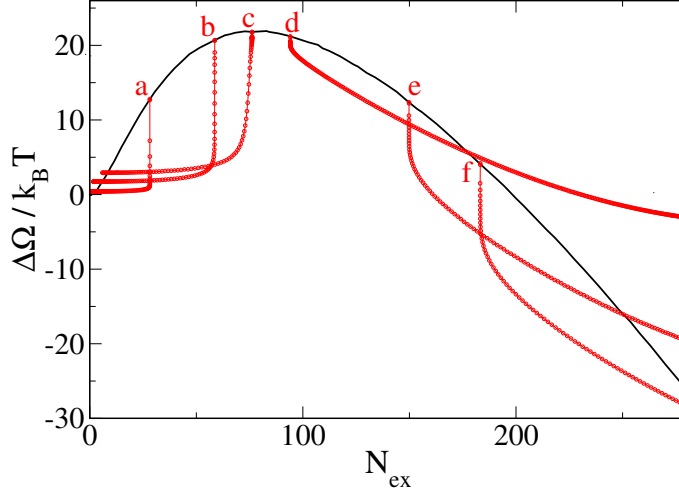


Figure 38.: The grand potential $\Delta\Omega$ of the nucleus as function of the excess number N_{ex} . The black curve is obtained from the DFT approach and the red curve corresponds to DDFT calculations for initial configurations with radius $R = 2.05\sigma$ (a), $R = 2.5\sigma$ (b), $R = 2.75\sigma$ (c), $R = 3\sigma$ (d), $R = 3.6\sigma$ (e), $R = 4\sigma$ (f). The parameters are $\rho\sigma^2 = 3.2$, $x = 0.96$, $\varepsilon^* = 5.0$ and $\delta = 0.1$.

To confirm this, we have performed a number of DDFT calculations with initial density profiles stemming from the DFT calculations described above (after 300 iterations). Some results of these calculations are illustrated in figure 38. Note that for the DDFT results we have used a slightly different definition of N_{ex} . The DDFT calculations are performed on a finite size square area of length $L = 64\sigma$, with periodic boundary conditions. We start with the drop located at the center and we define

$$N_{\text{ex}} = \int dx \int dz (\rho_n(x, z) - \rho_n^{\text{corner}}), \quad (169)$$

where $\rho_n^{\text{corner}} = \rho_n(0, 0) = \rho_n(0, L) = \rho_n(L, 0) = \rho_n(L, L)$ is the value of the density at the corners of the (square, periodic) system. During the initial stages of the evolution $\rho_n^{\text{corner}} = \rho_n^{\text{bulk}}$, and so the value of N_{ex} remains constant due to the conserved dynamics. However, at later times ρ_n^{corner} changes, and so N_{ex} changes with time. This is because either excess density from the center of the system diffuses out to the corner as the drop disappears, or because as the drop grows it removes particles of species n from the surrounding fluid and so ρ_n^{corner} decreases.

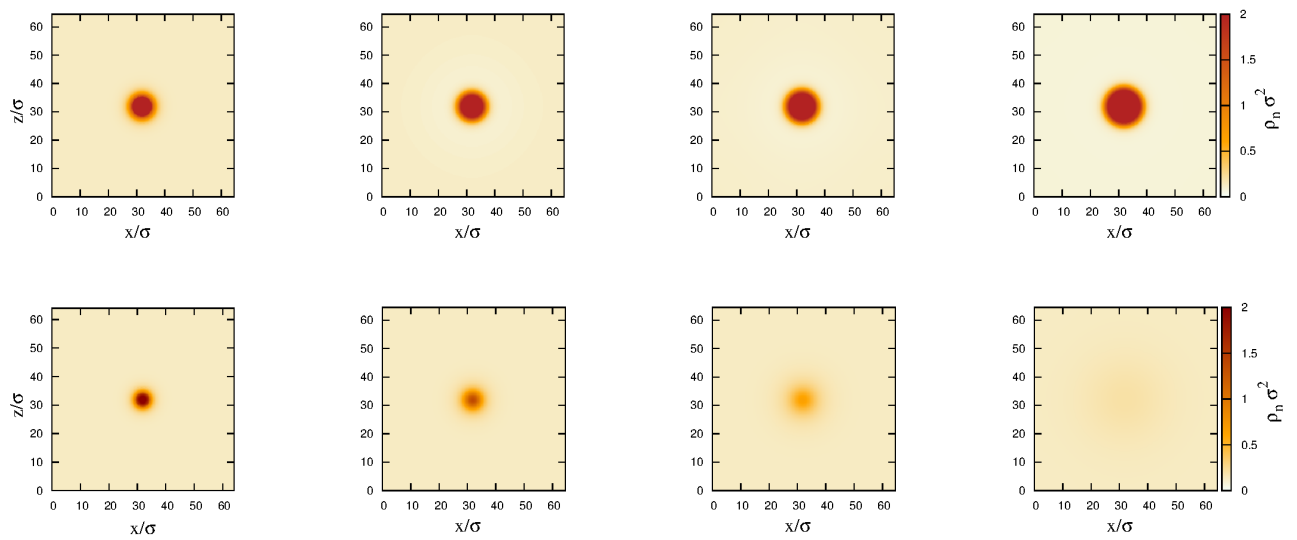


Figure 39.: Density profiles of the isotropic particles (species n) as function of the position. The upper row shows a supercritical growing nucleus ($R^{initial} = 3.6\sigma$) for subsequent times. The bottom row shows a time sequence for a subcritical nucleus ($R^{initial} = 2.5\sigma$). The time increases from the left to the right. Upper row: $t_1 = 0\tau_B$, $t_2 = 200\tau_B$, $t_3 = 600\tau_B$ and $t_4 = 2000\tau_B$. Bottom row: $t_1 = 0\tau_B$, $t_2 = 40\tau_B$, $t_3 = 80\tau_B$ and $t_4 = 200\tau_B$. The parameters are $\rho\sigma^2 = 3.2$, $x = 0.96$, $\varepsilon^* = 5.0$ and $\delta = 0.1$.

In figure 38 the curves labelled by a,b,c correspond to calculations where the radius characterizing the initial profile is smaller than that characterizing the critical droplet predicted by the previous DFT approach. On the other hand, the curves labelled by d,e,f have been started from “supercritical” clusters. In all cases, the DDFT algorithm evolves in the direction predicted by the previous free-energy approach. That is, when starting from a subcritical or supercritical profile, respectively, the droplet vanishes or grows without restriction. We also see from figure 38 that the actual values of $\Delta\Omega$ “on the way” towards the final state are strongly different from those predicted by the previous approach. The interpretation of this issue clearly needs further investigation (see also the discussion in reference [162]).

Furthermore, in the limit $N_{\text{ex}} \rightarrow 0$ the DDFT curves a,b,c approach different values, which depend on the initial profile. This is a consequence of the fact that the initial profiles a-c correspond to different space-averaged densities. This stems from the fact that the DDFT conserves the total densities, and so the final state emerging for subcritical clusters does not necessarily have chemical potentials equal to those chosen in the previous DFT calculations. We conclude that, at least, the DDFT predictions for the critical nucleus are consistent with the traditional DFT theory. Typical density profiles illustrating the nucleation dynamics according to DDFT on a microscopic (space-resolved) level are shown in figure 39. Besides the shrinking/growth process, we remark in particular the diffuse character of the density profiles, which directly reflects the difficulty in associating a fixed radius to the instantaneous droplets.

4.6. Summary

In this chapter we investigated the demixing phase transition of a binary mixture of magnetic and non-magnetic soft-core particles from both a static and a dynamic point of view. To this end we have employed, both, classical equilibrium DFT as well as DDFT. After presenting the bulk phase diagram, we performed a linear stability analysis to identify those wave numbers k that correspond to growing harmonic density perturbations. We find that the linear analysis underestimates the occurrence of spinodal decomposition resulting in wrong predictions for states near the spinodal. Indeed, other studies [139] confirm that in this case nonlinear terms have to be included for the equation of motion.

In the second part, we used a DDFT approach to address the *real-time* coarsening dynamics inside the coexistence region. By inserting a test particle into the homogeneous fluid combined with an “identification scheme” suggested by references [82; 83] we obtained the (partial) van Hove functions $G_{\alpha\beta}^i(\mathbf{r}, t)$. This route opened up an

access to calculate the average cluster size $l_\alpha(t)$. We showed that the coarsening during the first-order demixing transition is characterized by different time-scales: for times $t \lesssim 20\tau_B$ we find that the diffusion-controlled relaxational dynamics of the test particle in the free energy landscape formed by the “sea” of the remaining particles is predominant. After this time scale the formation of sharp domain interfaces takes place while the average cluster size l_α increases. Within a time period of approximately $100\tau_B$ we observe the formation of sharp interfaces throughout the system. For times beyond this correlation time we find late-stage spinodal decomposition where the average cluster growth (as obtained from the dynamic structure factor) is given by a power-law behavior $l_\alpha \propto t^{\delta_\alpha}$ with $\delta_n \simeq 0.323$ and $\delta_m \simeq 0.333$ being the exponents for the non-magnetic species and the magnetic species, respectively. We note that these exponents are in agreement with the “classical” power law for conserved systems, that is, $\delta_{cl} = 1/3$ [150].

We also compared the predictions for $S_{\alpha\alpha}(k, t)$ and $l_\alpha(t)$ from the test particle scheme with corresponding ones from the simpler Vineyard approximation. The latter neglects spatiotemporal density correlations. Moreover, the effective mean field $B(\mathbf{r}, t)$ for the angular distribution function $h_m(\mathbf{r}', \omega', t)$ is linear in $\rho_m(\mathbf{r}, t)$ within the Vineyard approximation. In contrast, in equation (152) we use the full magnetic van Hove correlation function $G_{mm}(\mathbf{r}, t) = G_{mm}^s(\mathbf{r}, t) + G_{mm}^d(\mathbf{r}, t)$ for the calculation of $B(\mathbf{r}, t)$. By comparing the test particle results to those of the Vineyard approach we conclude that the early time regime of spinodal decomposition where density-density correlations play a role is finished after a correlation time of $t_c \simeq 100\tau_B$. Furthermore, we find that local density-density correlations in the vicinity of the test particle position tend to support the coarsening process during spinodal decomposition: for times up to t_c the interfacial structures are more pronounced as compared to the Vineyard system. For very late times these differences fade, i.e. the average cluster growth $l_\alpha(t)$ for both approaches is similar for $t \gtrsim t_c$.

We then focused on the nucleation of non-magnetic clusters within the metastable ferromagnetic phase. We have analyzed and compared results from three different approaches to nucleation. The simplest one is CNT, a macroscopic approach, involving the bulk pressure and line tension. The resulting nucleation barriers show familiar behavior (as compared to other model systems [135; 161]) and predicts that the barrier height increases as one approaches to the binodal. In this regime CNT is expected to give a good approximation for $\Delta\Omega_c$. However, CNT incorrectly predicts that the barrier is finite at the spinodal. As a second step we have investigated the nucleation using the microscopic DFT approach originally proposed by Oxtoby and Evans [157]. In this approach one calculates the free energy as function of an appropriate “reaction coordinate”, which we set to the excess number of particles in the nucleus. The results

for the nucleation barrier are very similar to those from CNT when the fluid state point is near to the binodal. However, in contrast to CNT, the DFT predicts that the nucleation barriers vanishes upon approaching the spinodal, as one should expect on physical grounds.

Finally, we have addressed the issue of the nucleation pathway by comparing the results of the microscopic DFT with those from DDFT. Since both of these approaches are based on the same free energy functional, they are both probing the same underlying free energy landscape. The choice of reaction coordinate to some extent determines what regions of this landscape are accessed and what path to and from the saddle point are predicted. In addition, the ‘dynamics’ inherent in each approach also determines this path. The DDFT has a real (physical) dynamics, which conserves the total number of particles in the system, whilst in contrast the Oxtoby–Evans DFT approach, which has a finite number of iterations starting from an initial guess, leads to having an effective (unphysical) dynamics, which does not conserve the number of particles. Thus, the DDFT is essentially a canonical theory, whereas the DFT approach is more grand canonical in character. As we have shown, these subtleties are irrelevant for the actual height of the nucleation barrier, but yield marked differences when we consider the evolution of profiles away from that of the critical nucleus towards equilibrium.

5. Field-controlled pattern formation

In this chapter we address the interplay of the phase behavior and demixing dynamics with further external influences. To this end, we extend our model from chapter 4 towards 2d magnetic systems exposed to additional external magnetic fields. In fact, a number of recent experiments [43; 44] have addressed the question of phase behavior and transport of magnetic particles on complex substrates [163] driven by magnetic ratchet fields. In contrast to most studies so far, we focus on the impact of a magnetic ratchet potential on the collective behavior, that is, the phase separation dynamics of the mixture. The present results demonstrate that, in combination with a ratchet potential, the attractive forces between the magnetic species in the driven mixture lead to a novel instability, that is, the formation of stripes perpendicular to the direction of the ratchet potential.

5.1. Model

We consider the binary magnetic mixture confined to a two-dimensional substrate [see section 4.1]. The cores of the spherical Brownian particles are soft with effective (gyration) radius σ . One species (n) interacts through purely isotropic repulsive forces and the other species (m) consists of magnetic particles [for the pair potentials see equations (100)-(102)]. For the spin coupling constant we make the choice $J^* = J/(k_B T) > 0$ such that ferromagnetic ordering is favored. We also note that we set $J(|\mathbf{r} - \mathbf{r}'|) = 0$ for distances $|\mathbf{r} - \mathbf{r}'| < \sigma$, i.e., we assume that at these separations the interaction between two magnetic particles is negligible as compared to the repulsion from the core potentials. In fact, for $J^* = 0$ the particles are identical and no demixing occurs. To model the magnetic surface fields we use a one-dimensional rocking ratchet potential [50], that is,

$$\begin{aligned} V_m^{\text{ext}}(\mathbf{r}, t) = & -U [\sin(0.2\pi x/\sigma) + 0.25 \sin(0.4\pi x/\sigma)] \\ & - F \sin(\nu t)x, \end{aligned} \tag{170}$$

where U is the amplitude of the substrate field with broken reflection symmetry and F is the amplitude of an oscillatory driving force with zero mean-force and frequency ν . This ratchet potential acts only on the magnetic species (similar to the static magnetic field in a ferrocolloid-polymer mixture studied in recent experiments, e.g., reference [21]). In the adiabatic limit $\nu \rightarrow 0$ the net current for a single particle subject to this potential is always positive if F exceeds the maximal barrier force, that is, $\max(|\nabla V_m^{\text{ext}}|_{F \rightarrow 0})$. However, for driving frequencies $\nu > 0$ the transport behavior can be rather complex including current reversal phenomena [164].

The non-equilibrium dynamics of the driven system is investigated via a DDFT approach. To this end, we calculate the chemical potential $\mu_\alpha = \delta\mathcal{F}[\{\rho_\alpha\}]/\delta\rho_\alpha$ [which enters equation (144)] employing the Helmholtz free energy functional given in equation (107). The external potential in equation (170) leads to an additional contribution \mathcal{F}_{ext} to the free energy $\mathcal{F} = \mathcal{F}_{\text{id}} + \mathcal{F}_{\text{ex}} + \mathcal{F}_{\text{ext}}$ where

$$\mathcal{F}_{\text{ext}} = k_B T \sum_\alpha \iint d\mathbf{r} d\omega \rho_\alpha(\mathbf{r}, \omega, t) V_\alpha^{\text{ext}}(\mathbf{r}, \omega, t). \quad (171)$$

Note that we set $V_n^{\text{ext}} = 0$, i.e. the external field is not coupled to the isotropic species.

In our approach we factorize the one-body density profile into a translational number density part, $\rho_\alpha(\mathbf{r}, t)$, and a normalized orientational distribution function, $h_\alpha(\mathbf{r}, \omega, t)$ and then set the functional derivative $\delta\mathcal{F}/\delta h_m(\mathbf{r}, \omega, t) = 0$ for all times t (we are thus assuming that the magnetic moments relax instantaneously; see section 4.2.1 for details). We note that this approximation seems justified for magnetic ratchet systems which naturally display large differences in both the rotational and translational time scales. For example, in the experimental study [165], pairs of magnetic particles relax towards their equilibrium distance on a time scale, which is about a factor of 100 larger than that corresponding to the fast rotational movements enforced by external field modulations.

5.2. Results

We consider a state point (ρ, x) well inside the two-phase region of the bulk phase diagram for the exemplary case $\varepsilon^* = 5.0$ and $J^* = 0.5$ [see Fig. 40(a)]. In the absence of the ratchet potential ($V_m^{\text{ext}} = 0$), we observe a first-order demixing transition coupled to a second-order transition from a paramagnetic phase rich in n -particles to a ferromagnetic phase rich in m -particles as can be seen from Fig. 41(a) [see chapter 4 for details].

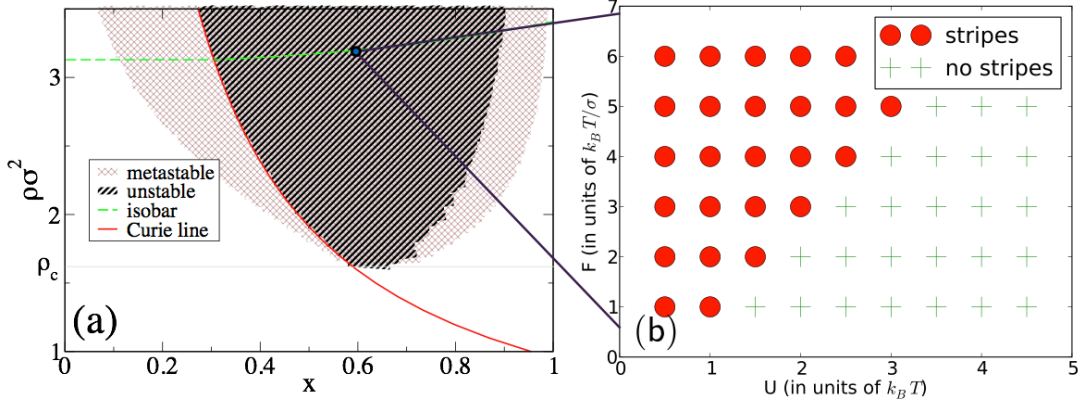


Figure 40.: (a) Bulk phase diagram for the binary n - m mixture in the density-concentration plane where x is the concentration of the m -particles. The green-dashed line is the $P\sigma^2/(k_B T) = 80$ isobar and the Curie line is indicated by the red curve. Unstable and metastable regions are indicated by the shaded regions. (b) Region for stripe formation for the driven system ($\nu = 0.1\tau_B^{-1}$) in the F - U plane inside the two-phase region. For each point in the phase diagram the density profiles have been calculated for times up to $t = 10^4\tau_B$ in order to check for stripe formation. The coupling parameters are $\varepsilon^* = 5.0$, $J^* = 0.5$.

Now, we consider the system where the magnetic particles are subject to the surface field. Without the oscillatory driving force, i.e., setting $F = 0$ in V_m^{ext} [see equation (170)], the external potential becomes static. To illustrate this case we choose a fixed amplitude of the static potential, $U = 1k_B T$. As can be seen from Fig. 41(b), the density distribution ρ_m is peaked at the minima positions of V_m^{ext} . Thus, the static part of the external potential leads to a symmetry break of the magnetic particle distribution, which is the expected behavior in the purely magnetic system (in fact, this behavior is also seen experimentally, see, e.g., reference [86]). Due to the repulsive pair interaction, the non-magnetic species is confined to the space where the density ρ_m is small (i.e., at the maxima positions of V_m^{ext}).

This situation changes when the oscillatory driving force (related to the parameter F) is switched on. We consider a fixed oscillation frequency $\nu = 0.1\tau_B^{-1}$ where the single-particle system displays positive net current [164]. Increasing F beyond a threshold value F_c (where $F_c(U)$ is a critical value depending on the ratchet amplitude U) we observe a shift of the entire density distribution ρ_m (and ρ_n) caused by the external force $|\nabla V_m^{\text{ext}}(\mathbf{r}, t)|$.

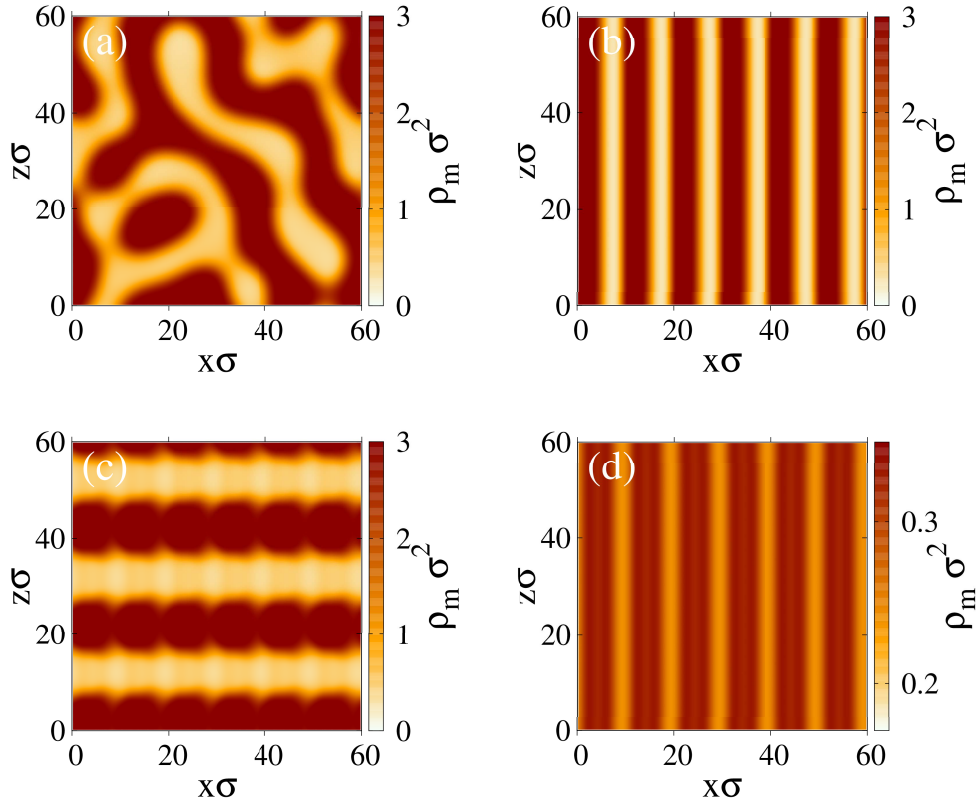


Figure 41.: Typical snapshots of the density profile ρ_m as a function of the position (for simplicity, we only show results for the magnetic species). (a) Demixing without external field ($V_m^{\text{ext}} = 0$) at $t = 120\tau_B$ for an unstable state ($\rho\sigma^2 = 3.2, x = 0.6$) inside the two-phase region [marked point in Fig. 40(a)]. The impact of the external potential on the demixing is shown for $U = 1k_B T$ and $t = 1400\tau_B$ (b) for $F = 0$ (without drive) and (c) for $F = 4k_B T/\sigma$. (d) Snapshot for the same parameters as in (c) but for a stable state ($\rho\sigma^2 = 1.5, x = 0.2$) outside the two-phase region of Fig. 40(a).

Moreover, after several periods T [e.g., after 50 periods for $U = 1k_B T$ and $F = 4k_B T/\sigma$; see Fig. 41(c)] we find non-vanishing values for ρ_m for all x -positions. In other words, we observe a spontaneous symmetry break of the density distribution indicated by the formation of longitudinal stripes. We interpret this dynamical instability as an interplay between the intrinsic spinodal decomposition and the external magnetic force $\propto |\nabla V_m^{\text{ext}}(\mathbf{r}, t)|$: For $F > F_c$, domains of m -particles (and n -particles through the mutual m - n repulsion) are driven over the local barriers of V_m^{ext} . These domains reorganize into stripes since the formation of interconnecting structures is promoted by the bulk system behavior [see Fig. 41(a)]. The strict orientation along the x -direction reflects the fact that the resulting fluid-fluid interface has to be parallel to the driving force (the study [166] proves that curved interfaces are unstable for constant drives).

We checked our calculations with respect to system size dependencies by performing trial runs with different box sizes L . For the values of L considered, we did not find any impact on the formation of stripes. However, we cannot exclude that the dynamical scaling law for the demixing might be influenced by L (see section 4.4.2 for details). Moreover, the positioning of the stripes depends on the initial configuration which is given by the realization of the random white noise applied to the initial bulk profiles. Regarding the wavelength of the pattern in z -direction (i.e., the stripe width), we find that this length tends to decrease with increasing $F/U > F_c/U$. To further highlight the supportive role of the phase separation for stripe formation, we calculate the density distributions ρ_m, ρ_n for the same values of F and U but for a bulk set (ρ, x) outside the two-phase region of Fig. 40(a). Without the intrinsic phase separation the driving force does not suffice for stripe formation [as can be seen in Fig. 41(d)].

Another interesting observation is that the intrinsic coarsening process due to spinodal decomposition (which eventually leads to macroscopically separated phases) slows down significantly over the observation time ($\sim 10^4 \tau_B$) once the alternating sequence of m, n stripes is present [see Fig. 41(c)]. Thus, the external potential $V_m^{\text{ext}}(\mathbf{r}, t)$ may also be used to suppress spinodal decomposition in one direction contrary to an equivalent system with $V_m^{\text{ext}} = 0$ where no direction for the demixing process is favored (cf. Fig. 28). In Fig. 40(b) we depict a non-equilibrium state diagram for the stripe formation in the F - U plane. It is seen that the striped state is separated from the other state by a straight line, i.e., the critical driving force amplitude F_c for stripe formation depends linearly on the ratchet amplitude U . In fact, we find $F_c \sigma = 2 \max(V_m^{\text{ext}}|_{F \rightarrow 0}) - \Delta(J, \varepsilon)$ where $\max(V_m^{\text{ext}}|_{F \rightarrow 0}) \simeq 1.1U$ is the energy barrier of the static part of V_m^{ext} and $\Delta(J, \varepsilon)$ is a positive constant depending on the internal interactions of the system (e.g., $\Delta \simeq 1.5k_B T$ for $J^* = 0.5, \varepsilon^* = 5$). Since the stripe formation is induced by the ferromagnetic coupling, we expect $F_c(U)$ to decrease if J is being increased. We have not observed any hysteresis effects in the F - U plane.

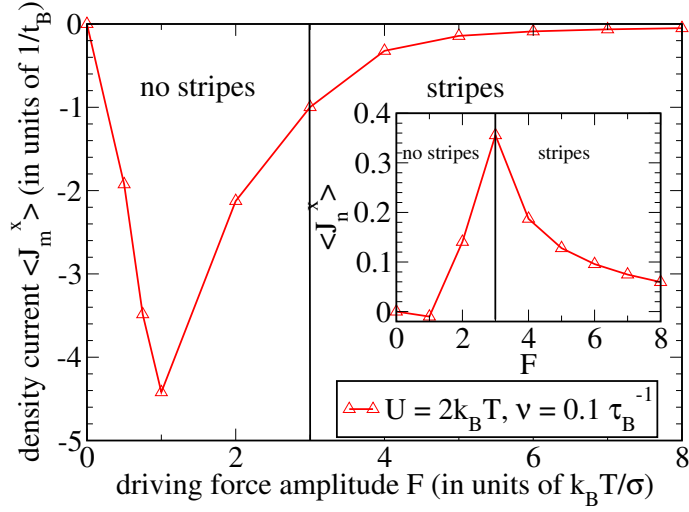


Figure 42.: Net particle current $\langle J_m^x \rangle$ for the magnetic species as a function of F . The inset shows the same curve for the non-magnetic species. The critical driving force F_c is indicated by the vertical lines.

We now explore the impact of the observed dynamical instability on the transport properties of the system. To this end we calculate the density current given by the divergence term in equation (144), that is, $\mathbf{J}_\alpha = -D\rho_\alpha \nabla (\delta\mathcal{F}[\{\rho_\alpha\}]/\delta\rho_\alpha)$. Specifically, we are interested in the particle currents along the x -direction that we obtain by averaging over all z -positions, that is,

$$J_\alpha^x(t) = \frac{1}{N_z} \sum_{i=1}^{N_z} \int_0^L dx J_\alpha^x(x, z_i, t), \quad \alpha = \{m, n\}, \quad (172)$$

where N_z is the number of discretization points in z -direction. In Fig. 42 we show results for the resulting net current that we derive from equation (172) by time-averaging over one period T , that is, $\langle J_\alpha^x \rangle = 1/T \int_{\tilde{t}}^{\tilde{t}+T} dt J_\alpha^x(t)$ where \tilde{t} is a time after the initial transient period (i.e., after the onset of the stripe formation). For a fixed value of $U = 2k_B T$ we follow a path through Fig. 40(b) by varying F . For small values of F we observe a net transport of m -particles in the backward direction, as can be seen from the negative values of $\langle J_m^x \rangle$. We note that this is in contrast to the behavior of a single particle in the ratchet potential, which would display positive current at the parameters considered. This difference is due to an interaction effect, specifically the repulsion between magnetic and non-magnetic particles which sit at

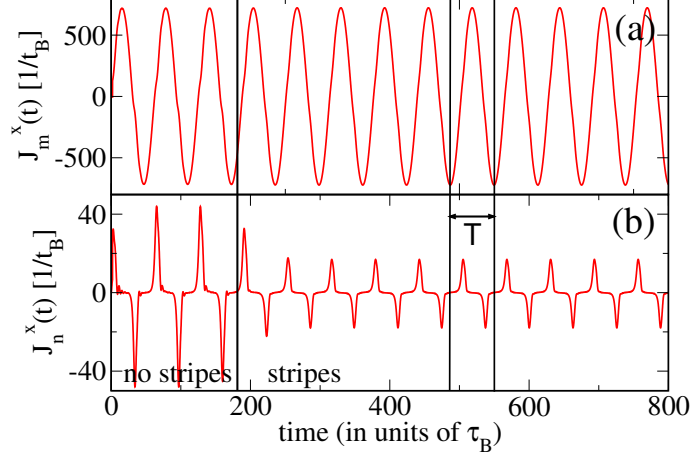


Figure 43.: Averaged particle current along the x -direction as a function of time (a) for the magnetic species and (b) for the non-magnetic species. The onset of the longitudinal stripe formation is at $t \simeq 190\tau_B$. The parameters are $U = 2k_B T$ and $F = 6k_B T/\sigma$.

the potential maxima [see Fig. 41(b)] and thus effectively increase the potential height at the parameters considered. Indeed, we have observed negative currents also for states with vanishing global magnetisation where attractive interactions between the particles are absent. We also note that the actual values for $\langle J_m^x \rangle$ strongly depend on the parameter U . In fact, for larger U (e.g., $U \sim \varepsilon$) we also find positive values for $\langle J_m^x \rangle$. For the value $U = 2k_B T$ considered in Fig. 42, the magnitude of the negative current becomes maximal for $F = 1k_B T/\sigma$. As F is being increased further towards the threshold value $F_c|_{U=2} \simeq 3k_B T/\sigma$ we find that the ratchet effect is decreasing again. Hence, the stripe formation effectively decreases the reflection asymmetry of the potential. In the inset we show the result for the non-magnetic species. Similarly to the magnetic species, we find that the transport of non-magnetic particles is suppressed within the stripe forming region of Fig. 40(b).

Moreover, $\langle J_n^x \rangle$ exhibits a peak as a function of F in the region where the system transitions into the striped state. From the density profiles we conclude that this behavior is linked to the repositioning of the non-magnetic species at the onset of the stripe formation: By further increasing F the particle separation into distinct longitudinal stripes reduces the total number of collisions between different species resulting in a decreased current $|\langle J_n^x \rangle|$. To show the dynamical behavior as the system undergoes the structural transition we exemplarily calculate with equation (172) the instantaneous current for a data point of Fig. 40(b) within the stripe forming region.

As can be seen from Fig. 43(a) the current for the m -particles oscillates between $\pm 720\tau_B^{-1}$ with period $T \simeq 62.8\tau_B$ indicating a back-and-forth rocking motion. Due to the n - m repulsion the same behavior is seen for the other species [see Fig. 43(b)] - the large quantitative difference between J_n^x and J_m^x reflects the fact that V_m^{ext} only couples to the m -particles. Furthermore, we observe a sudden drop in the amplitude of the J_n^x -oscillations at $3T \simeq 190\tau_B$ [see Fig. 43(b)]. From inspecting the density snapshots we find that this current drop is linked to the onset of the global stripe formation. Thus, the behavior of the n -particles serves again as a true indicator for signaling the transition into the striped state (cf. Fig. 42).

5.3. Summary

In this chapter we demonstrated that the non-equilibrium pattern formation in a phase separating colloidal mixture can be efficiently manipulated by applying external time-dependent surface fields (represented here by the one-body potential V_m^{ext}). For $V_m^{\text{ext}} = 0$, the system exhibits a first-order demixing transition accompanied by spinodal decomposition, i.e. with no favored direction for the domain growth. This symmetry is already broken if we switch on a static external potential ($F \rightarrow 0$) acting on the magnetic species.

Moreover, for the driven system ($F > 0$) we demonstrated that the *direction* of the symmetry break can be changed if the condition $F\sigma \geq 2\max(V_m^{\text{ext}}|_{F \rightarrow 0}) - \Delta$ is met where the first term on the right hand side is the energy barrier of the static part of the external potential and $\Delta = \Delta(J, \varepsilon)$ is a constant depending on the internal interactions of the system. We note that, in principle, the quantity $\Delta(J, \varepsilon)$ can be estimated by employing a linear stability analysis combined with continuation methods (see, e.g., reference [41]). The structural transition (that we call *stripe formation*) suppresses the transport of particles along the x -direction that is otherwise observed due to the magnetic ratchet effect. Indeed, the transport behavior turns out to be non-trivial due to the collective effects but remains tunable by the parameters U and F .

We stress that the stripe formation is a combinatory effect of the underlying demixing transition and the (one-body) interactions with the external surface fields. Indeed, without the demixing we cannot find any transition for the values F/U considered here. Moreover, we note that the stripe formation is quite robust against changes of the ratchet amplitude U , driving amplitude F (with F/U being constant), as well as the total density ρ and concentration x (inside the two-phase region). Indeed, for closed systems (i.e., without particle exchange), the parameter x seems to be a suitable parameter for controlling the size of the globally forming stripes. We also

observed robustness of the stripe formation against the frequency ν (for the range $0.05-1\tau_B^{-1}$). For higher frequencies (e.g., $\nu \gtrsim 5\tau_B^{-1}$ for $F\sigma/U = 1$) current reversal phenomena have been reported in the single-particle limit [164].

Finally, we note that pattern formation in phase separating systems may also be controllable by applying other types of external forcing. Indeed, a recent theoretical study for the Langmuir-Blodgett transfer reveals that the self-organization of the particles may be manipulated by changing, both, the substrate properties and the transfer velocity [41; 167]. In another study [168] the effects of a quench interface traveling with constant velocity v on the coarsening has been studied based on a Cahn-Hilliard approach. The studies [41; 167; 168] report periodic solutions that are parallel and perpendicular to the quench interface (contact line in references [41; 167]). However, these solutions are not aligned against the symmetry of an external periodic field as it is the case for the present study. In fact, the study [168] employs an additional periodic modulation in the perpendicular direction generating different modes including cellular patterns. Thus we find, to the best of our knowledge, a novel type of structure formation for a phase separating magnetic mixture subject to time-dependent (open-loop) fields.

6. Concluding remarks

6.1. Summary of this thesis

In this thesis we have studied various one- and two-component systems of colloidal suspensions with soft repulsive interactions and permanent (or induced) magnetic moments. Inspired by recent developments in the context of non-equilibrium phenomena, we focused on one-dimensional channel geometries [48; 49; 50; 51; 65] as well as on two-dimensional systems representing liquid thin film geometries or surfaces [44; 84; 43; 42; 85; 87]. For our research we mainly used density functional theory (DFT) employing, both, the static and dynamical versions.

In the first part of this thesis, we considered driven systems of interacting colloidal particles in periodically corrugated narrow channels. We demonstrated that, despite of pronounced spatio-temporal correlations, the particle current can be stopped or reversed by adding suitable closed-loop control terms to the DDFT equation of motion. Moreover, we showed that time-delayed feedback can be used to induce oscillatory density states corresponding to synchronized particle oscillations along the channel. We have shown that related control goals can be achieved with different loops that involve the same delay time τ (chosen similar to the intrinsic, Brownian time scale) but different targets (average particle position versus density profile). The fact that the schemes produce comparable results indicates a certain robustness of the feedback control method for transport phenomena in 1D systems, consistent with earlier theoretical findings for ratchet systems [66; 71; 111; 70] and for non-interacting particles in tilted washboards [72; 73]. In that sense, our studies also support the more general perspective that closed-loop control can be extremely useful for the manipulation of non-linear systems [68]. Beyond the actual physical behavior, we showed for the first time that time-delayed feedback control can be conveniently implemented within the framework of DDFT.

In the second part, we added a second species with embedded magnetic moments. Our analysis of the equilibrium phase behavior of the system showed that the magnetic (Heisenberg) interaction is capable of inducing macroscopic phase separation. More precisely, for sufficiently large ferromagnetic coupling strength we find a combined

phase transition where the system both demixes and develops global ferromagnetic ordering in one of the phases. Depending on the total density, the transition may either be second or first order (in terms of the magnetization and composition, respectively), with the two regimes being separated by a tricritical point. Thus, the general topology of the phase diagram in the fluid regime, particularly the appearance of a Curie line and a tricritical point, coincides with that of 3D Heisenberg and XY-fluids [30; 46]. Based on DFT we calculated the structure of the fluid-fluid interface in the first-order regime as well as the resulting interfacial tension. As expected, the latter vanishes upon approaching the tricritical point from the high-density side. For the average cluster growth (as obtained from the dynamic structure factor), we observed a power-law behavior $l \propto t^{\delta_\alpha}$ with $\delta_m \simeq 0.333$ for the magnetic species and $\delta_n \simeq 0.323$ for the non-magnetic species. These exponents are in agreement with the classical power law for conserved systems, that is, $\delta_{cl} = 1/3$ [150]. Our results indicate that DDFT is able to show spontaneous demixing for the full unstable region of the phase diagram being thermodynamically consistent in this regard as opposed to theories that are only correct up to linear order in the density. We also addressed the issue of the nucleation pathway by comparing for the first time results from static DFT and DDFT in this context.

In the last part, we demonstrated that the non-equilibrium pattern formation in a phase separating colloidal mixture can be efficiently manipulated by applying open-loop control fields, here, time-dependent surface fields. Specifically, we found that the interplay between the intrinsic spinodal decomposition and time-dependent external forces leads to a novel dynamical instability where stripes against the symmetry of the external potential form. Moreover, the stripe formation suppresses the transport of particles along the x -direction that is otherwise observed due to a magnetic ratchet effect. For an overview of the achieved control goals within the different geometries we include the following table:

<i>control type</i>	1d washboard + feedback closed-loop		2d (bulk) uncontrolled		2d ratchet + surface fields open-loop	
<i>pair interaction</i>	none	repulsive	repulsive	repulsive + attractive	repulsive	repulsive + attractive
goals concerning pattern formation:						
<i>demixing transition</i>	no	no	no	1st order demixing	no	1st order demixing
<i>stripe formation</i>	no	no	no	no	vertical	vertical + horizontal
goals concerning transport properties:						
<i>net transport</i>	no	no	no	no	yes	suppressed
<i>current reversal</i>	yes	enhanced	no	no	yes ¹⁾	yes ¹⁾
1) Can be induced by the ratchet potential; see e.g. reference [164].						

6.2. Outlook and experimental realizations

There are several directions which we believe require further investigation. Since DDFT is an approximate theory, the present results for the impact of control remain to be tested against (quasi-exact) data from Brownian dynamics computer simulations. However, given the good performance of the DDFT in other contexts [169; 170] we expect our findings to be at least qualitatively right. We further note that the present DFT results are based on a mean-field approximation for the excess free energy contribution from both the soft-core repulsion (where mean-field theory has already proven to be very accurate [93]) and from the Heisenberg interactions. Thus, the quantitative reliability of our results remain to be checked against those of more refined free energy functionals and/or computer simulations. Indeed, concerning the phase behavior of the fluid it is well known that the mean-field theory generally predicts very similar results in 2D as it does in 3D (for a recent study see Ref. 171).

A possible extension is to study the present system under external shear. It is known that shear induces a variety of non-equilibrium instabilities such as shear-banding [4], oscillatory wagging motion states [172] or moving interfaces in patterned systems [150; 173]. Indeed, the study [173] indicates that external shear can be used to stabilize the sizes of dynamic patterns. However, the question if secondary instabilities also arise in phase separating systems is essentially unexplored. For the present

magnetic mixture, we expect that possibly new ordered structures could emerge under external shear. It would then be very interesting to investigate how far the spatiotemporal behavior of these sheared structures can be manipulated by applying open- or closed-loop control strategies.

Another interesting idea concerning our results for the patterned surface is to supplement the modulated potential by a feedback control force acting with multiple time delay constants. In fact, a first experimental realization of feedback-controlled currents in flashing ratchets already exists [111]. This could be a promising route for the development of novel particle assemblers on the nano to micro-scale.

Clearly, it would be particularly interesting to extend the present studies to colloids with true dipolar (instead of Heisenberg) interactions (for an experimental realization of a dipolar ferrofluid-nonferrofluid mixture, e.g., see Ref. [21]) or magnetic particles with different surface chemistry, which enable directed self-assembly. Indeed, Yan and colleagues found in a recent study [174; 175] that Janus particles perform synchronized oscillations in a precessing magnetic field which are absent for conventional magnetic spheres. Moreover, these particles self-organize themselves into stable tubular structures. Aiming at the relocation or the fixation of such structures, it would be very interesting to apply magnetic surface fields similar as the ones reported in chapter 5. This could possibly open the way towards novel microdevices, e.g., ones that can be used for the controlled drug delivery in biotechnology. We note that a functional for patchy colloids based on Wertheim's theory [176] already exists, which could be used as a starting point for a (D)DFT study.

We close our comments with a discussion of possible experimental realizations for the systems presented here. For the narrow channel geometry the present results seems possible with micron-sized colloidal particles in 1D tilted washboard potentials created by optical (laser) fields [53; 64; 111]. For instance, the study [64] employs particles of size $\sigma = 1.5\mu m$ in potentials with periodicity $\lambda = 3.14\mu m \approx 2.1\sigma$, and similar dimensions occur in [111]. The barrier heights in [64] are $U = 4.5 - 11.5$, and the biasing forces are in the range $0 \leq F \lesssim 100$, suggesting that our parameters for the uncontrolled system ($\lambda = 8\sigma$, $U = 15$, $F = 3$) are not unrealistic. With respect to control, we stress that in colloidal systems the trajectories of the *individual* particles can be monitored with a video camera [64; 111] yielding, in principle, *both* the average particle position and the full density field as possible control target. Indeed, the average colloid position is also targeted in a recent experimental realization of a flashing ratchet with time-delayed feedback control [111]. Moreover, in these experiments the delay of $\tau = 5ms$ (arising from the finite time required to locate the colloids), is much smaller than the time scale for diffusion ($\approx 300ms$), consistent with our assumption that $\tau \lesssim \tau_B$.

For the results concerning the patterned surface, an experimental realization seems possible, e.g., by employing polystyrene (paramagnetic) particles of size $\sigma = 1.4\mu\text{m}$ on a 2D surface with parallel magnetic stripes created by a ferrite garnet film with spatial periodicity $\lambda = 6.9\mu\text{m} \simeq 4.9\sigma$ [42]. The translation along the horizontal direction is technically feasible by superimposing an external, rotating magnetic field where the target velocity is tunable via the frequency [84; 42]. Typical travel distances within a period $2\pi/\nu$ in Ref. [87] are $0 - 16\sigma$ compared to $0 - 14\sigma$ in the present study, suggesting that our parameters ($\lambda = 10\sigma, 0 \leq F\sigma/U \leq 10, \nu = 0.1\tau_B^{-1}$) are not unrealistic. We note that all quantities in the model system in chapter 5 are, in principle, accessible by experiments [54].

For an experimental counterpart to soft magnetic particles one may employ complex dusty plasmas [177; 178]. By charging paramagnetic dust grains the magnetic interaction between the particles can be superimposed by a repulsive screened electrostatic interaction. In contrast to experiments with magnetic hard spheres [179], the softness of the repulsion may thus be changed by the electrostatic coupling between the grains. We note that a particularly attractive feature of magnetic particles is that the effective pair interaction can be tailored by the application of an external magnetic field [180]. We therefore strongly encourage further experimental investigations based on our theoretical studies.

Appendix

I. Gibbs-Bogoliubov relation

In section 2.1.2 we stated that the grand potential functional satisfies a variational principle. In the following, we complete the proof by employing the Gibbs-Bogoliubov relation for a positive real number x , that is,

$$x \ln x \geq x - 1. \quad (173)$$

Inserting a probability distribution $f \neq f_0$ (where f_0 is the equilibrium distribution) into the grand potential yields

$$\Omega[f] = \text{Tr} f (\mathcal{H}_N - \mu N + \beta^{-1} \ln f) \quad (174)$$

$$= \text{Tr} f (\Omega_0 + \beta^{-1} \ln f - \beta^{-1} \ln f_0). \quad (175)$$

In the last step we have used that

$$\begin{aligned} \ln f_0 &= -\beta(\mathcal{H}_N - \mu N) - \ln \Xi_{\text{gc}} \\ &= -\beta(\mathcal{H}_N - \mu N) + \beta\Omega_0. \end{aligned} \quad (176)$$

Thus, we may replace $\mathcal{H}_N - \mu N = -\beta^{-1} \ln f_0 + \Omega_0$ in equation (174). Since Ω_0 is independent from the configuration $\{\mathbf{r}^N, \mathbf{p}^N\}$ it follows then from equation (175) that

$$\Omega[f] = \Omega_0 + \beta^{-1} \text{Tr} f (\ln f - \ln f_0). \quad (177)$$

Employing the Gibbs-Bogoliubov relation (173) for $x = f/f_0$ we obtain

$$\text{Tr} f (\ln f - \ln f_0) \geq \text{Tr} (f - f_0). \quad (178)$$

The right hand side of the inequality (178) vanishes since f and f_0 are normalized probability distributions, and the left hand side vanishes only for $f = f_0$. Hence, by

combining (177) with (178) we have shown that

$$\Omega[f] > \Omega[f_0] = \Omega_0, \text{ for } f \neq f_0. \quad (179)$$

II. Inhomogeneous profiles of the interface

In section 4.2.4 we calculated the interfacial structure for a binary mixture. Here we show how integrations of type (139) can be carried out, that is,

$$I(\mathbf{r}) \equiv \int d\mathbf{r}' \rho(\mathbf{r}') L(\mathbf{r}') J(|\mathbf{r} - \mathbf{r}'|), \quad (180)$$

where $J(|\mathbf{r} - \mathbf{r}'|)$ is the range-dependent coupling term and $L(\mathbf{r}')$ is the local magnetization (see section 4.2.1).

In the two-dimensional case where the interface is aligned along the x -direction we have $\rho(\mathbf{r}) = \rho(z)$. We may then rewrite the convolution term in equation (180), that is,

$$I(z) = \int d\mathbf{r}' \rho(z') L(z') J(|\mathbf{r} - \mathbf{r}'|). \quad (181)$$

Rewriting the integral gives

$$I(z) = \int_{-\infty}^{+\infty} dz' \rho(z') L(z') \int_{-\infty}^{+\infty} dx' J(\sqrt{(x - x')^2 + (z - z')^2}). \quad (182)$$

By shifting the variable $x' - x \rightarrow x$ and introducing $a = z - z'$, we can show that the internal integral is proportional to a modified Bessel function of the second kind, that is,

$$\tilde{K}_0(a) = \int_{-\infty}^{+\infty} dx J(\sqrt{x^2 + a^2}). \quad (183)$$

Substituting $x = a \sinh u$ in equation (183) yields

$$\tilde{K}_0(a) = \int_{-\infty}^{+\infty} du a \cosh u J(a \cosh u). \quad (184)$$

By inserting the definition of the coupling term we finally find that

$$\tilde{K}_0(a) = J \int_{-\infty}^{+\infty} du \exp(-a \cosh u). \quad (185)$$

The last equation can be used for the numerical evaluation of equations (140)-(141).

Bibliography

- [1] A. Einstein, “Über die von der molekularkinetischen Theorie der Wärme geforderte Bewegung von in ruhenden Flüssigkeiten suspendierten Teilchen,” *Annalen der Physik*, vol. 322, no. 8, pp. 549–560, 1905.
- [2] M. von Smoluchowski, “Zur kinetischen Theorie der Brownschen Molekularbewegung und der Suspensionen,” *Annalen der Physik*, vol. 326, no. 14, pp. 756–780, 1906.
- [3] J. Perrin, *Brownian movement and molecular reality / by M. Jean Perrin ; translated from the Annales de chimie et de physique, 8me series, September 1909 by F. Soddy*. London Taylor and Francis, 1910.
- [4] J. Dhont, *An Introduction to Dynamics of Colloids*. Studies in Interface Science, Elsevier Science, 1996.
- [5] G. Bogush, M. Tracy, and C. Z. IV, “Preparation of monodisperse silica particles: Control of size and mass fraction,” *Journal of Non-Crystalline Solids*, vol. 104, no. 1, pp. 95 – 106, 1988.
- [6] L. Antl, J. Goodwin, R. Hill, R. Ottewill, S. Owens, S. Papworth, and J. Waters, “The preparation of poly(methyl methacrylate) latices in non-aqueous media,” *Colloids and Surfaces*, vol. 17, no. 1, pp. 67 – 78, 1986.
- [7] A. D. Nikolov and D. T. Wasan, “Dispersion stability due to structural contributions to the particle interaction as probed by thin liquid film dynamics,” *Langmuir*, vol. 8, no. 12, pp. 2985–2994, 1992.
- [8] Widawski Gilles, Rawiso Michel, and Francois Bernard, “Self-organized honeycomb morphology of star-polymer polystyrene films,” *Nature*, vol. 369, pp. 387–389, jun 1994. 10.1038/369387a0.
- [9] S. M. Grayson and J. M. Frechet, “Convergent dendrons and dendrimers: from synthesis to applications,” *Chemical reviews*, vol. 101, no. 12, pp. 3819–3868, 2001.
- [10] K. R. Purdy, S. Varga, A. Galindo, G. Jackson, and S. Fraden, “Nematic phase

- transitions in mixtures of thin and thick colloidal rods,” *Phys. Rev. Lett.*, vol. 94, p. 057801, Feb 2005.
- [11] P. M. Johnson, C. M. van Kats, and A. van Blaaderen, “Synthesis of colloidal silica dumbbells,” *Langmuir*, vol. 21, no. 24, pp. 11510–11517, 2005.
- [12] P. Linse and V. Lobaskin, “Electrostatic attraction and phase separation in solutions of like-charged colloidal particles,” *Phys. Rev. Lett.*, vol. 83, pp. 4208–4211, Nov 1999.
- [13] S. H. L. Klapp, “Dipolar fluids under external perturbations,” *Journal of Physics: Condensed Matter*, vol. 17, no. 15, p. R525, 2005.
- [14] E. Bianchi, R. Blaak, and C. N. Likos, “Patchy colloids: state of the art and perspectives,” *Phys. Chem. Chem. Phys.*, vol. 13, pp. 6397–6410, 2011.
- [15] G.-R. Yi, D. J. Pine, and S. Sacanna, “Recent progress on patchy colloids and their self-assembly,” *Journal of Physics: Condensed Matter*, vol. 25, no. 19, p. 193101, 2013.
- [16] P. N. Pusey and W. van Megen, “Phase behaviour of concentrated suspensions of nearly hard colloidal spheres,” *Nature*, vol. 320, pp. 340–342, Mar. 1986.
- [17] P. Pusey, W. V. Megen, S. Underwood, P. Bartlett, and R. Ottewill, “Colloidal fluids, crystals and glasses,” *Physica A: Statistical Mechanics and its Applications*, vol. 176, no. 1, pp. 16 – 27, 1991.
- [18] W. C. K. Poon, “The physics of a model colloid-polymer mixture,” *Journal of Physics: Condensed Matter*, vol. 14, no. 33, p. R859, 2002.
- [19] G. Foffi, E. Zaccarelli, P. Tartaglia, F. Sciortino, and K. Dawson, *Are particle gels glasses?*, vol. 118 of *Progress in Colloid and Polymer Science*. Springer Berlin Heidelberg, 2001.
- [20] K. Dawson, G. Foffi, M. Fuchs, W. Götze, F. Sciortino, M. Sperl, P. Tartaglia, T. Voigtmann, and E. Zaccarelli, “Higher-order glass-transition singularities in colloidal systems with attractive interactions,” *Phys. Rev. E*, vol. 63, p. 011401, Dec 2000.
- [21] R. Rungsawang, J. da Silva, C.-P. Wu, E. Sivaniah, A. Ionescu, C. H. W. Barnes, and N. J. Darton, “Magnetically induced pattern formation in phase separating polymer-solvent nanoparticle mixtures,” *Phys. Rev. Lett.*, vol. 104, p. 255703, Jun 2010.
- [22] G. M. Range and S. H. L. Klapp, “Pair formation and global ordering of strongly interacting ferrocolloid mixtures: An integral equation study,” *J. Chem. Phys.*,

- vol. 124, no. 11, p. 114707, 2006.
- [23] M. Dennison, M. Dijkstra, and R. van Roij, “Phase diagram and effective shape of semiflexible colloidal rods and biopolymers,” *Phys. Rev. Lett.*, vol. 106, p. 208302, May 2011.
- [24] E. Lomba, J. J. Weis, and C. F. Tejero, “Liquid-solid transition of the ferromagnetic heisenberg fluid: Simulation, density functional, and perturbation theories,” *Phys. Rev. E*, vol. 58, pp. 3426–3435, Sep 1998.
- [25] E. Lomba, J.-J. Weis, N. G. Almarza, F. Bresme, and G. Stell, “Phase transitions in a continuum model of the classical heisenberg magnet: The ferromagnetic system,” *Phys. Rev. E*, vol. 49, pp. 5169–5178, Jun 1994.
- [26] F. Lado, E. Lomba, and J. J. Weis, “Integral equation and simulation studies of the heisenberg spin fluid in an external magnetic field,” *Phys. Rev. E*, vol. 58, pp. 3478–3489, Sep 1998.
- [27] J. M. Tavares, M. M. Telo da Gama, P. I. C. Teixeira, J. J. Weis, and M. J. P. Nijmeijer, “Phase diagram and critical behavior of the ferromagnetic heisenberg fluid from density-functional theory,” *Phys. Rev. E*, vol. 52, pp. 1915–1929, Aug 1995.
- [28] A. Oukouiss and M. Baus, “Phase diagrams of the classical heisenberg fluid within the extended van der waals approximation,” *Phys. Rev. E*, vol. 55, pp. 7242–7252, Jun 1997.
- [29] I. P. Omelyan, R. Folk, A. Kovalenko, W. Fenz, and I. M. Mryglod, “Liquid-vapor interfaces in xy -spin fluids: An inhomogeneous anisotropic integral-equation approach,” *Phys. Rev. E*, vol. 79, p. 011123, Jan 2009.
- [30] I. P. Omelyan, W. Fenz, I. M. Mryglod, and R. Folk, “ xy spin fluid in an external magnetic field,” *Phys. Rev. Lett.*, vol. 94, p. 045701, Feb 2005.
- [31] P. H. V. Konynenburg and R. L. Scott, “Critical lines and phase equilibria in binary van der waals mixtures,” *Philosophical Transactions of the Royal Society of London. Series A, Mathematical and Physical Sciences*, vol. 298, no. 1442, pp. 495–540, 1980.
- [32] N. B. Wilding, F. Schmid, and P. Nielaba, “Liquid-vapor phase behavior of a symmetrical binary fluid mixture,” *Phys. Rev. E*, vol. 58, pp. 2201–2212, Aug 1998.
- [33] E. A. G. Jamie, R. P. A. Dullens, and D. G. A. L. Aarts, “Spinodal decomposition of a confined colloid-polymer system,” *The Journal of Chemical Physics*, vol. 137, no. 20, p. 204902, 2012.

- [34] A. J. Archer and R. Evans, “Binary gaussian core model: Fluid-fluid phase separation and interfacial properties,” *Phys. Rev. E*, vol. 64, p. 041501, Sep 2001.
- [35] J.-M. Bomont and D. Costa, “A theoretical study of structure and thermodynamics of fluids with long-range competing interactions exhibiting pattern formation,” *The Journal of Chemical Physics*, vol. 137, no. 16, p. 164901, 2012.
- [36] M. B. Sweatman, R. Fartaria, and L. Lue, “Cluster formation in fluids with competing short-range and long-range interactions,” *The Journal of Chemical Physics*, vol. 140, no. 12, p. 124508, 2014.
- [37] J. C. F. Toledano, F. Sciortino, and E. Zaccarelli, “Colloidal systems with competing interactions: from an arrested repulsive cluster phase to a gel,” *Soft Matter*, vol. 5, pp. 2390–2398, 2009.
- [38] P. Linse and V. Lobaskin, “Electrostatic attraction and phase separation in solutions of like-charged colloidal particles,” *The Journal of Chemical Physics*, vol. 112, no. 8, pp. 3917–3927, 2000.
- [39] B. Ruzicka, L. Zulian, E. Zaccarelli, R. Angelini, M. Sztucki, A. Moussaid, and G. Ruocco, “Competing interactions in arrested states of colloidal clays,” *Phys. Rev. Lett.*, vol. 104, p. 085701, Feb 2010.
- [40] A. Wysocki, C. R ath, A. V. Ivlev, K. R. S utterlin, H. M. Thomas, S. Khrapak, S. Zhdanov, V. E. Fortov, A. M. Lipaev, V. I. Molotkov, O. F. Petrov, H. L owen, and G. E. Morfill, “Kinetics of fluid demixing in complex plasmas: Role of two-scale interactions,” *Phys. Rev. Lett.*, vol. 105, p. 045001, Jul 2010.
- [41] M. H. K opf, S. V. Gurevich, R. Friedrich, and U. Thiele, “Substrate-mediated pattern formation in monolayer transfer: a reduced model,” *New Journal of Physics*, vol. 14, no. 2, p. 023016, 2012.
- [42] P. Tierno, P. Reimann, T. H. Johansen, and F. Sagu es, “Giant transversal particle diffusion in a longitudinal magnetic ratchet,” *Phys. Rev. Lett.*, vol. 105, p. 230602, Dec 2010.
- [43] P. Tierno, T. M. Fischer, T. H. Johansen, and F. Sagu es, “Colloidal assembly on magnetically vibrated stripes,” *Phys. Rev. Lett.*, vol. 100, p. 148304, Apr 2008.
- [44] P. Tierno, T. H. Johansen, and T. M. Fischer, “Localized and delocalized motion of colloidal particles on a magnetic bubble lattice,” *Phys. Rev. Lett.*, vol. 99, p. 038303, Jul 2007.
- [45] R. Evans, “The nature of the liquid-vapour interface and other topics in the statistical mechanics of non-uniform, classical fluids,” *Advances in Physics*,

- vol. 28(2), pp. 143–200, 1979.
- [46] W. Fenz, R. Folk, I. M. Mryglod, and I. P. Omelyan, “Phase diagrams of classical spin fluids: The influence of an external magnetic field on the liquid-gas transition,” *Phys. Rev. E*, vol. 68, p. 061510, Dec 2003.
- [47] D. G. Grier, “A revolution in optical manipulation,” *Nature*, vol. 424, pp. 810–816, aug 2003.
- [48] P. Hänggi and F. Marchesoni, “Artificial brownian motors: Controlling transport on the nanoscale,” *Rev. Mod. Phys.*, vol. 81, pp. 387–442, Mar 2009.
- [49] P. S. Burada, P. Hänggi, F. Marchesoni, G. Schmid, and P. Talkner, “Diffusion in confined geometries,” *ChemPhysChem*, vol. 10, no. 1, pp. 45–54, 2009.
- [50] P. Reimann, “Brownian motors: noisy transport far from equilibrium,” *Physics Rep.*, vol. 361, pp. 57–265, 2002.
- [51] A. Ros, R. Eichhorn, J. Regtmeier, T. T. Duong, P. Reimann, and D. Anselmetti, “Brownian motion: Absolute negative particle mobility,” *Nature*, vol. 436, pp. 928–928, Aug 2005.
- [52] S.-H. Lee and D. G. Grier, “Giant colloidal diffusivity on corrugated optical vortices,” *Phys. Rev. Lett.*, vol. 96, p. 190601, May 2006.
- [53] V. Blickle, T. Speck, U. Seifert, and C. Bechinger, “Characterizing potentials by a generalized boltzmann factor,” *Phys. Rev. E*, vol. 75, p. 060101, Jun 2007.
- [54] A. V. Arzola, K. Volke-Sepúlveda, and J. L. Mateos, “Experimental control of transport and current reversals in a deterministic optical rocking ratchet,” *Phys. Rev. Lett.*, vol. 106, p. 168104, Apr 2011.
- [55] W. Mu, Z. Liu, L. Luan, G. Wang, G. C. Spalding, and J. B. Ketterson, “Enhanced particle transport in an oscillating sinusoidal optical potential,” *New Journal of Physics*, vol. 11, no. 10, p. 103017, 2009.
- [56] R. Gommers, V. Lebedev, M. Brown, and F. Renzoni, “Gating ratchet for cold atoms,” *Phys. Rev. Lett.*, vol. 100, p. 040603, Jan 2008.
- [57] P. Reimann, C. Van den Broeck, H. Linke, P. Hänggi, J. M. Rubi, and A. Pérez-Madrid, “Giant acceleration of free diffusion by use of tilted periodic potentials,” *Phys. Rev. Lett.*, vol. 87, p. 010602, Jun 2001.
- [58] K. Lindenberg, J. M. Sancho, A. M. Lacasta, and I. M. Sokolov, “Dispersionless transport in a washboard potential,” *Phys. Rev. Lett.*, vol. 98, p. 020602, Jan 2007.

- [59] F. Höfling and T. Franosch, “Anomalous transport in the crowded world of biological cells,” *Reports on Progress in Physics*, vol. 76, no. 4, p. 046602, 2013.
- [60] J. Jordanovic, S. Jäger, and S. H. L. Klapp, “Crossover from normal to anomalous diffusion in systems of field-aligned dipolar particles,” *Phys. Rev. Lett.*, vol. 106, p. 038301, Jan 2011.
- [61] A. Zaccone, H. Wu, and E. Del Gado, “Elasticity of arrested short-ranged attractive colloids: Homogeneous and heterogeneous glasses,” *Phys. Rev. Lett.*, vol. 103, p. 208301, Nov 2009.
- [62] P. Chaudhuri, L. Berthier, and W. Kob, “Universal nature of particle displacements close to glass and jamming transitions,” *Phys. Rev. Lett.*, vol. 99, p. 060604, Aug 2007.
- [63] R. Eichhorn, J. Regtmeier, D. Anselmetti, and P. Reimann, “Negative mobility and sorting of colloidal particles,” *Soft Matter*, vol. 6, pp. 1858–1862, 2010.
- [64] M. Evstigneev, O. Zvyagolskaya, S. Bleil, R. Eichhorn, C. Bechinger, and P. Reimann, “Diffusion of colloidal particles in a tilted periodic potential: Theory versus experiment,” *Phys. Rev. E*, vol. 77, p. 041107, Apr 2008.
- [65] Q.-H. Wei, C. Bechinger, and P. Leiderer, “Single-file diffusion of colloids in one-dimensional channels,” *Science*, vol. 287, no. 5453, pp. 625–627, 2000.
- [66] F. J. Cao, L. Dinis, and J. M. R. Parrondo, “Feedback control in a collective flashing ratchet,” *Phys. Rev. Lett.*, vol. 93, p. 040603, Jul 2004.
- [67] K. Pyragas, “Continuous control of chaos by self-controlling feedback,” *Physics Letters A*, vol. 170, no. 6, pp. 421 – 428, 1992.
- [68] E. Schöll and H. Schuster, *Handbook of Chaos Control*. John Wiley & Sons, 2007.
- [69] D. Wu and S. Zhu, “Brownian motor with time-delayed feedback,” *Phys. Rev. E*, vol. 73, p. 051107, May 2006.
- [70] M. Borromeo, S. Giusepponi, and F. Marchesoni, “Recycled noise rectification: An automated maxwells daemon,” *Phys. Rev. E*, vol. 74, p. 031121, Sep 2006.
- [71] E. M. Craig, B. R. Long, J. M. R. Parrondo, and H. Linke, “Effect of time delay on feedback control of a flashing ratchet,” *EPL (Europhysics Letters)*, vol. 81, no. 1, p. 10002, 2008.
- [72] D. Hennig, “Current control in a tilted washboard potential via time-delayed feedback,” *Phys. Rev. E*, vol. 79, p. 041114, Apr 2009.

- [73] D. Hennig, L. Schimansky-Geier, and P. Hänggi, “Directed transport of an inertial particle in a washboard potential induced by delayed feedback,” *Phys. Rev. E*, vol. 79, p. 041117, Apr 2009.
- [74] L. Lizana and T. Ambjörnsson, “Diffusion of finite-sized hard-core interacting particles in a one-dimensional box: Tagged particle dynamics,” *Phys. Rev. E*, vol. 80, p. 051103, Nov 2009.
- [75] A. Ethirajan, U. Wiedwald, H.-G. Boyen, B. Kern, L. Han, A. Klimmer, F. Weigl, G. Kästle, P. Ziemann, K. Fauth, J. Cai, R. Behm, A. Romanyuk, P. Oelhafen, P. Walther, J. Biskupek, and U. Kaiser, “A micellar approach to magnetic ultrahigh-density data-storage media: Extending the limits of current colloidal methods,” *Advanced Materials*, vol. 19, no. 3, pp. 406–410, 2007.
- [76] P. Tierno, F. Sagues, T. H. Johansen, and T. M. Fischer, “Colloidal transport on magnetic garnet films,” *Phys. Chem. Chem. Phys.*, vol. 11, pp. 9615–9625, 2009.
- [77] M. Wang, L. He, and Y. Yin, “Magnetic field guided colloidal assembly,” *Materials Today*, vol. 16, no. 4, pp. 110–116, 2013.
- [78] M. Tlidi, A. G. Vladimirov, D. Pieroux, and D. Turaev, “Spontaneous motion of cavity solitons induced by a delayed feedback,” *Phys. Rev. Lett.*, vol. 103, p. 103904, Sep 2009.
- [79] P. T. Korda, M. B. Taylor, and D. G. Grier, “Kinetically locked-in colloidal transport in an array of optical tweezers,” *Phys. Rev. Lett.*, vol. 89, p. 128301, Sep 2002.
- [80] K. Xiao and D. G. Grier, “Sorting colloidal particles into multiple channels with optical forces: Prismatic optical fractionation,” *Phys. Rev. E*, vol. 82, p. 051407, Nov 2010.
- [81] J. K. Percus, “Approximation methods in classical statistical mechanics,” *Phys. Rev. Lett.*, vol. 8, pp. 462–463, Jun 1962.
- [82] P. Hopkins, A. Fortini, A. J. Archer, and M. Schmidt, “The van hove distribution function for brownian hard spheres: Dynamical test particle theory and computer simulations for bulk dynamics,” *The Journal of Chemical Physics*, vol. 133, no. 22, p. 224505, 2010.
- [83] A. J. Archer, P. Hopkins, and M. Schmidt, “Dynamics in inhomogeneous liquids and glasses via the test particle limit,” *Phys. Rev. E*, vol. 75, p. 040501, Apr 2007.
- [84] B. B. Yellen, R. M. Erb, H. S. Son, R. Hewlin, Jr., H. Shang, and G. U. Lee,

- “Traveling wave magnetophoresis for high resolution chip based separations,” *Lab Chip*, vol. 7, pp. 1681–1688, 2007.
- [85] L. Gao, M. A. Tahir, L. N. Virgin, and B. B. Yellen, “Multiplexing superparamagnetic beads driven by multi-frequency ratchets,” *Lab Chip*, vol. 11, pp. 4214–4220, 2011.
- [86] Y. Ouyang, M. A. Tahir, D. J. Lichtenwalner, and B. B. Yellen, “Origin of multiplexing capabilities of multifrequency magnetic ratchets,” *Phys. Rev. E*, vol. 85, p. 041407, Apr 2012.
- [87] P. Tierno, “Depinning and collective dynamics of magnetically driven colloidal monolayers,” *Phys. Rev. Lett.*, vol. 109, p. 198304, Nov 2012.
- [88] P. Tierno, S. V. Reddy, M. G. Roper, T. H. Johansen, and T. M. Fischer, “Transport and separation of biomolecular cargo on paramagnetic colloidal particles in a magnetic ratchet,” *The Journal of Physical Chemistry B*, vol. 112, no. 12, pp. 3833–3837, 2008. PMID: 18318526.
- [89] B. B. Yellen, O. Hovorka, and G. Friedman, “Arranging matter by magnetic nanoparticle assemblers,” *Proceedings of the National Academy of Sciences of the United States of America*, vol. 102, no. 25, pp. 8860–8864, 2005.
- [90] N. D. Mermin, “Thermal properties of the inhomogeneous electron gas,” *Phys. Rev.*, vol. 137, pp. A1441–A1443, Mar 1965.
- [91] P. Tierno, T. H. Johansen, and T. M. Fischer, “Fast and rewritable colloidal assembly via field synchronized particle swapping,” *Applied Physics Letters*, vol. 104, no. 17, p. 174102, 2014.
- [92] J.-P. Hansen and I. R. McDonald, *Theory of Simple Liquids, Third Edition*. Academic Press, 3 ed., April 2006.
- [93] A. A. Louis, P. G. Bolhuis, and J. P. Hansen, “Mean-field fluid behavior of the gaussian core model,” *Phys. Rev. E*, vol. 62, pp. 7961–7972, Dec 2000.
- [94] H. Risken, *The Fokker-Planck Equation: Methods of Solutions and Applications*. Springer Series in Synergetics, Springer, 2nd ed. 1989. 3rd printing ed., Sept. 1996.
- [95] A. J. Archer and R. Evans, “Dynamical density functional theory and its application to spinodal decomposition,” *The Journal of Chemical Physics*, vol. 121, no. 9, pp. 4246–4254, 2004.
- [96] J. M. Brader and M. Schmidt, “Dynamic correlations in brownian many-body systems,” *The Journal of Chemical Physics*, vol. 140, no. 3, pp. –, 2014.

- [97] U. M. B. Marconi and P. Tarazona, “Dynamic density functional theory of fluids,” *The Journal of Chemical Physics*, vol. 110, no. 16, pp. 8032–8044, 1999.
- [98] U. M. B. Marconi and P. Tarazona, “Dynamic density functional theory of fluids,” *Journal of Physics: Condensed Matter*, vol. 12, no. 8A, p. A413, 2000.
- [99] E. Ott, C. Grebogi, and J. A. Yorke, “Controlling chaos,” *Phys. Rev. Lett.*, vol. 64, pp. 1196–1199, Mar 1990.
- [100] E. Shahverdiev, S. Sivaprakasam, and K. Shore, “Lag synchronization in time-delayed systems,” *Physics Letters A*, vol. 292, no. 6, pp. 320–324, 2002.
- [101] T. Hikihara and T. Kawagoshi, “An experimental study on stabilization of unstable periodic motion in magneto-elastic chaos,” *Physics Letters A*, vol. 211, no. 1, pp. 29–36, 1996.
- [102] K. Pyragas and K. Tamaševičius, “Experimental control of chaos by delayed self-controlling feedback,” *Physics Letters A*, vol. 180, no. 1-2, pp. 99–102, 1993.
- [103] K. Hall, D. J. Christini, M. Tremblay, J. J. Collins, L. Glass, and J. Billette, “Dynamic control of cardiac alternans,” *Phys. Rev. Lett.*, vol. 78, pp. 4518–4521, Jun 1997.
- [104] T. Sagawa and M. Ueda, “Nonequilibrium thermodynamics of feedback control,” *Phys. Rev. E*, vol. 85, p. 021104, Feb 2012.
- [105] D. Abreu and U. Seifert, “Thermodynamics of genuine nonequilibrium states under feedback control,” *Phys. Rev. Lett.*, vol. 108, p. 030601, Jan 2012.
- [106] G. Costantini and F. Marchesoni, “Threshold diffusion in a tilted washboard potential,” *EPL (Europhysics Letters)*, vol. 48, no. 5, p. 491, 1999.
- [107] A. Pototsky, A. J. Archer, M. Bestehorn, D. Merkt, S. Savel’ev, and F. Marchesoni, “Collective shuttling of attracting particles in asymmetric narrow channels,” *Phys. Rev. E*, vol. 82, p. 030401, Sep 2010.
- [108] A. Pototsky, A. J. Archer, S. E. Savel’ev, U. Thiele, and F. Marchesoni, “Ratcheting of driven attracting colloidal particles: Temporal density oscillations and current multiplicity,” *Phys. Rev. E*, vol. 83, p. 061401, Jun 2011.
- [109] X. X. Sun, L. R. Nie, and P. Li, “Effect of time delay on current of symmetric brownian motor,” *EPL (Europhysics Letters)*, vol. 95, no. 5, p. 50003, 2011.
- [110] L.-C. Du and D.-C. Mei, “Time delay control of absolute negative mobility and multiple current reversals in an inertial brownian motor,” *Journal of Statistical Mechanics: Theory and Experiment*, vol. 2011, no. 11, p. P11016, 2011.

- [111] B. J. Lopez, N. J. Kuwada, E. M. Craig, B. R. Long, and H. Linke, “Realization of a feedback controlled flashing ratchet,” *Phys. Rev. Lett.*, vol. 101, p. 220601, Nov 2008.
- [112] A. Pototsky and N. Janson, “Synchronization of a large number of continuous one-dimensional stochastic elements with time-delayed mean-field coupling,” *Physica D*, vol. 238, p. 175, 2009.
- [113] A. Pototsky, “Emergence and multistability of time-periodic states in a population of noisy passive rotators with time-lag coupling,” *Phys. Rev. E*, vol. 85, p. 036219, 2012.
- [114] W. H. Press, S. A. Teukolsky, W. T. Vetterling, and B. P. Flannery, *Numerical Recipes 3rd Edition: The Art of Scientific Computing*. New York, NY, USA: Cambridge University Press, 3 ed., 2007.
- [115] H. Kramers, “Brownian motion in a field of force and the diffusion model of chemical reactions,” *Physica*, vol. 7, no. 4, pp. 284 – 304, 1940.
- [116] S. Grandner and S. H. L. Klapp, “Freezing of charged colloids in slit pores,” *The Journal of Chemical Physics*, vol. 129, no. 24, p. 244703, 2008.
- [117] C. N. Likos, “Effective interactions in soft condensed matter physics,” *Physics Reports*, vol. 348, no. 4-5, pp. 267 – 439, 2001.
- [118] M. Evstigneev, S. von Gehlen, and P. Reimann, “Interaction-controlled brownian motion in a tilted periodic potential,” *Phys. Rev. E*, vol. 79, p. 011116, Jan 2009.
- [119] S. V. Gurevich and R. Friedrich, “Instabilities of localized structures in dissipative systems with delayed feedback,” *Phys. Rev. Lett.*, vol. 110, p. 014101, Jan 2013.
- [120] A. Pototsky, A. J. Archer, S. E. Savel’ev, U. Thiele, and F. Marchesoni, “Ratcheting of driven attracting colloidal particles: Temporal density oscillations and current multiplicity,” *Phys. Rev. E*, vol. 83, p. 061401, Jun 2011.
- [121] O. Zvyagolskaya, A. J. Archer, and C. Bechinger, “Criticality and phase separation in a two-dimensional binary colloidal fluid induced by the solvent critical behavior,” *EPL (Europhysics Letters)*, vol. 96, no. 2, p. 28005, 2011.
- [122] T. Kruppa, T. Neuhaus, R. Messina, and H. Löwen, “Soft repulsive mixtures under gravity: Brazil-nut effect, depletion bubbles, boundary layering, nonequilibrium shaking,” *The Journal of Chemical Physics*, vol. 136, no. 13, p. 134106, 2012.
- [123] G. Kahl and H. Löwen, “Classical density functional theory: an ideal tool to

- study heterogeneous crystal nucleation,” *Journal of Physics: Condensed Matter*, vol. 21, no. 46, p. 464101, 2009.
- [124] M. Hermes, E. C. M. Vermolen, M. E. Leunissen, D. L. J. Vossen, P. D. J. van Oostrum, M. Dijkstra, and A. van Blaaderen, “Nucleation of colloidal crystals on configurable seed structures,” *Soft Matter*, vol. 7, pp. 4623–4628, 2011.
- [125] S. van Teeffelen, C. N. Likos, and H. Löwen, “Colloidal crystal growth at externally imposed nucleation clusters,” *Phys. Rev. Lett.*, vol. 100, p. 108302, Mar 2008.
- [126] A. Chauviere, H. Hatzikirou, I. G. Kevrekidis, J. S. Lowengrub, and V. Cristini, “Dynamic density functional theory of solid tumor growth: Preliminary models,” *AIP Advances*, vol. 2, no. 1, p. 011210, 2012.
- [127] G. Busch and H.-J. Güntherodt, “Ferromagnetic behavior of liquid alloys,” *Physics Letters A*, vol. 27, no. 2, p. 110, 1968.
- [128] T. Albrecht, C. Bühner, M. Fähnle, K. Maier, D. Platzek, and J. Reske, “First observation of ferromagnetism and ferromagnetic domains in a liquid metal,” *Applied Physics A*, vol. 65, no. 2, pp. 215–220, 1997.
- [129] F. H. Stillinger, “Phase transitions in the gaussian core system,” *The Journal of Chemical Physics*, vol. 65, no. 10, pp. 3968–3974, 1976.
- [130] A. A. Louis, P. G. Bolhuis, J. P. Hansen, and E. J. Meijer, “Can polymer coils be modeled as “soft colloids”?,” *Phys. Rev. Lett.*, vol. 85, pp. 2522–2525, Sep 2000.
- [131] C. Likos, M. Schmidt, H. Löwen, M. Ballauff, D. Potschke, and P. Lindner, “Soft interaction between dissolved flexible dendrimers: Theory and experiment,” *Macromolecules*, vol. 34, no. 9, pp. 2914–2920, 2001.
- [132] C. Likos, S. Rosenfeldt, N. Dingenouts, M. Ballauff, P. Lindner, N. Werner, and F. Vogtle, “Gaussian effective interaction between flexible dendrimers of fourth generation: A theoretical and experimental study,” *J. Chem. Phys.*, vol. 117, no. 4, pp. 1869–1877, 2002.
- [133] I. O. Götze, A. J. Archer, and C. N. Likos, “Structure, phase behavior, and inhomogeneous fluid properties of binary dendrimer mixtures,” *J. Chem. Phys.*, vol. 124, no. 8, p. 084901, 2006.
- [134] J.-L. Colot, X.-G. Wu, H. Xu, and M. Baus, “Density-functional, landau, and onsager theories of the isotropic-nematic transition of hard ellipsoids,” *Phys. Rev. A*, vol. 38, pp. 2022–2036, Aug 1988.

- [135] A. Archer and R. Evans, “Nucleation of liquid droplets in a fluid with competing interactions,” *Molecular Physics*, vol. 109, no. 23-24, pp. 2711–2722, 2011.
- [136] L. Yelash, P. Virnau, W. Paul, K. Binder, and M. Müller, “Spinodal decomposition of polymer solutions: A parallelized molecular dynamics simulation,” *Phys. Rev. E*, vol. 78, p. 031801, Sep 2008.
- [137] K. Lichtner, A. J. Archer, and S. H. L. Klapp, “Phase separation dynamics in a two-dimensional magnetic mixture,” *The Journal of Chemical Physics*, vol. 136, no. 2, p. 024502, 2012.
- [138] M. J. Robbins, A. J. Archer, U. Thiele, and E. Knobloch, “Modeling the structure of liquids and crystals using one- and two-component modified phase-field crystal models,” *Phys. Rev. E*, vol. 85, p. 061408, Jun 2012.
- [139] J. K. G. Dhont, “Spinodal decomposition of colloids in the initial and intermediate stages,” *The Journal of Chemical Physics*, vol. 105, no. 12, pp. 5112–5125, 1996.
- [140] A. Archer, C. Likos, and R. Evans, “Binary star-polymer solutions: bulk and interfacial properties,” *Journal of Physics: Condensed Matter*, vol. 14, no. 46, pp. 12031–12050, 2002.
- [141] R. Evans, J. Henderson, D. Hoyle, A. Parry, and Z. Sabeur, “Asymptotic decay of liquid structure: Oscillatory liquid-vapour density profiles and the fisher-widom line,” *Molec. Phys.*, vol. 80, pp. 755–775, 1993.
- [142] J. Brader, R. Evans, M. Schmidt, and H. Löwen, “Entropic wetting and the fluid-fluid interface of a model colloid-polymer mixture,” *J. Phys.: Condens. Matter*, vol. 14, p. L1, 2002.
- [143] A. Lang, C. N. Likos, M. Watzlawek, and H. Löwen, “Fluid and solid phases of the gaussian core model,” *Journal of Physics: Condensed Matter*, vol. 12, no. 24, p. 5087, 2000.
- [144] R. Lovett and M. Baus, “Fluid interfaces as treated by density functional theory,” *Physica A*, vol. 194, no. 1-4, pp. 93 – 104, 1993.
- [145] J. S. Rowlinson and B. Widom, *Molecular Theory of Capillarity*. Dover Publications, Jan. 2003.
- [146] M. Rex, H. H. Wensink, and H. Löwen, “Dynamical density functional theory for anisotropic colloidal particles,” *Phys. Rev. E*, vol. 76, p. 021403, Aug 2007.
- [147] J. W. Cahn and J. E. Hilliard, “Free energy of a nonuniform system. iii. nucleation in a two-component incompressible fluid,” *The Journal of Chemical Physics*,

- vol. 31, no. 3, pp. 688–699, 1959.
- [148] M. Schmidt, H. Löwen, J. M. Brader, and R. Evans, “Density functional for a model colloid-polymer mixture,” *Phys. Rev. Lett.*, vol. 85, pp. 1934–1937, Aug 2000.
- [149] G. M. Range and S. H. L. Klapp, “Demixing in simple dipolar mixtures: Integral equation versus density functional results,” *Phys. Rev. E*, vol. 70, p. 031201, Sep 2004.
- [150] R. Desai and R. Kapral, *Dynamics of self-organized and self-assembled structures*. Cambridge University Press, 2009.
- [151] J. Stenhammar, A. Tiribocchi, R. J. Allen, D. Marenduzzo, and M. E. Cates, “Continuum theory of phase separation kinetics for active brownian particles,” *Phys. Rev. Lett.*, vol. 111, p. 145702, Oct 2013.
- [152] D. G. A. L. Aarts, R. P. A. Dullens, and H. N. W. Lekkerkerker, “Interfacial dynamics in demixing systems with ultralow interfacial tension,” *New Journal of Physics*, vol. 7, no. 1, p. 40, 2005.
- [153] J. W. Cahn and J. E. Hilliard, “Free energy of a nonuniform system. i. interfacial free energy,” *The Journal of Chemical Physics*, vol. 28, no. 2, pp. 258–267, 1958.
- [154] J. W. Cahn, “On spinodal decomposition,” *Acta Metallurgica*, vol. 9, no. 9, pp. 795 – 801, 1961.
- [155] J. F. M. Lodge and D. M. Heyes, “Brownian dynamics simulations of lennard-jones gas/liquid phase separation and its relevance to gel formation,” *J. Chem. Soc., Faraday Trans.*, vol. 93, pp. 437–448, 1997.
- [156] J. F. M. Lodge and D. M. Heyes, “Structural evolution of phase-separating model colloidal liquids by brownian dynamics computer simulation,” *The Journal of Chemical Physics*, vol. 109, no. 17, pp. 7567–7577, 1998.
- [157] D. W. Oxtoby and R. Evans, “Nonclassical nucleation theory for the gas–liquid transition,” *The Journal of Chemical Physics*, vol. 89, no. 12, pp. 7521–7530, 1988.
- [158] V. Talanquer and D. W. Oxtoby, “Dynamical density functional theory of gas–liquid nucleation,” *The Journal of Chemical Physics*, vol. 100, no. 7, pp. 5190–5200, 1994.
- [159] M. J. Uline and D. S. Corti, “Activated instability of homogeneous bubble nucleation and growth,” *Phys. Rev. Lett.*, vol. 99, p. 076102, Aug 2007.
- [160] Lutsko, J. F., “Theoretical description of the nucleation of vapor bubbles in a

- superheated fluid,” *EPL*, vol. 83, no. 4, p. 46007, 2008.
- [161] J. F. Lutsko, “Density functional theory of inhomogeneous liquids. III. Liquid-vapor nucleation,” *The Journal of Chemical Physics*, vol. 129, no. 24, p. 244501, 2008.
- [162] J. F. Lutsko, “Communication: A dynamical theory of homogeneous nucleation for colloids and macromolecules,” *The Journal of Chemical Physics*, vol. 135, no. 16, p. 161101, 2011.
- [163] S. Aliaskarisohi, T. H. Johansen, and T. M. Fischer, “Using symmetry breaking for directed transport of paramagnetic colloids on garnet films,” *The Journal of Physical Chemistry B*, vol. 115, no. 10, pp. 2243–2247, 2011.
- [164] R. Bartussek, P. Hänggi, and J. G. Kissner, “Periodically rocked thermal ratchets,” *EPL (Europhysics Letters)*, vol. 28, no. 7, p. 459, 1994.
- [165] A. V. Straube and P. Tierno, “Tunable interactions between paramagnetic colloidal particles driven in a modulated ratchet potential,” *Soft Matter*, vol. 10, pp. 3915–3925, 2014.
- [166] J. Dzubiella and H. Löwen, “Pattern formation in driven colloidal mixtures: tilted driving forces and re-entrant crystal freezing,” *Journal of Physics: Condensed Matter*, vol. 14, no. 40, p. 9383, 2002.
- [167] M. Wilczek and S. Gurevich, “Locking of periodic patterns in cahn-hilliard models for langmuir-blodgett transfer,” *arXiv:1308.6691v2*, 2014.
- [168] A. Krekhov, “Formation of regular structures in the process of phase separation,” *Phys. Rev. E*, vol. 79, p. 035302, Mar 2009.
- [169] M. Rex and H. Löwen, “Dynamical density functional theory with hydrodynamic interactions and colloids in unstable traps,” *Phys. Rev. Lett.*, vol. 101, p. 148302, Sep 2008.
- [170] C. P. Royall, J. Dzubiella, M. Schmidt, and A. van Blaaderen, “Nonequilibrium sedimentation of colloids on the particle scale,” *Phys. Rev. Lett.*, vol. 98, p. 188304, May 2007.
- [171] R. L. C. Vink and A. J. Archer, “Phase separation in fluids exposed to spatially periodic external fields,” *Phys. Rev. E*, vol. 85, p. 031505, Mar 2012.
- [172] D. A. Strehober, H. Engel, and S. H. L. Klapp, “Oscillatory motion of sheared nanorods beyond the nematic phase,” *Phys. Rev. E*, vol. 88, p. 012505, Jul 2013.
- [173] P. Stansell, K. Stratford, J.-C. Desplat, R. Adhikari, and M. E. Cates, “Nonequilibrium steady states in sheared binary fluids,” *Phys. Rev. Lett.*, vol. 96, p. 085701,

Mar 2006.

- [174] J. Yan, M. Bloom, S. C. Bae, E. Luijten, and S. Granick, “Linking synchronization to self-assembly using magnetic janus colloids,” *Nature*, vol. 491, pp. 578–581, Nov. 2012.
- [175] S. H. L. Klapp, “Materials science: Synchronized tumbling particles,” *Nature*, vol. 491, pp. 530–531, Nov. 2012.
- [176] B. D. Marshall and W. G. Chapman, “A density functional theory for patchy colloids based on wertheim’s association theory: Beyond the single bonding condition,” *The Journal of Chemical Physics*, vol. 138, no. 4, pp. –, 2013.
- [177] P. Hartmann, M. Rosenberg, G. J. Kalman, and Z. Donkó, “Ground-state structures of superparamagnetic two-dimensional dusty plasma crystals,” *Phys. Rev. E*, vol. 84, p. 016409, Jul 2011.
- [178] S. Nunomura, N. Ohno, and S. Takamura, “Confinement and structure of electrostatically coupled dust clouds in a direct current plasma–sheath,” *Physics of Plasmas*, vol. 5, no. 10, pp. 3517–3523, 1998.
- [179] K. Zahn, R. Lenke, and G. Maret, “Two-stage melting of paramagnetic colloidal crystals in two dimensions,” *Phys. Rev. Lett.*, vol. 82, pp. 2721–2724, Mar 1999.
- [180] M. Oettel and S. Dietrich, “Colloidal interactions at fluid interfaces,” *Langmuir*, vol. 24, no. 4, pp. 1425–1441, 2008.

Acknowledgements

In the first place, I want to thank my supervisor Sabine Klapp for giving me the opportunity to work in her group on the challenging field of complex fluids. With her constant support and great advice she brought me closer to physics than I could have done by myself.

I am very grateful for being able to work together with my collaborators, Andy and Andrey. Andy, thank you for letting me come to Loughborough and teaching me a lot about soft matter in this short time. Another word of thanks is addressed to Joe Dzubielia who agreed to read and grade my thesis.

My thanks also goes to the entire work group in the second floor, in particular, Sebastian, Gerald and Rodrigo with whom I shared enjoyable and memorable discussions. Rodrigo, thanks for discussing and reading parts of my thesis.

I also would like to thank all my friends without whom the realization of this thesis would not have been possible. I cordially greet family Werlen for all the support and love from the distance.

Finally, I want to thank all my colleagues at the ITP, in particular, Carsten, Helge and Arash who enriched my experiences not only as a teaching assistant over the recent years.

This work is dedicated to my family who always supported me and my curiosity inside and outside of science.

